Title
Gas Adsorption in Flexible Metal–Organic Frameworks

Author
Taylor, Mercedes

Publication Date
2018

Peer reviewed|Thesis/dissertation

Gas Adsorption in Flexible Metal–Organic Frameworks

by

Mercedes Kelleher Taylor

A dissertation submitted in partial satisfaction of the

requirements for the degree of

Doctor of Philosophy

in

Chemistry

in the

Graduate Division

of the

University of California, Berkeley

Committee in charge:

Professor Jeffrey R. Long, Chair
Professor Omar M. Yaghi
Professor Bryan D. McCloskey

Fall 2018

Abstract

Gas adsorption in Flexible Metal–Organic Frameworks

by

Mercedes Kelleher Taylor

Doctor of Philosophy in Chemistry

University of California, Berkeley

Professor Jeffrey R. Long, Chair

The work presented herein describes the synthesis and investigation of structurally flexible metal–organic frameworks for gas adsorption applications. These highly crystalline, porous solids are promising materials for the storage and separation of gases such as CH_4, CO_2, and H_2. Furthermore, metal–organic frameworks are amenable to straightforward synthetic modification, due to their modular nature, and thus provide fertile ground for structure-property relationship studies.

Chapter 1 begins with a description of gas adsorption in porous materials, including activated carbons and zeolites. Metal–organic frameworks are introduced as an emerging alternative class of adsorbents, and their synthesis and hallmark structural features are discussed. Chapter 1 then provides an overview of flexible metal–organic frameworks in the literature and discusses their structural features and mechanisms of flexibility. Finally, the flexible metal–organic framework Co(bdp) is described, along with its record-setting CH_4 storage properties, to set the stage for the research presented herein.

Chapter 2 reports the synthesis of a library of Co(bdp) derivatives with varying functionalizations of the bdp^{2-} ligand, resulting in synthetic control over CH_4 pressure at which Co(bdp) undergoes a phase change. Notably, fluorination of bdp^{2-} disrupts π– π interactions that stabilize the collapsed phase of Co(bdp), while methylation of bdp^{2-} strengthens these interactions, thus lowering or raising the phase change pressure, respectively. The structure-property relationship between ligand functionalization and CH_4-induced phase change pressure is supported by *in situ* powder X-ray diffraction experiments.

Chapter 3 reports the effect of the identity of the adsorbate molecule on this phase change pressure (using CO_2, CH_4, N_2, and H_2) and the highly effective separation of CO_2 and CH_4 in Co(bdp). The mechanism of this selectivity is investigated with *in situ* powder X-ray diffraction studies, which reveal that Co(bdp) expands to CO_2-templated phases even in the presence of CO_2/CH_4 mixtures. Multicomponent equilbrium adsorptions measurements, supplemented by dynamic breakthrough experiments, probe the limits of the remarkable CO_2/CH_4 selectivity shown by Co(bdp).

Chapter 4 describes the discovery of novel synthetic routes to the organic molecule 4,4'-bipyrazole, via the previously unknown homocoupling of pyrazoleboronic esters. This molecule is then used to synthesize the metal–organic framework Co(bpz),

which is shown to be structurally flexible. CO_2 adsorption and N_2 adsorption are shown to induced structural phase changes in this framework, in contrast to H_2 adsorption, which does not trigger a phase change, and this adsorbate-dependent phase change behavior can potentially be leveraged to accomplish gas separations in Co(bpz).

Table of Contents

Table of Schemes, Tables, and Figures

Chapter 1: Introduction

Chapter 2: Tuning the Adsorption-Induced Phase Change in the Flexible Metal–Organic Framework Co(bdp)

Chapter 3: Near-Perfect CO_2/CH_4 Selectivity Achieved through Reversible Guest Templating in the Flexible Metal–Organic Framework Co(bdp)

Chapter 4: Novel routes to 4,4'-bipyrazole (H_2bpz) and Co(bpz)

Acknowledgements

I am indebted to all the members of the Long group with whom I overlapped—undergraduates, grad students, postdocs, and visiting scholars—for teaching me a great deal of chemistry and helping me with so many experiments. Rather than list all of these teachers and collaborators, who number nearly a hundred, I thank them en masse for making the group such a supportive intellectual environment and for teaching me so much. Those whose work is directly incorporated into this thesis are named in the Acknowledgements sections of the individual chapters, but I will thank them again here: I am grateful to Tomče Runčevski, Julia Oktawiec, Miguel I. Gonzalez, Rebecca L. Siegelman, Jarad A. Mason, Jinxing Ye, Craig M. Brown, Jeffrey R. Long, Jonathan E. Bachman, Henry Jiang, Jacob D. Tarver, and Jiwoong Lee, for their great experimental and intellectual contributions to the work presented herein. In particular, I'm grateful to my advisor Jeff Long for providing me with interesting projects and good ideas as well as the freedom to direct my own research. Finally, my family has been supportive and encouraging throughout the whole process, for which I'm extremely thankful, especially to my cousin Kevin Frick and to my parents, Elizabeth Kelleher and Ross Taylor.

Chapter 1. Introduction

1.1. Fundamentals of Gas Adsorption

Adsorption is a phenomenon in which a molecular species weakly interacts with a surface. This interaction is energetically favorable and is a result of Van der Waals-type attraction between the molecule and the surface, and it serves to generate a weak and often reversible bond between the two species (Figure 1.1a). This concept is similar to that of *absorption* but is differentiated by the fact that adsorption is a surface-level interaction, whereas the absorption of a molecule into a solid entails the integration of the molecule into the interior of the material itself (Figure 1.1b).[1] The phenomenon of adsorption has been observed between many kinds of adsorbate molecules and adsorbent materials and has been incorporated into many important processes, including the adsorption of aqueous ions onto resins in water purification,[2] the adsorption of liquid hydrocarbons onto zeolites in petroleum refining,[3] and the adsorption of gas molecules onto activated carbons in alternative fuel storage.[4]

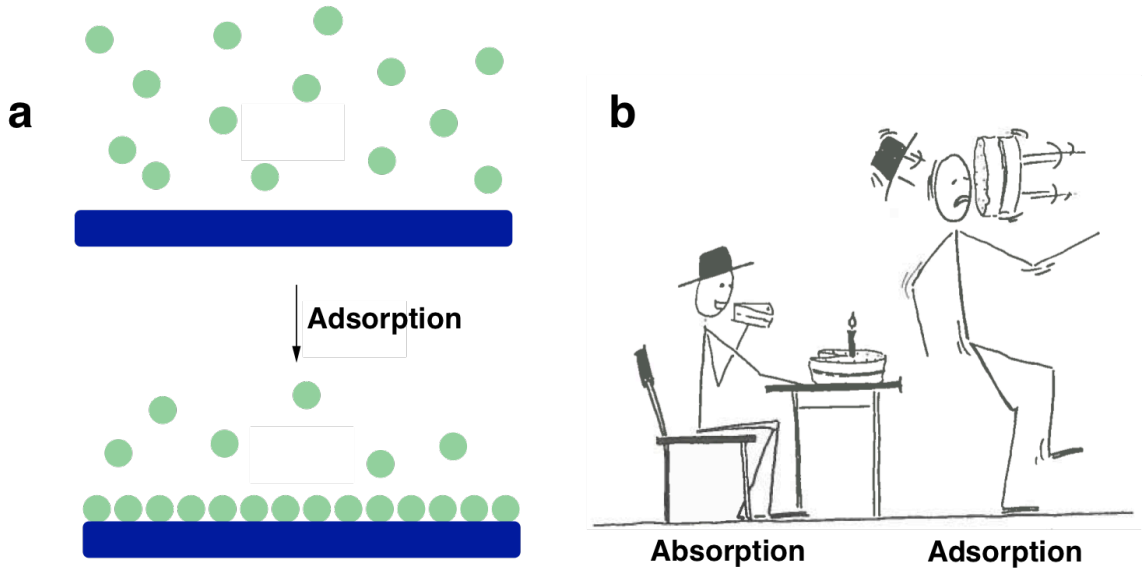

Figure 1.1. a) Schematic of molecules adsorbing onto a surface. b) A cartoon depicting the difference between absorption (eating cake) and adsorption (being splattered by cake). Adapted from Ref. 1.

The performance of a material as an adsorbent is usually characterized by a series of experiments that measure adsorption at various concentrations of the adsorbate. Typically, the mass of adsorbent is held constant while the amount of adsorbate is systematically increased, and the moles of adsorbate adsorbed per gram adsorbent is recorded after each increase. The resulting data is plotted as an adsorption isotherm (Figure 1.2), so called because the experiment is performed at a constant temperature.

Adsorptive interactions can be categorized based on the strength of the bond formed between the adsorbate and adsorbent. This bond strength is commonly referred to as the "binding enthalpy" or "heat of adsorption," terms which describe the heat released

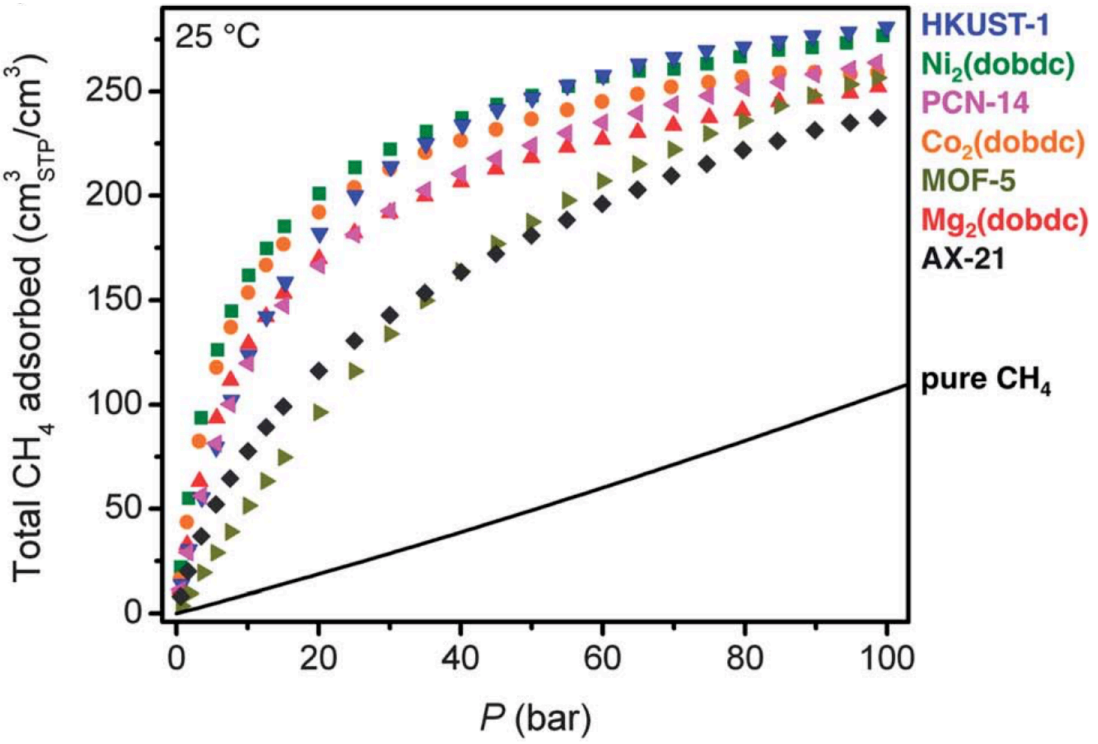

Figure 1.2. CH_4 adsorption isotherms at 25 °C for a variety of porous materials, compared to compression of pure (bulk) CH_4. Adapted from Ref. 36.

by the adsorption of one adsorbate molecule to the surface.[1] In many cases, the adsorbent surface is varied and contains sites of greater binding enthalpy and sites of weaker binding enthalpy. In such cases, adsorbate molecules will first populate the strongest binding sites and then later occupy the weaker sites, after all the strong binding sites are filled.[5] To describe the energy of adsorption in such cases, the term isosteric heat of adsorption (Q_{st}) is used to describe the average binding enthalpy at a given adsorbate loading (that is, after a certain number of adsorbate molecules are already adsorbed onto the adsorbent).[6] The isosteric heat of adsorption for a certain adsorbate/adsorbent pair is often represented as a plot showing the variation in binding enthalpy over adsorbate loading, and an example is given in Figure 1.3.

Adsorptive phenomena are grouped into the categories of physisorption or chemisorption, depending on the strength of the adsorbate-adsorbent interaction. Physisorption is generally considered to encompass interactions with binding enthalpies from approximately –4 kJ/mol to –50 kJ/mol, although this distinction is not rigid, and chemisorption describes all stronger adsorptive interactions. Chemisorption results from chemical reactivity between the adsorbate and the adsorbent and is often irreversible, as opposed to physisorption.[1]

The factors that govern the heat of adsorption of a given species onto a material include the chemical functionality, morphology, rigidity, porosity, and overall structure of the adsorbent material. These characteristics can be controlled by the rational design and synthesis of the material, and this synthetic control over the adsorption performance of a material comprises the major theme of this dissertation. However, the properties of

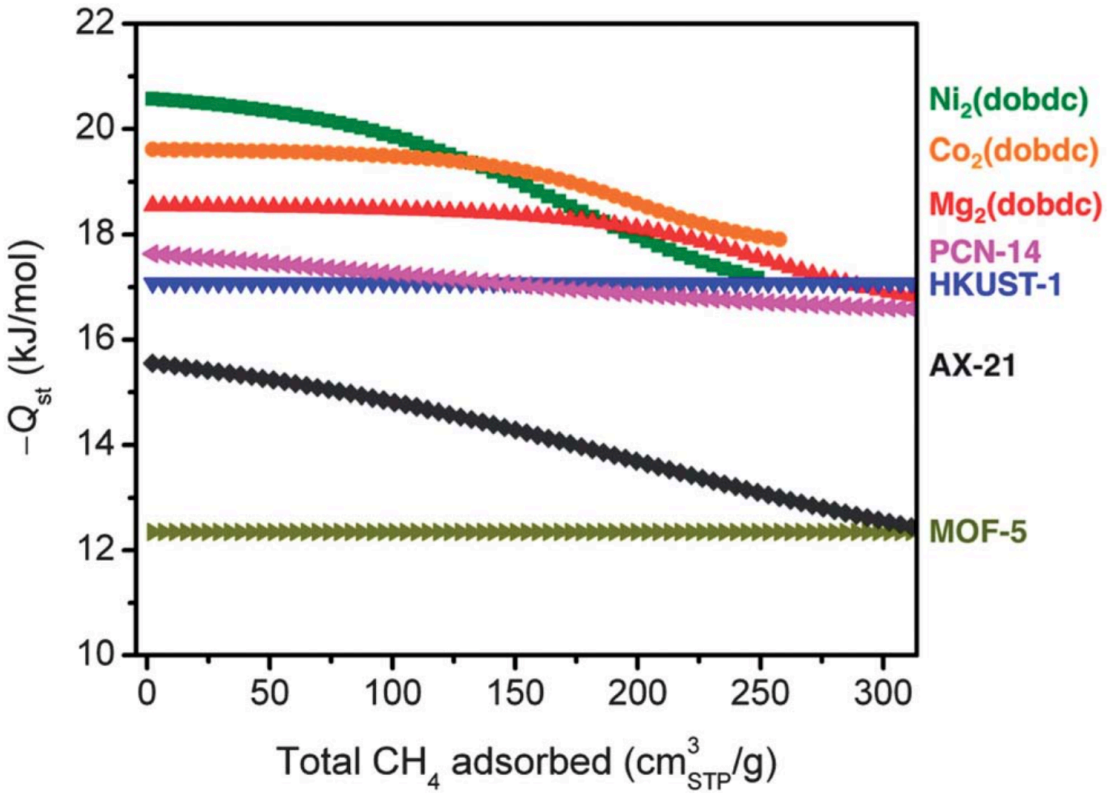

Figure 1.3. Isosteric heats of CH_4 adsorption ($-Q_{st}$) for a variety of porous materials. Adapted from Ref. 36.

the adsorbate molecule also significantly affect the adsorption behavior. For example, in spite of their similar size and physical properties, the gas molecules CO_2 and CH_4 display markedly different adsorption profiles with regards to the same adsorbent, as discussed further in Chapter 3. These differences in adsorption behavior are a result of subtle differences in polarity and chemical reactivity between the two molecules. Typically, the greater the polarity and polarizability of a molecule, the more strongly it will adsorb onto a surface, which is why H_2 is a particularly challenging adsorbate.[7] But beyond this rule of thumb, the adsorption behavior of a molecule depends on its unique electronic structure, arrangement of molecular orbitals, and mechanism of interaction with the adsorbent, so it is often necessary to consider these factors anew for each adsorbate when developing an adsorbent for a given application.

The adsorption of gases is a widely studied subset of the aforementioned adsorptive phenomena. The major techniques of gas adsorption characterization are gravimetric and volumetric adsorption measurements, in which a known volume of gas is dosed to an adsorbent sample, and the amount of adsorption is calculated by measuring either the change in mass or the change in volume of the sample holder, respectively.[1] These measurements are typically isothermal, but additional information can be gained by obtaining adsorption isotherms at a variety of temperatures, including a plot of the isosteric heat of adsorption for the adsorbate/adsorbent pair, as described in the Supporting Information of Chapter 3.

Because gas adsorption is a surface interaction, the gas adsorption capacity of a material will generally increase as the accessible surface area of the material increases. For this reason, highly porous materials are the most promising adsorbents for gas adsorption applications, as these materials provide the most available surface area for interaction with gas molecules. The porosity of an adsorbent is traditionally determined via N_2 adsorption at 77 K (the temperature at which N_2 condenses at atmospheric pressure). The data obtained from a 77-K N_2 adsorption isotherm can be fit to reveal the amount of surface area available to N_2 molecules, which is expressed in moles N_2 per gram of adsorbent. This value, known as a Brunauer-Emmett-Teller (BET) surface area, is a common metric used to compare the porosity of different materials.[1]

1.2. Industrial Applications of Gas Adsorption

Gas adsorption offers a promising solution to a number of problems associated with climate change, fuel storage, and industrial energy consumption. Specifically, by adsorbing a gas onto a solid adsorbent, the density of the gas can be greatly increased relative to its bulk density, thus allowing the gas to be stored under more moderate conditions than are typical of condensed gas cylinders or liquified, cryogenic storage systems.[8] Because many fuels and commodity chemicals are gaseous at standard conditions, the storage of gases is of major concern in many industries. By storing gases at ambient conditions, as is made possible by adsorption-based systems, the energetic cost of such systems can be kept to a minimum.

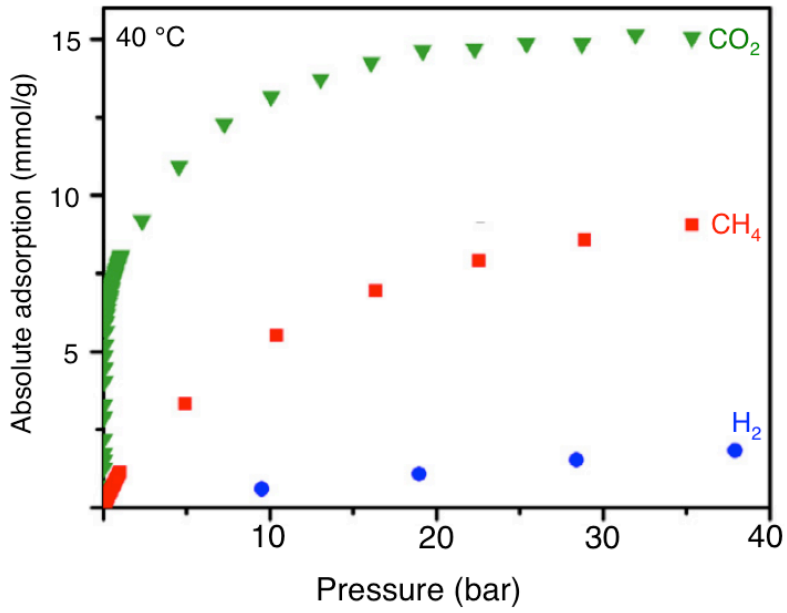

Figure 1.4. CO_2, CH_4, and H_2 isotherms at 40 °C for the metal–organic framework Mg_2(dobdc) (dobdc^{4-} = 1,4-dioxido-2,5-benzenedicarboxylate). Adapted from Ref. 7.

Similarly, adsorption-based processes can greatly reduce the energy necessary to separate gases from a mixture.[9] As described above, different gases adsorb to differing extents on a given adsorbent, based on the unique chemical and physical properties of each gas (Figure 1.4).[7] A adsorbent's varying affinity for various gases can be leveraged to achieve highly effective gas separations, which are often a great energy sink in industrial processes. Such separations are implicated in countless applications, from the separation of hydrocarbons and aromatic compounds to the removal of greenhouse gases from exhaust streams.[10] Consequently, research into adsorbents for gas separations is of increasing interest in the fields of chemistry and chemical engineering.

As mentioned above, materials with high permanent porosity are the most successful adsorbents for gas adsorption applications, because of the fact that this porosity allows adsorbate molecules to rapidly diffuse into the interior of the solid and because these interior pores and channels provide an enormous amount of additional surface area to which gas molecules can adsorb. Activated carbons are a class of porous materials that has received a great deal of research attention. These materials consist of an organic carbon base, usually derived from natural materials such as coconut husk, wood, or coal. This amorphous carbon-based solid is then activated by heating to extreme temperatures (often >600 °C) in the presence of oxidizing gases or strong acid or base. These harsh reaction conditions essentially burn holes throughout the material, generating a highly porous product. Over the decades during which the synthesis of activated carbons has been researched and industrialized, the activation process has been optimized to yield materials with surface areas above 4,000 m^2/g and high adsorption capacities for many different gases of interest.[11] Due to the low cost of the starting materials (coal, wood, etc.) and the highly optimized activation process, activated carbons have been widely adopted in industry and are used in many diverse chemical processes.[12]

However, these materials are amorphous, and the method of generating pores outlined above does not afford control over the pore shape and pore size beyond a certain narrow range. Consequently, synthetic control over the adsorption properties of activated carbons is quite limited. Based on the size and shape of these materials' characteristic slit-shaped pores, there are theoretical upper limits on the gas adsorption performance of activated carbons.[13] In order to exceed these limits, it is necessary to study materials whose properties are more tunable and are amenable to significant synthetic variation. Furthermore, the amorphous nature of activated carbons prevents crystallographic characterization of their pore structure, furthering inhibiting rational design and control of gas adsorption properties.

Zeolites represent another class of porous adsorbents that have received significant attention from academia and industry. Zeolites are materials composed of aluminum, silicon, and oxygen atoms arranged in repeating crystalline lattices, whose well-defined pores can be clearly characterized by X-ray crystallography (Figure 1.5).[14] The interconnected pores of zeolites allow these materials to act as "molecular sieves," by screening out larger molecules and adsorbing only those within a certain size range. The permanent porosity and molecular sieving abilities of zeolites make them well-suited to many industrial separations. However, like activated carbons, zeolites suffer from a lack of synthetic tunability.[15] Although the pore dimensions and overall structure of a zeolite can be tuned by changing the synthesis reaction conditions and using structure-directing agents, only a finite number of zeolite structures are known (despite extensive

research into the discovery of novel zeolite structures). This limitation on accessible zeolite structures may be due to the fact that only the most energetically stable structures nucleate in solution, preventing formation of less stable (but still structurally feasible) alternatives. Regardless of the theoretical explanation, only approximately 200 different zeolite structures have been characterized, out of the millions that have been proposed via computational modeling.[16]

In light of the great industrial need for porous adsorbents to store and separate gases, there is an urgent demand for fundamentally novel and tunable chemical structures that meet the criteria outlined above. Although many activated carbons and zeolites possess excellent gas adsorption properties for individual applications, these materials are not sufficiently tunable to allow chemists to adapt them for the numerous diverse processes that require better adsorbents. Consequently, chemists have turned to the emerging field of metal–organic frameworks to exercise greater creative control over synthetic porous adsorbents.

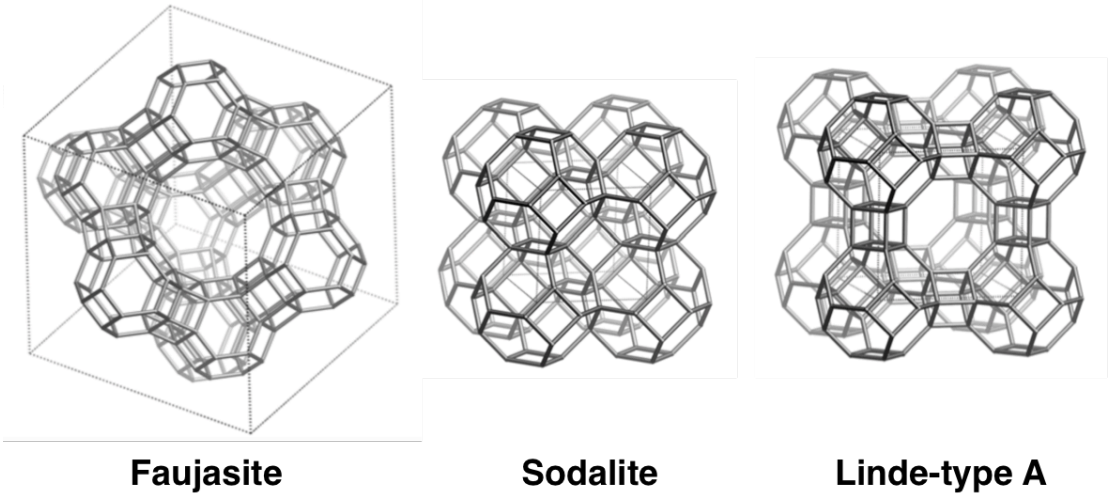

Figure 1.5. Three representative zeolite framework types. Adapted from Ref. 14.

1.3. An Emerging Class of Porous Materials: Metal–organic Frameworks

Metal–organic frameworks are a class of hybrid organic-inorganic materials in which multitopic organic ligands coordinate to multiple metal ions. The metal ions act as nodes which, when linked to each other by the organic ligands, form an extended three-dimensional structure composed of regularly repeating units (Figure 1.6). The first metal–organic framework was reported by Yaghi et al. in 1999,[17] although some similar materials (referred to as porous coordination polymers) had appeared in the literature throughout the preceding decade. After the report by Yaghi et al., the number of such reported structures exploded in the early 2000s, and the field of metal–organic frameworks quickly earned distinction as an emerging class of structually fascinating and potentially useful adsorbents.[18]

Traditional syntheses of metal–organic frameworks rely on the reaction of a metal salt with an organic ligand in a refluxing solvothermal synthesis, often in the presence of a base that slowly deprotonates the ligand over the course of the reaction. The high temperatures and long reaction times of most metal–organic framework syntheses allow the metal-ligand bonds to form, dissolve, and re-form until the system reaches an energetic minimum across the entire extended structure, resulting in a material of high symmetry, crystallinity, and regularity. Extended channels and pore systems bounded by rows of organic linkers or metal ions lead to exceptionally high surface areas in metal–organic frameworks, with the current record at 7000 m^2/g (BET).[19]

In the best cases, the crystalline and porous nature of metal–organic frameworks combines the respective advantages of zeolites and activated carbons in terms of gas adsorption applications. But arguably more promising than their observed structural properties is the high degree of tunability inherent to metal–organic frameworks. Because an exceedingly wide array of organic ligands and metal salts can be combined to yield an

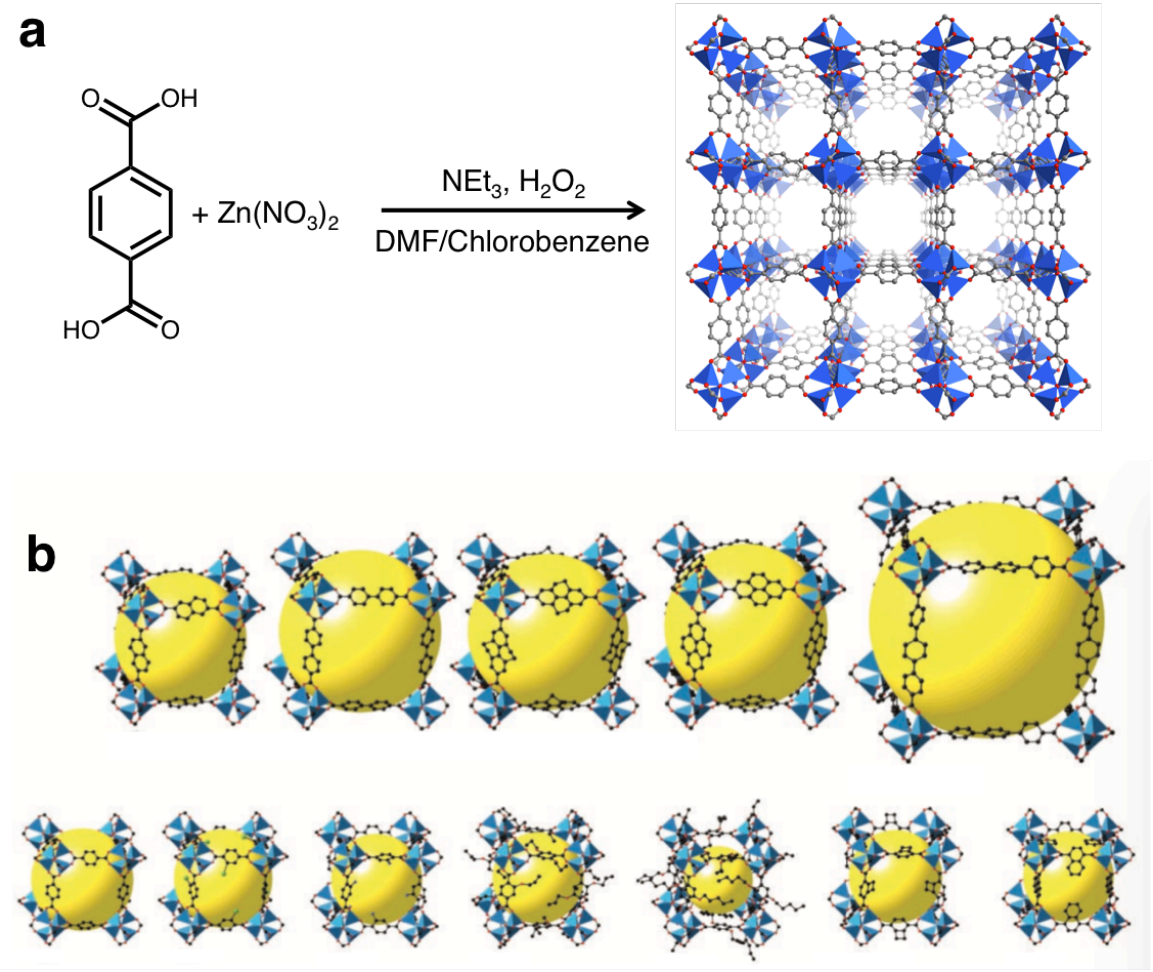

Figure 1.6. a) Conditions for the synthesis of the metal–organic framework MOF-5. b) An isoreticular series of MOF-5 analogues synthesized using different dicarboxylate linkers. Adapted from Refs. 17 and 20.

infinite set of theoretical products, the pore architectures and surface functionalities of metal–organic frameworks are within the control of synthetic chemists, and consequently the gas adsorption properties of these materials are within synthetic control as well.[20] As is demonstrated in Chapter 2, precise synthetic control over the adsorption performance of a metal–organic framework can be achieved via minor structural changes introduced in a targeted way.

Over the last 20 years, researchers have leveraged this synthetic control to yield metal–organic frameworks with pores of radically varying sizes and shapes, and surface areas spanning two orders of magnitude. Interpenetrated networks have been generated that weave together multiple structures,[21] and multivariate metal–organic frameworks have combined diverse organic ligands into the same structure to impart functional heterogeneity to the material.[22] Structurally dynamic frameworks have been discovered, which respond to external stimuli by reversibly changing shape,[23] as described in detail in Chapters 2-4. Taken together, the myriad structures reported to date provide an elegant demonstration of the synthetic tunability of metal–organic frameworks.

1.4. Metal–organic Frameworks for Gas Adsorption Applications

The gas adsorption applications for which metal–organic frameworks have been studied are numerous, ranging from chemically inert noble gases to toxic, reactive agents. This dissertation is focused on the adsorption of N_2, H_2, CH_4, and CO_2, gases that play large roles in energy production and global warming. Hundreds of studies have been carried out to investigate metal–organic frameworks' ability to store or separate some combination of these four gases. The questions considered in detail herein revolve around fundamental structural changes induced in metal–organic frameworks by the adsorption of these gases, rather than the immediate industrial applicability of these frameworks. However, some metal–organic frameworks have indeed shown great promise as adsorbents for real-world applications. One such material is the metal–organic framework Co(bdp) (bdp^{2-} = 1,4-benzenedipyrazolate), which exhibits record-high CH_4 capacity at room temperature and is discussed in further detail below.[24] Due to its remarkable methane storage properties and unique structural features Co(bdp) serves as the inspiration for the research described in Chapters 2-4.

1.5. Structurally Flexible Metal–organic Frameworks

Because of their characteristic arrangement of metal ions and organic linkers that form porous, repeating subunits, metal–organic frameworks comprise a structurally unique class of crystalline materials that have attracted great attention from the crystallographic community. However, a subclass of metal–organic frameworks possesses an additional structural feature: flexible metal–organic frameworks can reversibly change shape in response to external stimuli. These flexible frameworks undergo conformational changes that increase or decrease the dimensions of one or more crystallographic axes along with the overall unit cell volume when triggered by an external factor such as gas pressure. The structural expansions or contractions are then reversed when the external condition is removed, a phase change that is often accompanied by hysteresis.[25]

The origins of such structural flexibility vary among different metal–organic frameworks. In some cases, the organic ligands contain sites of flexibility such as single carbon-carbon bonds that can freely rotate to access different overall crystal conformations.[26] Interpenetrated frameworks can expand or contract when inter-framework contacts such as Van der Waals forces are formed or broken.[21] In other cases, the metal nodes of the framework act as hinges, as the arrangement of their ligand coordination sphere distorts, thus allowing extended flexing of the structure.[27] Often, structural flexibility is a result of a combination of these and other factors, and the exact atom(s) or bond(s) giving rise to the flexibility can be difficult to tease out. However, by combining targeted functionalization of the framework with subsequent crystallographic characterization, major sources of flexibility can be identified and controlled, as demonstrated in Chapter 2.[28]

Interpenetration of both two-dimensional sheets and three-dimensionals structures has been leveraged effectively to generate structurally flexible metal–organic frameworks. Kitagawa and coworkers combined Cu(II) ions, multitopic carboxylate-based ligands, and 4,4'-bipyridine (bpy) struts to build interpenetrated frameworks that showed structurally dynamic behavior (Figure 1.7).[29] Upon increasing N_2 pressure, the adjacent layers of the interpenetrated frameworks were forced apart, disrupting the stabilizing $\pi-\pi$ interactions between the layers and replacing these interactions with N_2–framework contacts. This adsorption-induced flexibility was replicated in various similar Cu(II)–bpy frameworks and under multiple gases, including O_2, CO_2, and CH_4.[23,30]

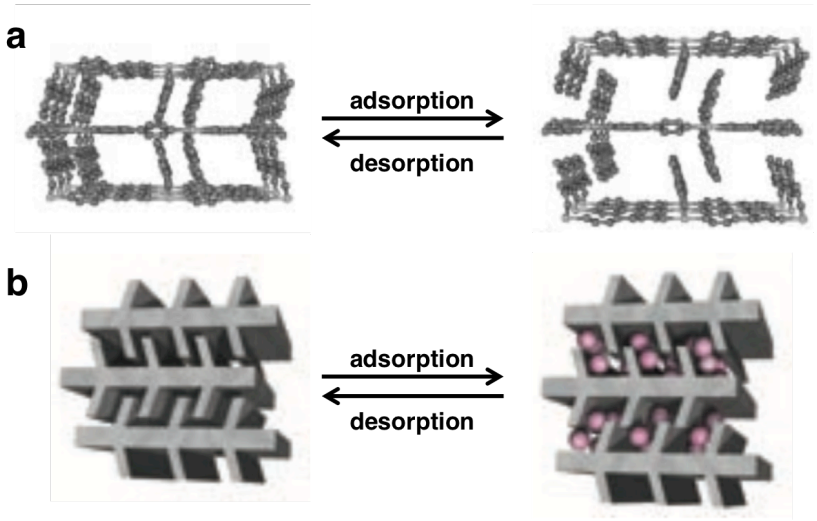

Figure 1.7. Crystal structures (a) and illustration (b) of an adsorption-induced structural phase change in a flexible metal–organic framework. Adapted from Refs. 23 and 29.

The MIL-53 series of metal–organic frameworks provides another important example of reversible structural flexibility. First reported by Férey and coworkers in 2002,[31] this family of materials is composed of chains of trivalent metal ions linked by 1,4-benzenedicarboxylate molecules (Figure 1.8). The resulting 3-dimensional network is capable of expanding and contracting via changing bond angles of the ligands around the

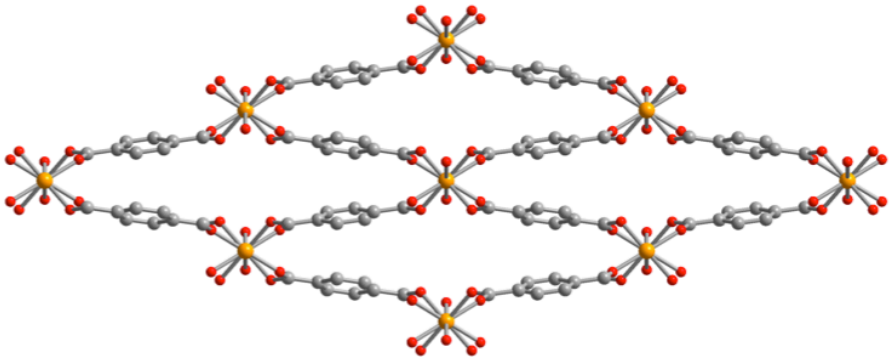

Figure 1.8. Crystal structure of Fe(OH)(bdc) (bdc^{2-} = 1,4-benzenedicarboxylate), also called Fe-MIL-53. Adapted from Ref. 27.

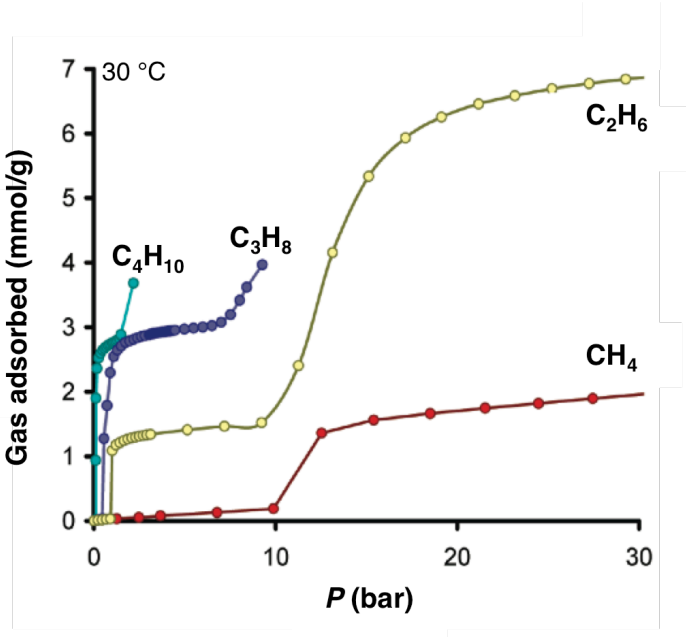

Figure 1.9. CH_4, C_2H_3, C_3H_8, and C_4H_{10} isotherms at 30 °C for Fe-MIL-53. Adapted from Ref. 32.

metal center, similar to the motion of an accordion, and this flexibility is strongly dependent on the identity of the metal center.[27]

But whether the flexibility of a metal–organic framework arises from intraframework π– π interactions, rotations around single bonds in the ligands, changes in the bond angles around the metal centers, or a combination of these and other effects, the structural phase changes observed in these frameworks are often the result of changes in the ambient gas pressure. For example, Férey and coworkers have demonstrated adsorption-induced phase changes in MIL-53 frameworks resulting from exposure to CO_2, CH_4, C_2H_3, C_3H_8, and C_4H_{10}, as well as other adsorbates (Figure 1.9).[32,33] The energetically favorable interaction between a gas molecule and the surface of a flexible metal–organic framework serves to stabilize an alternative conformation that is not the most thermodynamically stable structure when under vacuum.[34] This effect is often

adsorbate-dependent, as some adsorbate molecules have greater stabilizing power than others for a given conformation, and consequently flexible frameworks can be very effective at separating mixtures of gases, as discussed in Chapter 3.

Like MIL-53, Co(bdp) is a flexible metal–organic framework with a wine rack-type structure that undergoes reversible, adsorption-induced phase changes. Under vacuum, Co(bdp) collapses to a nonporous phase, and it expands to a series of increasingly porous intermediates when exposed to solvent or gas. This framework expands to different phases depending on the nature of the adsorbate, as has been demonstrated for N_2, O_2, H_2, CH_4, and CO_2 at a wide range of temperatures and pressures.[35,36] The high adsorption capacities and extreme volume changes exhibited by Co(bdp) make it an ideal system for study as well as for use in gas adsorption applications, as discussed below.

1.6. Methane Storage in Co(bdp)

The primary component of natural gas, CH_4, is an abundant and cleaner-burning alternative to gasoline as a transportation fuel. However, unlike liquid hydrocarbon fuels, CH_4 is a gas at standard conditions, and consequently the energy density of CH_4 is orders of magnitude lower than that of gasoline. This low energy density presents a major problem for the use of CH_4 to fuel vehicles, as any transportation fuel must be stored on board the vehicle in question. To date, CH_4 storage on board buses and trucks is accomplished by either compression or liquefaction, which entail reinforced spherical fuel tanks and/or cryogenic temperatures, respectively. These costly engineering measures have proved a prohibitive constraint for smaller vehicles and have prevented the widespread adoption of CH_4-fueled cars.[8]

Adsorption onto a porous solid offers an appealing alternative storage method for CH_4, as an effective adsorbent can increase the density of CH_4 to desired levels without the use of extreme pressures or temperatures (as shown in Figure 1.2). Metal–organic frameworks have been shown to be promising CH_4 storage materials, with high CH_4 capacities and binding enthalpies within the optimal range of –15 to –25 kJ/mol.[37] The metal–organic framework HKUST-1 ($Cu_3(btc)_2$; btc^{3-} = 1,3,5-benzenetricarboxylate) combines several important advantages of metal–organic frameworks as CH_4 adsorbents: this material possesses exposed Cu^{2+} cations capable of strongly polarizing CH_4, it contains binding pockets perfectly sized to stabilize a CH_4 molecule, it is stable to air and water, and its synthesis is straightforward and inexpensive.[37]

In spite of these numerous advantages, the usable CH_4 capacity of HKUST-1 suffers from a drawback inherent to the operation of a fuel tank. Because a vehicle requires a certain minimum CH_4 pressure in the fuel tank to operate, it must be re-fueled whenever the CH_4, pressure reaches this minimum. For the case of CH_4-fueled cars, this minimum desorption pressure is 5 bar at 25 °C. Because HKUST-1 adsorbs significant CH_4 at this pressure, the working capacity of HKUST-1 is greatly diminished (see Figure 1.10a). Consequently, a further criteria for an ideal CH_4 adsorbent is that it have minimal adsorption at 5 bar while still reaching a high saturation CH_4 capacity.[24]

The flexible nature of Co(bdp) provides the perfect isotherm shape for this application, as the collapsed form of Co(bdp) that exists under vacuum admits minimal CH_4, but after reaching a certain threshold pressure, the framework expands to a phase

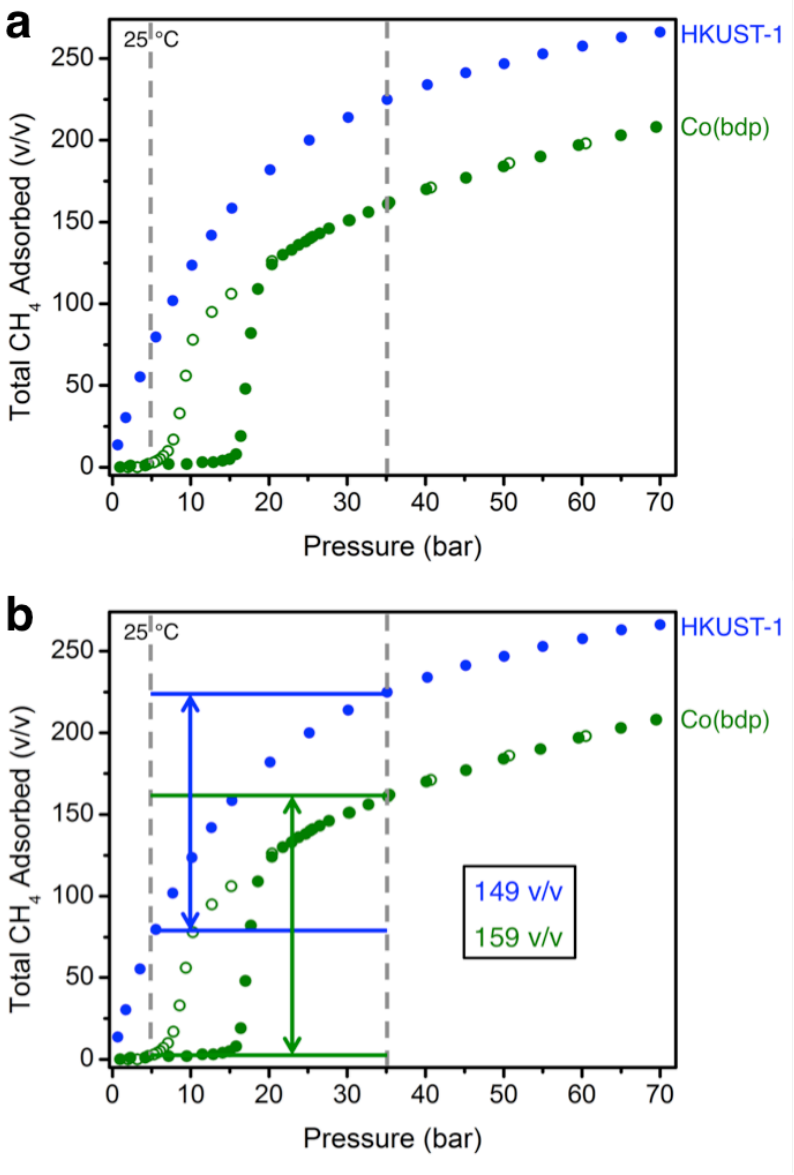

Figure 1.10. a) CH_4 isotherms at 25 °C for HKUST-1 and Co(bdp), with the industrially-relevant adsorption and desorption pressures illustrated with gray dotted lines. b) Usable CH_4 capacities of HKUST-1 and Co(bdp) illustrated on the same plot shown in part (a). Adapted from Ref. 24.

with a large CH_4 capacity (Figure 1.10b). Because the steps in the adsorption and desorption isotherms occur within the industrially-relevant fueling window of 5–35 bar at 25 °C, the CH_4-induced phase change allows Co(bdp) to achieve a usable CH_4 capacity greater than that of HKUST-1. In addition to this boost in usable CH_4 capacity, the CH_4-induced phase change bestows another significant advantage on Co(bdp): because this phase change is endothermic, it offsets much of the heat released upon CH_4 adsorption (that would otherwise have to be mitigated by an external heat exchanger of some kind).[24] The outstanding CH_4 storage performance of Co(bdp) and its structurally-unique mechanism provide the starting point for the investigations described in Chapters 2-4.

1.7. References

(1) Keller, J.; Staudt, R. *Gas Adsorption Equilibria;* Springer: New York, 2005.
(2) Zhao, G.; Wu, X.; Tan, X.; Wang, X. *Open Colloid Sci. J.* **2011**, *4*, 19.
(3) Bai, P.; Jeon, M. Y.; Ren, L.; Knight, C.; Deem, M. W.; Tsapatsis, M.; Siepmann, J. I. *Nat. Commun.* **2016**, *6*, Article number 5912.
(4) Lozano-Castelló, D.; Cazorla-Amorós, D.; Linares-Solano, A. *Energy Fuels* **2002**, *16*, 1321.
(5) Kapelewski, M. T.; Geier, S. J.; Hudson, M. R.; Stuk, D.; Mason, J. A.; Nelson, J. N.; Xiao, D. J.; Hulvey, Z.; Gilmour, E.; FitzGerald, S. A.; Head-Gordon, M.; Brown, C. M.; Long, J. R. *J. Am. Chem. Soc.* **2014**, *136*, 12119.
(6) Sircar, S. *Ind. Eng. Chem. Res.* **1992**, *31*, 1813.
(7) Herm, Z. R.; Krishna, R.; Long, J. L. *Microporous Mesoporous Mater.* **2012**, *151*, 481.
(8) Service, R. F. *Science* **2014**, *346*, 538.
(9) U. S. Department of Energy. Materials for Separation Technology: Energy and Emission Reduction Opportunities (2005).
(10) Scholl, D. S.; Lively, R. P. *Nature* **2016**, *532*, 435.
(11) Sevilla, M.; Mokaya, R. *Energy Environ. Sci.* **2014**, *7*, 1250.
(12) Allen, S. J.; Whitten, L. *Dev. Chem. Eng. Mineral Process.* **1998**, *6*, 231.
(13) Matranga, K. R.; Myers, A. L.; Glandt, E. D. *Chem. Eng. Sci*. **1992**, *47*, 569.
(14) Baerlocher, C.; McCusker, L. B.; Olson, D. H. *Atlas of Zeolite Framework Types*; Elsevier: Amsterdam, 2007.
(15) Jha, B.; Singh, D. N. Basics of Zeolites. In *Fly Ash Zeolites*; Springer: Singapore, 2016.
(16) Mazur, M.; Wheatley, P. S.; Navarro, M.; Roth, W. J.; Položij, M; Mayoral, A.; Eliášová, P.; Nachtigall, P.; Čejka, J.; Morris, R. E. *Nat. Chem.* **2016**, *8*, 58.
(17) Li, H.; Eddaoudi, M.; O'Keefe, M.; Yaghi, O. M. *Nature* **1999**, *402*, 276.
(18) Zhou, H.-C.; Long, J. R.; Yaghi, O. M. *Chem. Rev.* **2012**, *112*, 673.
(19) Farha, O. K.; Eryazici, I.; Jeong, N. C.; Hauser, B. G.; Wilmer, C. E.; Sarjeant, A. A.; Snurr, R. Q.; Nguyen, S. T.; Yazaydin, A. Ö; Hupp, J. T. *J. Am. Chem. Soc.*, **2012**, *134*, 15016.
(20) Eddaoudi, M.; Kim, J.; Rosi, N.; Vodak, D.; Wachter, J.; O'Keeffe, M.; Yaghi, O. M. *Science* **2002**, *295*, 469.
(21) Chen, B. L.; Liang, C.; Yang, J.; Contreras, D. S.; Clancy, Y. L; Lobkovsky, E. B.; Yaghi, O. M.; Dai, S. *Angew. Chem. Int. Ed.* **2006**, *45*, 1390.
(22) Kong, X.; Deng, H.; Yan, F.; Kim, J.; Swisher, J. A.; Smit, B.; Yaghi, O. M.; Reimer, J. A. *Science* **2013**, *341*, 882.
(23) Horike, S.; Shimomura, S.; Kitagawa, S. *Nat. Chem.* **2009**, *1*, 695.
(24) Mason, J. A.; Oktawiec, J.; Taylor, M. K.; Hudson, M. R.; Rodriguez, J.; Bachman, J. E.; Gonzalez, M. I.; Cervellino, A.; Guagliardi, A.; Brown, C. M.; Llewellyn, P. L.; Masciocchi, N.; Long, J. R. *Nature* **2015**, *527,* 357.
(25) Schneemann, A.; Bon, V.; Schwedler, I.; Senkovska, I.; Kaskel S.; Fischer R. A. *Chem. Soc. Rev.* **2014**, *43*, 6062.

(26) Mukherjee, S.; Joarder, B.; Manna, B.; Desai, A.; Chaudhari, A. K.; Ghosh ,S. K. *Sci. Rep.* **2014**, *4*, Article number 5761.
(27) Millange, F.; Guillou, N.; Walton, R. I.; Grenèche, J.-M.; Margiolaki, I.; Férey, G. *Chem. Commun.* **2008**, 4732.
(28) Taylor, M. K.; Runčevski, T.; Oktawiec, J.; Gonzalez, M. I.; Siegelman, R. L.; Mason, J. A.; Ye, J.; Brown, C. M.; Long, J. R. *J. Am. Chem. Soc.* **2016,** *138,* 15019.
(29) Kitagawa, S.; Kitaura, R.; Noro, S. *Angew. Chem. Int. Ed.* **2004**, *43*, 2334.
(30) Kitaura, R.; Seki, K.; Akiyama, G.; Kitagawa, S. *Angew. Chem. Int. Ed.* **2003**, *42*, 428.
(31) Serre, C.; Millange, F.; Thouvenot, C.; Nougès, M.; Marsolier, G.; Louër, D.; Férey, G. *J. Am. Chem. Soc.*, **2002**, *124*, 13519.
(32) Llewellyn, P. L.; Horcajada, P.; Maurin, G.; Devic, T.; Rosenbach, N.; Bourrelly, S.; Serre, C.; Vincent, D.; Loera-Serna, S.; Filinchuk, Y.; Férey, G. *J. Am. Chem. Soc.* **2009**, *131*, 13002.
(33) Hamon, L.; Llewellyn, P. L.; Devic, T.; Ghoufi, A.; Clet, G.; Guillerm, V.; Pirngruber, G. D.; Maurin, G.; Serre, C.; Driver, G.; van Beek, W.; Jolimaître, E.; Vimont, A.; Daturi, M; Férey, G. *J. Am. Chem. Soc.* **2009,** *131,* 17490.
(34) Coudert, F.-X.; Mellot-Draznieks, C.; Fuchs, A. H.; Boutin, A. *J. Am. Chem. Soc.* **2009,** *131,* 11329.
(35) Choi, H. J.; Dincă, M.; Long, J. R. *J. Am. Chem. Soc.* **2008**, *130*, 7848.
(36) Herm, Z. R.; Swisher, J. A.; Smit, B.; Krishna, R.; Long, J. R. *J. Am Chem. Soc.* **2011,** *133,* 5664.
(37) Mason, J. A.; Veenstra, M.; Long, J. R. *Chem. Sci.* **2014**, *5*, 32.

Chapter 2: Tuning the Adsorption-Induced Phase Change in the Flexible Metal–Organic Framework Co(bdp)

2.1. Introduction

Metal–organic frameworks are a unique class of three-dimensional materials composed of metal ions linked by multitopic organic ligands, which are notable for their crystallinity, porosity, and synthetic tunability.[1-11] Certain metal–organic frameworks also demonstrate structural flexibility, reversibly responding to external stimuli, such as changes in temperature or gas pressure.[12-28] Flexible frameworks that collapse under reduced gas pressure and expand under increasing pressure are particularly promising for gas storage applications, because of the unique shape of their adsorption isotherms. These materials adsorb minimal gas below the phase change pressure and then exhibit an abrupt rise or 'step' in adsorption upon undergoing the phase change. This drastic change in adsorption behavior can lead to enhanced selectivities, high usable storage capacities, and reduced thermal management requirements.[29-33] A handful of recent studies have found that, particularly in the case of the metal–organic framework MIL-53, changing the ligand functionality alters the step pressure.[34-41] In general, for a given family of flexible metal–organic frameworks, identification of the structural features that give rise to the phase change should allow the pressure at which this step occurs in the adsorption isotherm to be tuned through chemical design.

A promising system for such a structure-property relationship study is the flexible metal–organic framework Co(bdp) (bdp^{2-} = 1,4-benzenedipyrazolate).[17,23] This material features a record-high usable capacity for methane storage due to a sharp step at 18 bar in its high-pressure (0-70 bar) CH_4 adsorption isotherm, which results from a structural transition from a collapsed phase to an expanded phase under increasing gas pressure. This expansion is also endothermic, endowing the framework with the ability to provide intrinsic thermal management.[33] However, potential gains in CH_4 thermal management and usable capacity are only realized if the operating pressure range for a given application spans the spread of the isotherm step. For example, many CH_4 sources emit CH_4 at pressures well below 18 bar, including low-pressure natural gas formations and biogas generation facilities.[42-46] To achieve on-site CH_4 storage or transport to processing facilities without costly initial compression would require an adsorbent for which the phase change occurs at lower pressures than that of Co(bdp). Alternatively, for the material to be suitable for storage of a more weakly interacting gas such as hydrogen,[47-52] or a more strongly interacting gas such as carbon dioxide,[53-58] the adsorption step position must be shifted accordingly. Therefore, the ability to tune the phase change pressure of a flexible adsorbent like Co(bdp) through synthesis is vital to the industrial application of these materials.

In the collapsed phase of Co(bdp), edge-to-face π–π interactions between the aryl rings of neighboring bdp^{2-} ligands likely contribute to the stability of the collapsed phase at low gas pressures and affect the energy required to expand the framework.[33,59-65] We hypothesized that introduction of different functional groups on the central ring of bdp^{2-} would alter the strength of these interactions and therefore alter the minimum CH_4 pressure necessary to produce the isotherm step. In particular, we anticipated that

increasing the strength of the edge-to-face interactions would lead to higher step pressures, while decreasing their strength would lead to lower step pressures.

Herein, we demonstrate control over the phase change pressure via systematic ligand modification in a new series of functionalized Co(bdp) frameworks. X-ray diffraction studies and low-pressure N_2 adsorption measurements indicate that all new derivatives are isoreticular to Co(bdp) and exhibit similar structural flexibility. To study the effects of ligand functionalization, CH_4 was used as a probe molecule for high-pressure adsorption measurements and *in situ* powder x-ray diffraction experiments, allowing us to rationalize changes in step pressures relative to the non-functionalized framework. Because the operating conditions for industrial gas adsorption applications vary widely, this ability to systematically tune the position of an isotherm step is of tremendous advantage in facilitating the design of new adsorbents. Moreover, the synthetic approach outlined here can likely be applied to other flexible metal–organic frameworks and gases, enabling materials scientists to design phase-change adsorbents for specific applications.

2.2. Experimental Section

Unless otherwise stated, all manipulations were performed under an Ar or N_2 atmosphere in a Vacuum Atmospheres glovebox or using standard Schlenk techniques. Anhydrous *N,N*-dimethylformamide (DMF) and anhydrous dichloromethane (CH_2Cl_2) were obtained from a JC Meyer solvent system. All other reagents were obtained from commercial vendors and used as received.

Synthesis of H_2bdp Derivatives. The ligand 1,4-benzenedipyrazole (H_2bdp) was synthesized according to a previously reported procedure.[17] Complete synthetic details and characterization for all other functionalized H_2bdp derivatives are provided in the Supporting Information, while a general procedure is given below. The functionalized dibromobenzene analogues used were 1,4-dibromo-2-fluorobenzene, 1,4-dibromo-2,5-difluorobenzene, 1,4-dibromo-2,3-difluorobenzene, 1,4-dibromobenzene-d_4, or 1,4-dibromo-2,5-dimethylbenzene.

Functionalized 1,4-dibromobenzene (8.00 mmol, 1.00 equiv), 1-(2-tetrahydropyranyl)-1*H*-pyrazole-4-boronic acid pinacol ester (5.56 g, 20.0 mmol, 2.50 equiv), and K_3PO_4 (8.48 g, 40.0 mmol, 5.00 equiv) were suspended in toluene (16 mL) in a 40-mL glass scintillation vial equipped with a magnetic stir bar, which was then sparged with Ar for 10 min. The vial was uncapped quickly to add XPhos Pd G2[66] (1.26 g, 1.60 mmol, 0.200 equiv) and then briefly purged with Ar, sealed with a PTFE-lined cap, and heated to 110 °C with stirring for 2 days. After 2 days, the reaction mixture was cooled to room temperature, exposed to air, concentrated under reduced pressure, and diluted with 250 mL of diethyl ether. The ether layer was then washed with saturated aqueous $NaHCO_3$ (5 × 250 mL), dried over $MgSO_4$, and concentrated under reduced pressure to yield a yellow oil, which was used in the subsequent reaction without additional purification. The crude ligand was then dissolved in 60 mL of methanol in a 250-mL round-bottom flask equipped with a magnetic stir bar. To this flask was added 12 mL of concentrated aqueous HCl, and the reaction mixture was stirred at 50 °C for 2 h, during which time a white precipitate formed. The reaction mixture was then filtered, and

the filtrate was suspended in water and neutralized with $NaHCO_3$. The precipitate was isolated in a second filtration, washed with water, and dried under reduced pressure to yield a white or beige powder.

Synthesis of Co(bdp) Derivatives. The compound Co(bdp) and all Co(bdp) derivatives were synthesized using a strategy adapted from a previous report.[17] Specifically, a 100-mL solvent bomb was charged with a magnetic stir bar, $Co(CF_3SO_3)_2$ (0.72 g, 2.0 mmol, 1.1 equiv), H_2bdp or H_2bdp derivative (1.9 mmol, 1.0 equiv), and 10 mL *N,N*-diethylformamide (DEF). The mixture was degassed using 5 freeze–pump–thaw cycles and then sealed by closing the stopcock of the solvent bomb while the frozen reaction mixture remained under vacuum. The solvent bomb was then heated at 160 °C for 3 days to afford a purple microcrystalline solid. Upon completion of the reaction, the solvent bomb was backfilled with Ar, the supernatant was removed under positive Ar pressure and discarded, and 80 mL of anhydrous DMF was added to the solid product under an Ar atmosphere. The solvent bomb was then sealed under Ar and heated to 110 °C overnight. This solvent-exchange procedure was performed once daily for 7 days to completely remove unreacted starting material from the pores. Subsequently, the DMF was replaced with anhydrous CH_2Cl_2 following the same procedure but without heating. These CH_2Cl_2 exchanges were performed once daily for 3 days to allow activation from a lower-boiling solvent. To activate the material, the CH_2Cl_2 was evaporated under positive Ar pressure until 25 mL of solution remained. The resultant slurry was transferred to a 100-mL Schlenk flask under inert atmosphere, and the CH_2Cl_2 was evaporated over the course of 1 h under a flow of Ar at room temperature. The resultant solid was dried under a flow of Ar at 160 °C for 6 h and then placed under dynamic vacuum at 160 °C overnight. The activated solid was immediately transferred to a glovebox and handled under a dinitrogen atmosphere for all further experiments.

Single-Crystal and Powder X-ray Diffraction. All single-crystal x-ray diffraction data were collected at Beamline 11.3.1 at the Advanced Light Source, Lawrence Berkeley National Laboratory, using synchrotron radiation (λ = 0.7749 Å for Co(bdp), Co(D_4-bdp), and Co(F-bdp); λ = 0.8856 for Co(*o*-F_2-bdp) and Co(*p*-F_2-bdp)) with a Bruker PHOTON100 CMOS detector on a D8 diffractometer. The samples were held at the experimental temperature under N_2 using an Oxford Cryosystems cryostream during data collection.

High-resolution powder x-ray diffraction patterns of the samples were collected at the Beamline 17-BM at the Advanced Photon Source of Argonne National Laboratory with an average wavelength of 0.72768 Å. Scattered intensity was recorded by Perkin Elmer α-Si Flat Panel detector. Prior to measurement, the samples were packed in borosilicate glass capillaries of 1 mm diameter (Hilgenberg glass No. 50) under an N_2 atmosphere, and the capillaries were then attached to a gas-dosing manifold for *in situ* diffraction measurements. For each sample, diffraction patterns were collected at room temperature under dynamic vacuum to obtain the structure of the material in the collapsed phase. For Co(*p*-F_2-bdp), the gas-dosing manifold was then used to increase CH_4 pressure in increments of approximately 3 bar from 0 bar to 19.7 bar, and diffraction data for each pressure was collected after reaching equilibrium (evidenced by a constant

pressure readout and diffraction pattern). Analysis of all diffraction data, including structure solution and refinement, is discussed in the Supporting Information.

Gas Adsorption. Nitrogen adsorption isotherms for pressures in the range of 0-1.1 bar were measured using a Micromeritics ASAP 2020 or 2420 gas adsorption analyzer. Activated samples were transferred under a N_2 atmosphere to preweighed analysis tubes, which were capped with a Transeal. Each sample was evacuated on the instrument until the outgas rate was less than 3 μbar/min. The evacuated analysis tube containing degassed sample was then carefully transferred to an electronic balance and weighed to determine the mass of sample (typically 30-50 mg). The tube was then fitted with an isothermal jacket and transferred back to the analysis port of the instrument. The outgas rate was again confirmed to be less than 3 μbar/min. Nitrogen adsorption isotherms were measured at 77 K using a liquid N_2 bath.

Methane adsorption isotherms for pressures in the range of 0–70 bar were measured on an HPVA-II-100 gas adsorption analyzer from Particulate Systems, a Micromeritics company. In a typical measurement, 0.2-0.5 g of activated sample was loaded into a tared stainless steel sample holder inside a glovebox under a N_2 atmosphere. Prior to connecting the sample holder to the VCR fittings of the complete high-pressure assembly inside the glovebox, the sample holder was weighed to determine the sample mass. The sample holder was then transferred to the HPVA-II-100, connected to the analysis port of the instrument via an OCR fitting, and evacuated at room temperature for at least 2 h. The sample holder was then placed inside an aluminium recirculating dewar connected to a Julabo FP89-HL isothermal bath filled with Julabo Thermal C2 fluid. The temperature stability of the isothermal bath was ±0.02 °C. Methods for accurately measuring the relevant sample freespaces, which involve the expansion of He from a calibrated volume at 0.7 bar and 25 °C to the evacuated sample holder, have been described in detail previously.[106] Non-ideality corrections were performed using the CH_4 compressibility factors tabulated in the NIST REFPROP database[67] at each measured temperature and pressure.

2.3. Results and Discussion

Synthesis of Functionalized Co(bdp) Derivatives. Variants of the H_2bdp ligand with methyl, deuterium, or fluorine functionalities on the central ring were synthesized to investigate how changing the non-covalent interactions between linkers in the collapsed Co(bdp) phase might influence adsorption-induced structural changes. Specifically, the selected groups were expected to show increased, similar, or decreased electrostatic affinities for the π cloud of a neighboring aryl ring, respectively.[59-65,68-74] This array of dipyrazole ligands was realized by coupling protected pyrazoleboronic esters to a variety of commercially available dibromobenzenes (Scheme 2.1), thus enabling late-stage diversification. Initial attempts to accomplish this coupling with $Pd(PPh_3)_4$ required large amounts of the catalyst, high reaction temperatures, and long reaction times, and still resulted in low yields and incomplete conversions. This inefficiency was especially true of the multiply-fluorinated substrates; for example, the synthesis of H_2(*o*-F_2-bdp) required the gradual addition of 0.6 equivalents of $Pd(PPh_3)_4$ over the course of eight days of heating at reflux. In turn, the liberal use of $Pd(PPh_3)_4$ led to an abundance of PPh_3O

Scheme 2.1. Synthesis of H_2bdp derivatives.

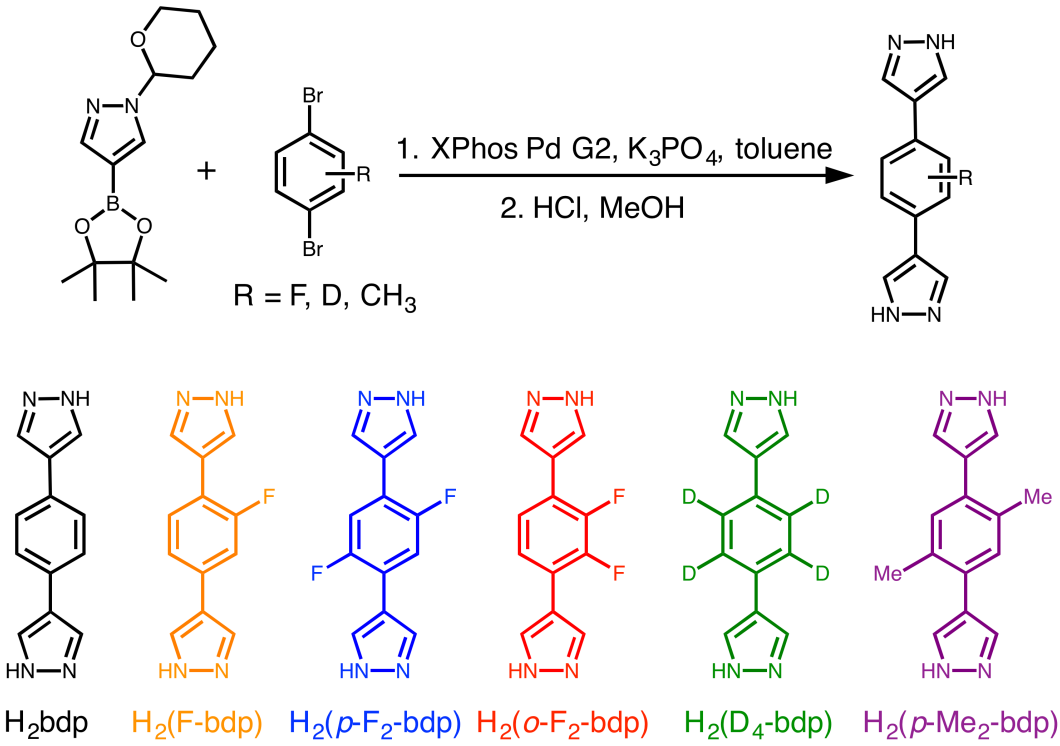

by-product, which was difficult to remove completely from the desired product via chromatography. In order to improve the syntheses and minimize impurities carried forward, we optimized the coupling reaction conditions through a series of trials and ultimately adopted XPhos Pd G2[66] as a catalyst in place of $Pd(PPh_3)_4$. Although a minimum of 0.2 equivalents of catalyst was still necessary for the synthesis of the fluorinated H_2bdp derivatives, this route afforded improved yields and reduced reaction times (see the Supporting Information for full experimental details).

The corresponding Co(bdp) derivatives were synthesized by reaction of $Co(CF_3SO_3)_2$ with the respective ligands in sealed vessels with *N,N*-diethylformamide (DEF), and after heating at 160 °C for 3 days, the desired frameworks were obtained as dark purple crystalline solids. It was found that in comparison to the parent framework, the fluorinated derivates are much more air-sensitive. Framework degradation was evidenced by formation of pink, red, or brown solids that were shown to be amorphous by powder x-ray diffraction. In addition to this color change and loss of crystallinity, pre-step adsorption in subsequent CH_4 adsorption isotherms was often a sign that a material was of insufficient quality (Figure 2.S20). Sample degradation occurred frequently during post-synthetic solvent exchanges in particular, and this degradation was ultimately overcome by carrying out all exchanges using anhydrous solvent and rigorous Schlenk techniques, precautions that are unnecessary for Co(bdp). We also note that fluorination of H_2bdp reduces the solubility of the ligand in DMF, and thus more extensive solvent exchanges are necessary to remove unreacted materials from the pores of the resulting metal-organic framework.

After optimization of the synthesis conditions for all Co(bdp) derivatives, crystals suitable for single-crystal x-ray diffraction were obtained for Co(F-bdp), Co(*p*-F_2-bdp), Co(*o*-F_2-bdp), and Co(D_4-bdp) from small-scale reactions in sealed tubes. The resultant DEF-solvated crystal structures confirmed the formation of metal–organic frameworks with the same structural connectivity as Co(bdp). The as-synthesized materials adopt an expanded configuration, in which one-dimensional square channels are formed by chains of tetrahedral pyrazolate-bridged cobalt(II) centers linked on four sides by rows of bdp^{2-} ligands. As an example, a portion of the structure of the solvated Co(*p*-F_2-bdp) is depicted in Figure 2.1. Interestingly, the fluorinated aryl rings in this structure are ordered, such that fluorine atoms from one ring are oriented toward fluorine atoms on adjacent rings along the walls of the channel. The resulting C–F···F–C distance between adjacent ligands is 2.693(6) Å, slightly shorter than the mean C–F···F–C distance of 2.8 Å found in a survey of the CSD for aromatic C–F···F–C contacts below the sum of the van der Waals radii.[75,76] Thus, the overall framework geometry positions the rings at a distance compatible with typical C–F···F–C interactions and gives rise to aryl ordering in Co(*p*-F_2-bdp),[77-85] as discussed further below. Single crystals of Co(bdp) were also obtained, and improved resolution data and a better structural refinement were achieved relative to the original report[17] by collecting data at room temperature. Although a single-crystal structure determination was not obtained for Co(*p*-Me_2-bdp), its structure was confirmed to be isoreticular to that of Co(bdp) from powder x-ray diffraction data collected for the activated bulk sample (Figure 2.S6).

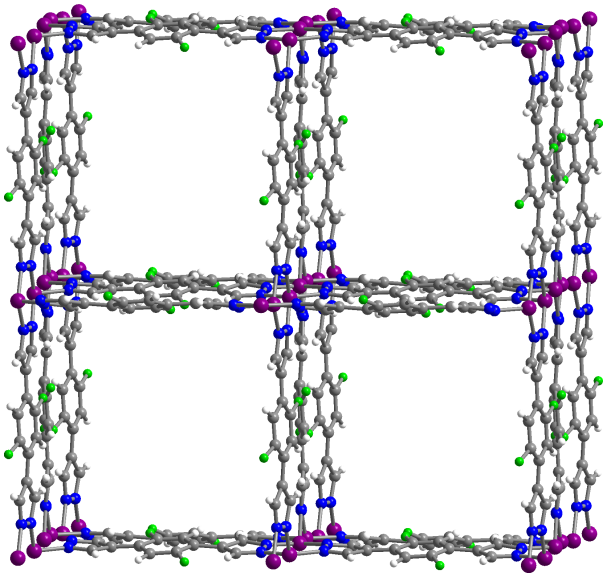

Figure 2.1. Single-crystal x-ray diffraction structure of DEF-solvated form of Co(*p*-F_2-bdp). DEF molecules in the framework pores were found to be disordered and could not be modeled successfully, and thus are not shown here. All Co(bdp) derivatives feature one-dimensional channels bounded by rows of organic ligands and chains of tetrahedral cobalt(II) ions. Gray, blue, white, purple, and green spheres represent C, N, H, Co, and F atoms, respectively.

N_2 Adsorption and Framework Flexibility. Prior to gas adsorption measurements, all frameworks were activated by heating the materials to 160 °C under dynamic vacuum to completely remove any guest solvent molecules. Low-temperature N_2 adsorption measurements were then used to assess the porosity and flexibility of the various derivatives (Figure 2.2). Similar to the N_2 isotherm of Co(bdp), the new frameworks Co(F-bdp), Co(*p*-F_2-bdp), Co(*o*-F_2-bdp), and Co(D_4-bdp) exhibit low initial N_2 uptake, followed by a series of distinct adsorption steps beginning at pressures below 3 mbar. This isotherm shape indicates that these materials are collapsed when fully evacuated, but transition to a series of expanded structures under increasing gas pressure, demonstrating that the introduction of new functional groups does not eliminate framework flexibility. The step positions in each isotherm vary among the derivatives, suggesting that the stability of each structural intermediate (and thus the N_2 pressure associated with that particular phase change) is uniquely affected by ligand functionalization. All of the aforementioned Co(bdp) derivatives reach an expanded phase with N_2 saturation capacities between 7.1 and 8.3 mol/mol, indicating that these materials have similarly high permanent porosities, with Langmuir surface areas between 2279 and 2702 m^2/g (Table 2.S3). In contrast, Co(*p*-Me_2-bdp) remains relatively nonporous until nearly 500 mbar, at which point it undergoes a phase change to reach a saturation capacity of only 5.3 mol/mol. This much higher phase change pressure suggests that the ligand methyl groups significantly stabilize a collapsed framework structure.[86-90]

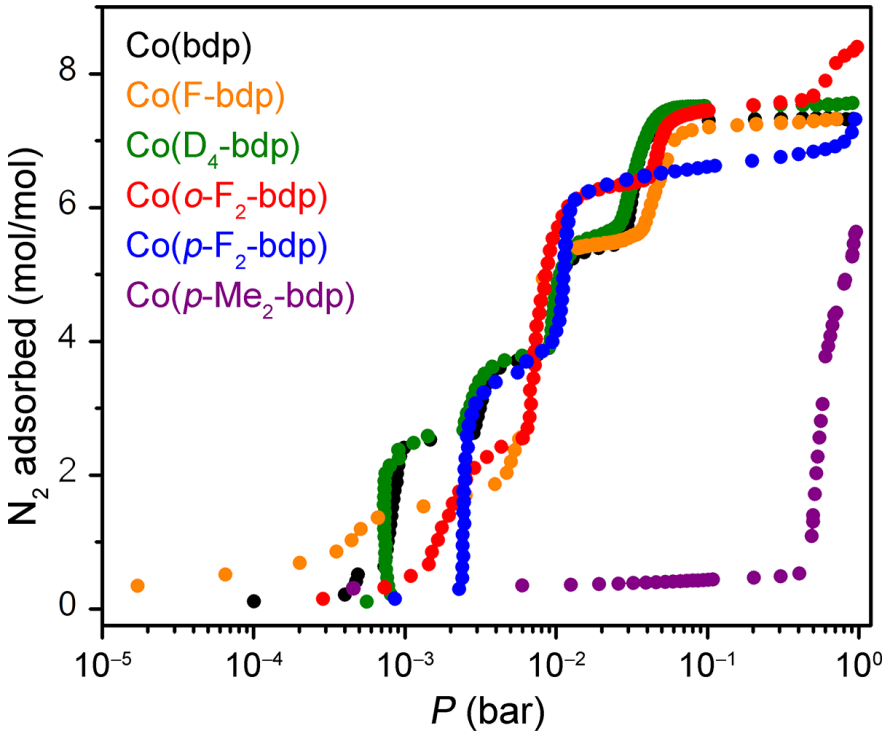

Figure 2.2. Low pressure N_2 adsorption for Co(bdp) and derivatives at 77 K. Co(bdp) adsorption (black) largely underlays Co(D_4-bdp) adsorption (green).

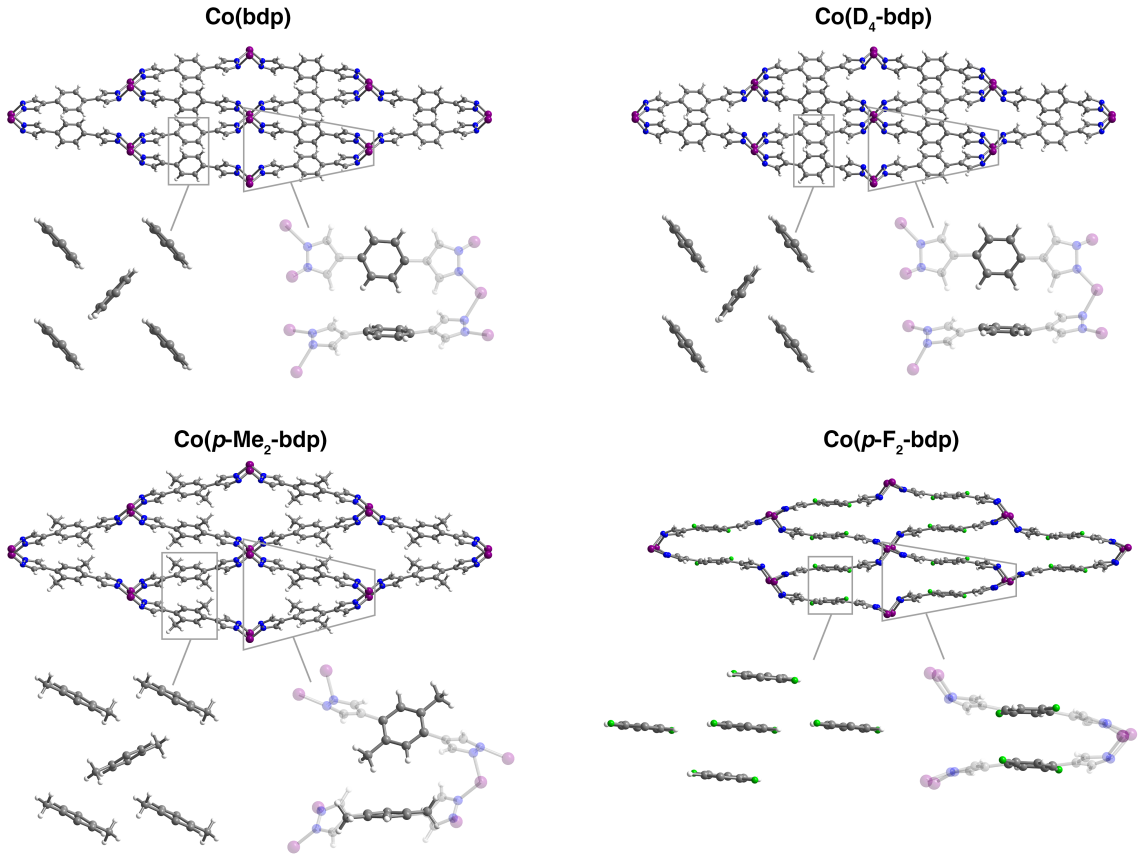

Figure 2.3. Powder x-ray diffraction structures of activated Co(bdp), Co(D_4-bdp), Co(*p*-Me_2-bdp), and Co(*p*-F_2-bdp), viewed down the pore channel. Below each structure are expanded views, highlighting interactions between the aryl rings of the frameworks. Gray, blue, white, purple, and green spheres represent C, N, H, Co, and F atoms, respectively.

Structural Characterization of Collapsed Phases. To investigate the effect of ligand functionalization on edge-to-face π–π interactions in the collapsed phases of these materials, the frameworks Co(D_4-bdp), Co(*p*-Me_2-bdp), and Co(*p*-F_2-bdp) were chosen as representatives of each type of functional group, and synchrotron powder x-ray diffraction data were collected on the activated powders while they were maintained under dynamic vacuum at room temperature. As expected, the activated structure of Co(D_4-bdp) does not exhibit noticeable differences from Co(bdp) and adopts a collapsed phase with a calculated pore volume of 0 cm^3/g.[91] While the diffraction data revealed that Co(*p*-F_2-bdp) and Co(*p*-Me_2-bdp) also adopt collapsed phases, these structures display important differences from the parent framework (Figure 2.3).

In the case of Co(*p*-Me_2-bdp), the ligands interact across the pore channel through edge-to-face π–π interactions, similar to those of Co(bdp) and Co(D_4-bdp). However, because of the steric bulk of the methyl groups, the methylated aryl rings are not able to orient perpendicularly or approach as closely as the phenyl rings in the parent framework.

Indeed, the distance between the centers of two adjacent aryl rings in Co(*p*-Me_2-bdp) is 5.6 Å, compared to 4.9 Å in Co(bdp). Consequently, Co(*p*-Me_2-bdp) retains some porosity in its collapsed phase, with a calculated accessible N_2 surface area of 59 m^2/g and pore volume of 0.021 cm^3/g[91] that is consistent with the 77 K N_2 adsorption approaching 1.5 mmol/g prior to any structural changes. Despite this increased porosity, the comparatively high expansion pressure of Co(*p*-Me_2-bdp) suggests that its collapsed phase is significantly more stable than that of the other Co(bdp) derivatives. This increased stability can be understood by considering the activated, collapsed structure: the methyl group orients two of its three hydrogen atoms toward the neighboring phenyl ring π cloud, increasing the number of electrophilic atoms engaged in the edge-to-face interaction. Furthermore, the electron-donating nature of the methyl group strengthens the edge-to-face interaction by increasing the electron density in the π cloud, as well as the electrophilicity of the edge of the ring.[68-72]

In Co(*p*-Me_2-bdp), as well as Co(bdp) and Co(D_4-bdp), the edge-to-face interactions across pore channels are facilitated by a rotation of the ligands relative to the associated chain of cobalt atoms. Alternating ligands rotate either clockwise or counterclockwise, orienting the electron-poor edge of one aryl ring towards the electron-rich *p* cloud of the next in a stabilizing electrostatic interaction (Figure 2.S10).[59-65,73,74] This orientation results in a dihedral angle between successive ligands of as large as 73.7° for Co(bdp). In the case of Co(*p*-F_2-bdp), however, this dihedral angle is only 9.7°, and edge-to-face interactions are replaced with a π-stacked configuration, wherein the fluorine atoms of one ligand sit above the hydrogen atoms of another. Thus, the introduction of electronegative fluorine atoms onto the central ligand ring in Co(*p*-F_2-bdp) decreases the electronic disparity between ring edge and face, thereby decreasing the favorability of this edge-to-face interaction.

Methane-Induced Phase Change. To evaluate the effect of ligand variation on adsorption-induced structural changes, CH_4 (the main component of natural gas) was selected as a probe molecule for high-pressure adsorption measurements. In addition to the industrial relevance of natural gas as a heating, electricity, and transportation fuel and to the growing interest in its storage in metal–organic frameworks, CH_4 was chosen as a probe because it is supercritical at ambient temperature, which avoids contributions from pore filling that might complicate structure-property investigations.[2,33,92-109]

High-pressure CH_4 adsorption isotherms were measured for all Co(bdp) derivatives from 1 bar to 70 bar at 25 °C, revealing that the introduction of various substituents indeed results in shifts in the phase change step pressure (Figures 2.4 and 2.S21). Importantly, these altered step pressures are consistent with the structural information obtained from diffraction studies. For example, the CH_4 isotherm of Co(D_4-bdp) exhibits minimal low-pressure adsorption followed by a sharp step at ~18 bar and nearly overlays with the isotherm of Co(bdp). Thus, any equilibrium isotope effect is likely to be small. In stark contrast, the CH_4 adsorption isotherm of Co(*p*-Me_2-bdp) exhibits no phase change below 70 bar (Figure 2.S22) and instead adopts a Type I shape with modest gas uptake. This behavior is indicative of a slightly porous, rigid material, consistent with the porosity observed for the activated Co(*p*-Me_2-bdp) structure. Because the low-pressure N_2 adsorption of Co(*p*-Me_2-bdp) shows that this framework is indeed flexible, we

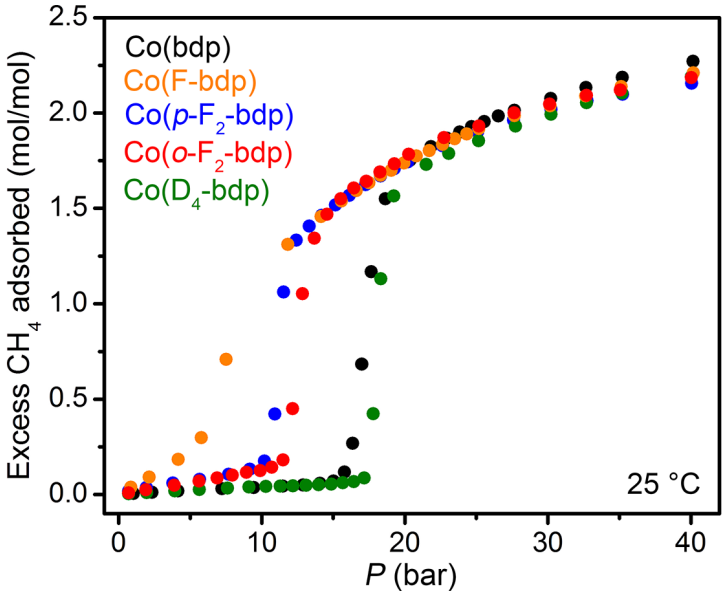

Figure 2.4. High-pressure CH_4 adsorption isotherms of Co(bdp), Co(F-bdp), Co(*p*-F_2-bdp), Co(*o*-F_2-bdp), and Co(D_4-bdp) at 25 °C.

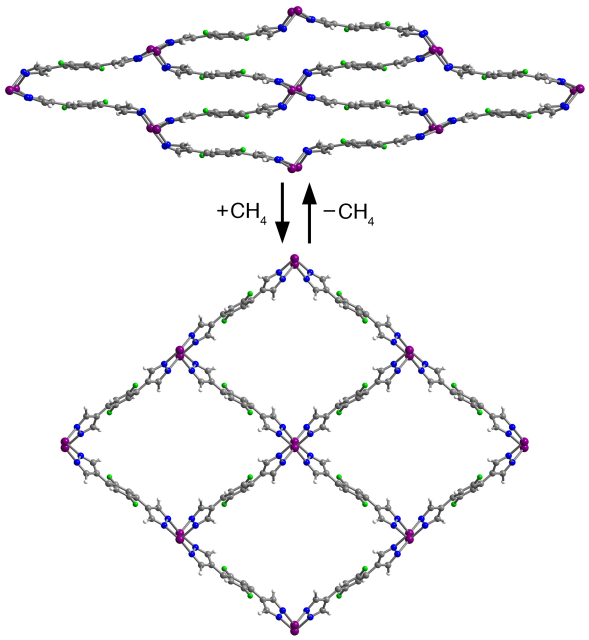

Figure 2.5. Powder x-ray diffraction structures of Co(*p*-F_2-bdp) under vacuum (top) and under 19.7 bar CH_4 (bottom). Gray, blue, white, purple, and green spheres represent C, N, H, Co, and F atoms, respectively.

hypothesize that the CH_4-induced phase change occurs at much higher pressures than in Co(bdp), as is the case for the N_2-induced phase change. Again, this result supports the conclusions drawn from the activated structure of Co(*p*-Me_2-bdp), in which the methyl groups enhance the favorable edge-to-face π–π interactions in the collapsed structure and thus stabilize this phase.

For Co(F-bdp), Co(*p*-F_2-bdp), and Co(*o*-F_2-bdp), on the other hand, the step shifts to lower CH_4 pressures relative to Co(bdp), indicating that the collapsed phase is destabilized by the introduction of fluorine atoms.[86-90] This observation is consistent with the powder diffraction data for the collapsed phase of Co(*p*-F_2-bdp), in which the stabilizing edge-to-face π–π interactions are eliminated. However, in addition to the crystal structure of the collapsed phase, a structure of the CH_4-expanded phase is necessary to fully understand how fluorination affects the step pressure. Therefore, we continued to focus on Co(*p*-F_2-bdp) as a representative of fluorine functionalization, and *in situ* diffraction studies at variable CH_4 pressures were performed on this compound.

The *in situ* diffraction patterns for Co(*p*-F_2-bdp) show that the step is indeed the result of a discrete structural phase change, in which the material expands by 103% in unit cell volume from 0 bar to 20 bar, as the calculated pore volume increases from 0 cm^3/g to 0.98 cm^3/g[91] (Figure 2.5). In contrast to the DEF-solvated structure of Co(*p*-F_2-bdp), in which fluorine atoms on adjacent rings orient toward each other, both the activated and CH_4-expanded structures show the aryl rings to order in the opposite orientation, with fluorine atoms pointing toward adjacent hydrogen atoms (Figure 2.S9). This C–H···F–C interaction has the characteristics of a weak hydrogen bond and has been shown to influence the conformation of other systems containing aryl fluorides.[110-122] Although it has been shown that C–H···F–C interactions are preferred over C–F···F–C interactions in fluorobenzenes,[123] our results suggest that the carbon-carbon distance may be an important factor in determining which interaction is most favorable. In the collapsed and CH_4-expanded phases of Co(*p*-F_2-bdp), in which the aryl rings are ordered to achieve C–H···F–C interactions, the relevant carbon atoms are separated by 4.7 Å and 4.8 Å, respectively. But in the fully-expanded, DEF-solvated structure, these carbons are 5.0 Å apart, and the aryl rings are rotated to replace the C–H···F–C interactions with C–F···F–C interactions. We note that this conclusion is not firm, however, since the disordered guest DEF molecules within the channels may also somehow be influencing the aryl ring arrangement.

Because the lateral C–H···F–C interactions are maintained when Co(*p*-F_2-bdp) undergoes the CH_4-induced phase change, only two π–π stacking interactions involving the central ring must be broken to accomplish the expansion. This is in distinct contrast to the four edge-to-face π–π interactions that must be broken in collapsed Co(bdp). Indeed, the reduction in the number of π–π interactions that must be broken in the CH_4-induced phase change is likely a key factor in the destabilization of collapsed Co(*p*-F_2-bdp) relative to Co(bdp). The destabilizing effect of fluorination extends to Co(*o*-F_2-bdp) and Co(F-bdp), which also exhibit phase changes at lower CH_4 pressures than the unfunctionalized framework. However, while both Co(*o*-F_2-bdp) and Co(*p*-F_2-bdp) undergo phase changes at ~11 bar CH_4, Co(F-bdp) expands below 8 bar, indicating that the collapsed phase of the monofluorinated derivative is less stable than that of the

difluorinated materials. This result implies that the number of fluorine atoms on the aryl ring, and not their relative location, is the dominant factor influencing the strength of π–π stacking. We note that this evidence is consistent with earlier observations[124-126] that substituents strengthen π–π stacking through local interactions with the opposing ring, rather than through their effect on the net dipole of the aryl system.

2.4. Conclusions

In this work, we used structural insights to design and synthesize a new family of isoreticular metal–organic frameworks derived from the flexible framework Co(bdp). By introducing methyl or fluoro substituents onto the central ring of the ligand, the step in the CH_4 adsorption isotherm of the parent Co(bdp) compound could be shifted to higher or lower pressures, respectively. *In situ* powder x-ray diffraction studies show that the shifts in the CH_4-induced phase change pressure are due to the enhancement or disruption of key π–π interactions in the collapsed phase of these materials. The shifts in step pressure correlate with the nature of the substituent in a predictable fashion, facilitating the design of future materials with a desired step pressure in mind. This relationship between ligand structure and phase-change pressure may also be leveraged in other flexible metal–organic frameworks, by using crystal structures of the collapsed and expanded phases to identify interactions that are formed or broken during the phase change. Although we have focused here on the edge-to-face π–π interactions present in the collapsed phase of Co(bdp), many other non-covalent, intraframework interactions may readily be targeted depending on the metal–organic framework. Once linkers have been identified that modulate the targeted interactions, the step pressure could potentially be further tuned by using a mixture of linkers to synthesize a multivariate metal-organic framework with an intermediate step pressure. Such synthetic control over the phase change pressures of flexible metal–organic frameworks is a powerful and promising tool for their application in an industrial setting.

2.5. Acknowledgements

First and foremost, I acknowledge my coauthors Tomče Runčevski, Julia Oktawiec, Miguel I. Gonzalez, Rebecca L. Siegelman, Jarad A. Mason, Jinxing Ye, Craig M. Brown, and Jeffrey R. Long. Early stages of the synthetic chemistry, including the synthesis of H_2(F-bdp) and Co(F-bdp), were supported by the U.S. Department of Energy, Advanced Research Projects Agency–Energy (ARPA-e). The remainder of the synthetic chemistry was funded by the Department of Energy, Office of Energy Efficiency and Renewable Energy, Fuel Cell Technologies Office under grant DE-AC02-05CH11231. Methane adsorption measurements and structural studies were supported by the Center for Gas Separations Relevant to Clean Energy Technologies, an Energy Frontier Research Center supported by the U.S. Department of Energy, Office of Science, Office of Basic Energy Sciences, under award DE-SC0001015. Single-crystal diffraction data were collected on the 11.3.1 Beamline at the Advanced Light Source User Facility at Lawrence Berkeley National Laboratory, which is supported by the Director, Office of Science, Office of Basic Energy Sciences, of the U.S. Department of Energy. Powder x-ray diffraction data were collected on the 17-BM Beamline at the Advanced Photon

Source, a U.S. Department of Energy Office of Science User Facility operated by Argonne National Laboratory. I thank Douglas Reed, Matthew Kapelewski, Dr. Brian Wiers, and Prof. Jiwoong Lee for helpful discussions and for experimental assistance, and Dr. Katie R. Meihaus for editorial assistance. I also thank the National Science Foundation for providing graduate fellowship support for M.K.T., J.O., and J.A.M.

2.6. References

(1) Li, H.; Eddaoudi, M.; O'Keefe, M.; Yaghi, O. M. *Nature* **1999**, *402*, 276.
(2) Eddaoudi, M.; Kim, J.; Rosi, N.; Vodak, D.; Wachter, J.; O'Keeffe, M.; Yaghi, O. M. *Science* **2002**, *295*, 469.
(3) Kitagawa, S.; Kitaura, R.; Noro, S.-I. *Angew. Chem. Int. Ed.* **2004**, *43*, 2334.
(4) Matsuda, R.; Kitaura, R.; Kitagawa, S.; Kubota, Y.; Belosludov, R. V.; Kobayashi, T. C.; Sakamoto, H.; Chiba, T.; Takata, M.; Kawazoe, Y.; Mita, Y. *Nature* **2005**, *436*, 238.
(5) Férey, G. *Chem. Soc. Rev.* **2008**, *37*, 191.
(6) Morris, R. E.; Wheatley, P. S. *Angew. Chem. Int. Ed.* **2008**, *47*, 4966.
(7) Czaja, A. U.; Trukhan, N.; Müller, U. *Chem. Soc. Rev.* **2009**, *38*, 1284.
(8) Li, J.-R.; Kuppler, R. J.; Zhou, H.-C. *Chem. Soc. Rev.* **2009**, *38*, 1477.
(9) Chen, B.; Xiang, S.; Qian, G. *Acc. Chem. Res.* **2010**, *43*, 1115.
(10) Zhou, H.-C.; Long, J. R.; Yaghi, O. M. *Chem. Rev.* **2012**, *112*, 673.
(11) Evans, J. D.; Sumby, C. J.; Doonan, C. J. *Chem. Soc. Rev.* **2014**, *43*, 5933.
(12) Kitagawa, S.; Kondo, M. *Bull. Chem. Soc. Jpn*, **1998**, *71*, 1739.
(13) Cussen, E. J.; Claridge, J. B.; Rosseinsky, M. J.; Kepert, C. J. *J. Am. Chem. Soc.* **2002**, *124*, 9574.
(14) Llewellyn, P. L.; Bourrelly, S.; Serre, C.; Filinchuk, Y.; Férey, G. *Angew. Chem. Int. Ed.* **2006**, *45*, 7751.
(15) Kondo, A.; Noguchi, H.; Carlucci, L.; Proserpio, D. M.; Ciani, G.; Kajiro, H.; Ohba, T.; Kanoh, H.; Kaneko, K. *J. Am. Chem. Soc.* **2007**, *129*, 12362.
(16) Serre, C.; Mellot-Draznieks, C.; Surblé, S.; Audebrand, N.; Filinchuk, Y.; Férey, G. *Science* **2007**, *315*, 1828.
(17) Choi, H. J.; Dincă, M.; Long, J. R. *J. Am. Chem. Soc.* **2008**, *130*, 7848.
(18) Thallapally, P. K.; Tian, J.; Kishan, M. R.; Fernandez, C. A.; Dalgarno, S. J.; McGrail, P.B.; Warren, J. E; Atwood, J. L. *J. Am. Chem. Soc.* **2008**, *130*, 16842.
(19) Férey, G.; Serre, C. *Chem. Soc. Rev.* **2009**, *38*, 1380.
(20) Horike, S.; Shimomura, S.; Kitagawa, S. *Nat. Chem.* **2009**, *1*, 695.
(21) Demessence, A.; Long, J. R. *Chem. Eur. J.* **2010**, *16*, 5902.
(22) Fernandez, C. A.; Thallapally, P. K.; Motkuri, R. K.; Nune, S. K.; Sumrak, J. C.; Tian, J.; Liu, J. *Cryst. Growth Des.* **2010**, *10*, 1037.
(23) Salles, F.; Maurin, G.; Serre, C.; Llewellyn, P. L.; Knöfel, C.; Choi, H. J.; Filinchuk, Y.; Oliviero, L.; Vimont, A.; Long, J. R.; Férey, G. *J. Am. Chem. Soc.* **2010**, *121*, 13782.
(24) Liu, Y.-Y.; Couck, S.; Vandichel, M.; Grzywa, M.; Leus, K.; Biswas, S.; Volkmer, D.; Gascon, J.; Kapteijn, F.; Denayer, J. F. M.; Waroquier, M.; Van Speybroeck, V.; Van Der Voort, P. *Inorg. Chem.* **2012**, *52*, 113.
(25) Sato, H.; Kosaka, W.; Matsuda, R.; Hori, A.; Hijikata, Y.; Belosludov, R. V.; Sakaki, S.; Takata, M.; Kitagawa, S. *Science* **2014**, *343*, 167.

(26) Schneemann, A.; Bon, V.; Schwedler, I.; Senkovska, I.; Kaskel S.; Fischer R. A. *Chem. Soc. Rev.* **2014**, *43*, 6062.
(27) Lanza, A.; Germann, L. S.; Fisch, M.; Casati, N.; Macchi, P. *J. Am. Chem. Soc.* **2015**, *137*, 13072.
(28) Sadakiyo, M.; Yamada, T.; Kato, K.; Takata, M.; Kitagawa, H. *Chem. Sci.* **2016**, *7*, 1349.
(29) (a) Kitaura, R.; Seki, K.; Akiyama, G.; Kitagawa, S. *Angew. Chem. Int. Ed.* **2003**, *42*, 428.
(30) Zhao, X.; Xiao, B.; Fletcher, A. J.; Thomas, K. M.; Bradshaw, D.; Rosseinsky, M. J. *Science* **2004**, *306*, 1012.
(31) Noguchi, H.; Kondoh, A.; Hattori, Y.; Kanoh, H.; Kajiro, H.; Kaneko, K. *J. Phys. Chem. B* **2005**, *109*, 13851.
(32) Llewellyn, P. L.; Horcajada, P.; Maurin, G.; Devic, T.; Rosenbach, N.; Bourrelly, S.; Serre, C.; Vincent, D.; Loera-Serna, S.; Filinchuk, Y.; Férey, G. *J. Am. Chem. Soc.* **2009**, *131*, 13002.
(33) Mason, J. A.; Oktawiec, J.; Taylor, M. K.; Hudson, M. R.; Rodriguez, J.; Bachman, J. E.; Gonzalez, M. I.; Cervellino, A.; Guagliardi, A.; Brown, C. M.; Llewellyn, P. L.; Masciocchi, N.; Long, J. R. *Nature* **2015**, *527,* 357.
(34) Couck, S.; Denayer, J. F. M.; Baron, G. V.; Rémy, T.; Gascon, J.; Kapteijn, F. *J. Am. Chem. Soc.* **2009***, 131,* 6326.
(35) Devic, T.; Horcajada, P.; Serre, C.; Salles, F.; Maurin, G.; Moulin, B.; Heurtaux, D.; Clet, G.; Vimont, A.; Grenéche, J.-M.; Le Ouay, B.; Moreau, F.; Magnier, E.; Filinchuk, Y.; Marrot, J.; Lavalley, J.-C.; Daturi, M; Férey, G. *J. Am. Chem. Soc.* **2010**, *132*, 1127.
(36) Horcajada, P.; Salles, F.; Wuttke, S.; Devic, T.; Heurtaux, D.; Maurin, G.; Vimont, A.; Daturi, M.; David, O.; Magnier, E.; Stock, N.; Filinchuk, Y.; Popov, D.; Riekel, C.; Férey, G.; Serre, C. *J. Am. Chem. Soc.* **2011**, *133*, 17839.
(37) Ramsahye, N. A.; Trung, T. K.; Bourrelly, S.; Yang, Q.; Devic, T.; Maurin, G.; Horcajada, P.; Llewellyn, P. L.; Yot, P.; Serre, C.; Filinchuk, Y.; Fajula, F.; Férey, G.; Trens, P. *J. Phys. Chem. C.* **2011**, *115*, 18683.
(38) Henke, S.; Schneemann, A.; Wütscher, A.; Fischer, R. A. *J. Am. Chem. Soc.* **2012**, *134*, 9464.
(39) Lescouet, T.; Kockrick, E.; Bergeret, G.; Pera-Titus, M.; Aguado, S.; Farrusseng, D. *J. Mater. Chem.* **2012**, *22*, 10287.
(40) Serra-Crespo, P.; Gobechiya, E.; Ramos-Fernandez, E. V.; Juan-Alcañiz, J.; Martinez-Joaristi, A.; Stavitski, E.; Kirschhock, C. E. A.; Martens, J. A.; Kapteijn, F.; Gascon, J. *Langmuir* **2012**, *28*, 12916.
(41) Kozachuck, O.; Meilikhov, M.; Yusenko, K.; Schneemann, A.; Jee, B.; Kuttatheyil, A. V.; Bertmer, M.; Sternemann, C.; Pöppl, A.; Fischer, R. A. *Eur. J. Inorg. Chem.* **2013**, 4546.
(42) Neumann, H.-J.; Paczynska-Lahme, B. Natural Gas. In *Ullmann's Encyclopedia of Industrial Chemistry, 5th Ed.;* Elvers, B.; Hawkins, S.; Schulz, G., Eds.; VCH: Weinheim, 1991; pp 73-124.
(43) Yadvika; Santosh; Sreekrishnan, T. R.; Kohli, S.; Rana, V. *Biores. Technol.* **2004**, *95*, 1.
(44) Balat, M.; Balat, H. *Energ. Source. Part A.* **2009**, *31*, 1280.

(45) Kidnay, A. J.; Parrish, W. R.; McCartney, D. G. *Fundamentals of Natural Gas Processing, 2nd Ed.;* CRC Press: Boca Raton, FL, 2009.
(46) Hammer, G.; Lübcke, T.; Kettner, R.; Davis, R. N.; Recknagel, H.; Commichau, A.; Mazyan, W.; Ahmadi, A.; Ahmed, H.; Hoorfar, M. *J. Nat. Gas Sci. Eng.* **2016**, *30*, 487.
(47) Rowsell, J. L. C.; Millward, A. R.; Park, K. S.; Yaghi, O. M. *J. Am. Chem. Soc.* **2004**, *126*, 5666.
(48) Dietzel, P. D. C.; Panella, B.; Hirscher, M.; Blom, R.; Fjellvåg, H. *Chem. Commun*. **2006**, *9*, 959.
(49) Murray, L. J.; Dinča, M.; Long, J. R. *Chem. Soc. Rev.* **2009**, *38,* 1294.
(50) Dietzel, P. D. C.; Georgiev, P. A.; Eckert, J.; Blom, R.; Strässle, T.; Unruh, T. *Chem. Commun*. **2010**, *46*, 4962.
(51) Suh, M. P.; Park, H. J.; Prasad, T. K.; Lim, D.-W. *Chem. Rev.* **2012**, *112*, 782.
(52) Kapelewski, M. T.; Geier, S. J.; Hudson, M. R.; Stück, D.; Mason, J. A.; Nelson, J. N.; Xiao, D. J.; Hulvey, Z.; Gilmour, E.; FitzGerald, S. A.; Head-Gordon, M.; Brown, C. M.; Long, J. R. *J. Am. Chem. Soc.* **2014**, *136*, 12119.
(53) Millward, A. R.; Yaghi, O. M. *J. Am. Chem. Soc.* **2005**, *127*, 17998.
(54) Caskey, S. R.; Wong-Foy, A. G.; Matzger, A. J. *J. Am. Chem. Soc.* **2008**, *130*, 10870.
(55) Bae, Y.-S.; Snurr, R. Q. *Angew. Chem. Int. Ed.* **2011**, *50*, 11586.
(56) Li, J.-R.; Ma, Y.; McCarthy, M. C.; Sculley, J.; Yu, J.; Jeong, H.-K.; Balbuena, P. B.; Zhou, H.-C. *Coord. Chem. Rev.* **2011**, *255*, 1791.
(57) Sumida, K.; Rogow, D. L.; Mason, J. A.; McDonald, T. M.; Bloch, E. D.; Herm, Z. R.; Bae, T.-H.; Long, J. R. *Chem. Rev.* **2012**, *112*, 724.
(58) McDonald, T. M.; Mason, J. A.; Kong, X.; Bloch, E. D.; Gygi, D.; Dani, A.; Crocella, V.; Giordanino, F.; Odoh, S. O.; Drisdell, W.; Vlaisavljevich, B.; Dzubak, A. L.; Poloni, R.; Schnell, S. K.; Planas, N.; Lee, K.; Pascal, T.; Wan, L. F.; Prendergast, D.; Neaton, J. B.; Smit, B.; Kortright, J. B.; Gagliardi, L.; Bordiga, S.; Reimer, J. A.; Long, J. R. *Nature*, **2015**, *519,* 303.
(59) Jorgensen, W. L.; Severance, D. L. *J. Am. Chem. Soc.* **1990**, *112*, 4768.
(60) Hobza, P.; Selzle, H. L.; Schlag, E. W. *J. Am. Chem. Soc.* **1994**, *116*, 3500.
(61) Hobza, P.; Selzle, H. L.; Schlag, E. W. *J. Phys. Chem.* **1996**, *100*, 18790.
(62) Hong, B. H.; Lee, J. Y.; Cho, S. J.; Yun, S.; Kim, K. S. *J. Org. Chem.* **1999**, *64*, 5661.
(63) Tsuzuki, S.; Honda, K.; Uchimaru, T.; Mikami, M.; Tanabe, K. *J. Am. Chem. Soc.* **2001**, *124*, 104.
(64) Sinnokrot, M.O.; Valeev, E.F.; Sherrill, C.D. *J. Am. Chem. Soc.* **2002**, *124*, 10887.
(65) Nishio, M. *Phys. Chem. Chem. Phys.* **2011**, *13*, 13873.
(66) Kinzel, T.; Yong, Z.; Buchwald, S. L *J. Am. Chem. Soc.* **2010**, *132*, 14073.
(67) Lemmon, E. W., Huber, M. L. & McLinden, M. O. *NIST Standard Reference Database 23: Reference Fluid Thermodynamic and Transport Properties—REFPROP Version 8.0* (National Institute of Standards and Technology, 2007).
(68) Sinnokrot, M. O.; Sherrill, C. D. *J. Am. Chem. Soc.* **2004**, *126*, 7690.
(69) Lee, E. C.; Hong, B. H.; Lee, J. Y.; Kim, J. C.; Kim, D.; Kim Y.; Tarakeshwar, P.; Kim, K. W. *J. Am. Chem. Soc.* **2005**, *127*, 4530.
(70) Wheeler, S. E.; Houk, K. N. *Mol. Phys.* **2008**, *107*, 749.

(71) Bloom, J. W. G.; Raju, R. K.; Wheeler, S. E. *J. Chem. Theory Comput.* **2012**, *8*, 3167.
(72) Hwang, J.; Li, P.; Smith, M. D.; Shimizu, K. D. *Angew. Chem. Int. Ed.* **2016**, *55*, 8086.
(73) Dunitz, J. D.; Gavezzotti, A. *Angew. Chem. Int. Ed.* **2005**, *44*, 1766.
(74) Forni, A.; Pieraccini, S.; Rendine, S.; Gabas, F.; Sironi, M. *Chem. Phys. Chem.* **2012**, *13*, 4224.
(75) Allen, F. H. *Acta Crystallogr., Sect. B* **2002**, *58*, 380.
(76) Bruno, I. J.; Cole, J. C.; Edgington, P. R.; Kessler, M.; Macrae, C. F.; McCabe, P.; Pearson, J.; Taylor, R. *Acta Crystallogr., Sect. B* **2002**, *58*, 389.
(77) Hibbs, D. E.; Overgaard, J.; Platts, J. A.; Waller, M. P.; Hursthouse, M. B. *J. Phys. Chem. B* **2004**, *108*, 3663.
(78) Bayón, R.; Coco, S.; Espinet, P. *Chem. Eur. J.* **2005**, *11*, 1079.
(79) Chopra, D.; Nagarajan K.; Guru Row, T. N. *Cryst. Growth Des.* **2005**, *5*, 1035.
(80) Matta, C. F.; Castillo, N.; Boyd, R. J. *J. Phys. Chem. A* **2005**, *109*, 3669.
(81) Chopra, D.; Cameron, T. S.; Ferrara, J. D.; Guru Row, T. N. *J. Phys. Chem. A* **2006**, *110*, 10465.
(82) Choudhury A. R.; Guru Row, T. N. *Cryst. Eng. Comm.* **2006**, *8*, 265.
(83) Mariaca, R.; Behrnd, N.-R.; Eggli, P.; Stoeckli-Evans, H.; Hulliger, J. *Cryst. Eng. Comm.* **2006**, *8*, 222.
(84) Berger, R.; Resnati, G.; Metrangolo, P.; Weber, E.; Hulliger, J. *Chem. Soc. Rev.* **2011**, *40*, 3496.
(85) Baker, R. J.; Colavita, P. E.; Murphy, D. M.; Platts, J. A.; Wallis, J. D. *J. Phys. Chem. A* **2012**, *116*, 1435.
(86) Coudert, F.-X.; Jeffroy, M; Fuchs, A. H.; Boutin, A.; Mellot-Draznieks, C. *J. Am. Chem. Soc.* **2008**, *130*, 14294.
(87) Watanabe, S.; Sugiyama, H.; Adachi, H.; Tanaka, H.; Miyahara, M. *J. Chem. Phys.* **2009**, *130*, 164707.
(88) Neimark, A. V.; Coudert, F.-X.; Boutin, A.; Fuchs, A. H. *J. Phys. Chem. Lett.* **2010**, *1*, 445.
(89) Bousquet, D.; Coudert, F.-X.; Boutin, A. *J. Chem. Phys.* **2012**, *137*, 044118.
(90) Sugiyama, H.; Watanabe, S.; Tanaka, H.; Miyahara, M. T. *Langmuir* **2012**, *28*, 5093.
(91) A description of the accessible N_2 surface area and pore volume calculations is provided in the Supporting Information.
(92) International Energy Agency, *World Energy Outlook 2011: Are We Entering a Golden Age of Gas*, http://www.worldenergyoutlook.org.
(93) U.S. Energy Information Administration, International Energy Statistics, *Today in Energy: Global natural gas consumption doubled from 1980 to 2010,* **2012**, http://www.eia.gov.
(94) Bilgen, S. *Renew. Sust. Energ. Rev.* **2014**, *38*, 890.
(95) Kondo, M.; Yoshitomi, T.; Seki, K.; Matsuzaka H.; Kitagawa, S. *Angew. Chem. Int. Ed.* **1997**, *36*, 1725.
(96) Chui, S. S.-Y.; Lo, S. M.-F.; Charmant, J. P. H.; Orpen, A. G.; Williams, I. D. *Science* **1999**, *283*, 1148.
(97) Noro, S.; Kitagawa, S.; Kondo, M.; Seki, K. *Angew. Chem. Int. Ed.* **2000**, *39*, 2082.

(98) Ma, S.; Sun, D.; Simmons, J. M.; Collier, C. D.; Yuan, D.; Zhou, H.-C. *J. Am. Chem. Soc.* **2008**, *130*, 1012.
(99) Furukawa, H.; Ko, N.; Go, Y. B.; Aratani, N.; Choi, S. B.; Choi, E.; Yazaydin, A. Ö.; Snurr, R. Q.; O'Keeffe, M.; Kim, J.; Yaghi, O. M. *Science* **2010**, *329*, 424.
(100) Wilmer, C. E.; Leaf, M.;Yeon Lee, C.; Farha, O. K.; Hauser, B. G.; Hupp, J. T.; Snurr, R. Q. *Nat. Chem.* **2012**, *4*, 83.
(101) Peng, Y.; Krungleviciute, V.; Eryazici, I.; Hupp, J. T.; Farha, O. K.; Yildirim, T. *J. Am. Chem. Soc.* **2013**, *135*, 11887.
(102) Wilmer, C. E.; Farha, O. K.; Yildirim, T.; Eryazici, I.; Krungleviciute, V.; Sarjeant, A. A.; Snurr, R. Q.; Hupp, J. T. *Energy Environ. Sci.* **2013**, *6*, 1158.
(103) Gándara, F.; Furukawa, H.; Lee, S.; Yaghi, O. M. *J. Am. Chem. Soc.* **2014**, *136*, 5271.
(104) He, Y.; Zhou, W.; Qian, G.; Chen, B. *Chem. Soc. Rev.* **2014**, *43*, 5657.
(105) Li, B.; Wen, H.-M.; Wang, H.; Wu, H.; Tyagi, M.; Yildirim, T.; Zhou, W.; Chen, B. *J. Am. Chem. Soc.* **2014**, *136*, 6207.
(106) Mason, J. A.; Veenstra, M.; Long, J. R. *Chem. Sci.* **2014**, *5*, 32.
(107) Service, R. F. *Science* **2014**, *346*, 538.
(108) Chang, G.; Li, B.; Wang, H.; Bao, Z.; Yildirim, T.; Yao, Z.; Xiang, S.; Zhou, W.; Chen, B. *Chem. Commun.* **2015**, *51*, 14789.
(109) Song, C.; Ling, Y.; Feng, Y.; Zhou, W.; Yildirim, T.; He, Y. *Chem. Commun.* **2015**, *51*, 8508.
(110) Mele, A.; Vergani, B.; Viani, F.; Meille, S. V.; Farina, A.; Bravo, P. *Eur. J. Org. Chem.* **1999**, *1*, 187.
(111) Desiraju, G. R. *Acc. Chem. Res.* **2002**, *35*, 565.
(112) Parsch, J.; Engels, J. W. *J. Am. Chem. Soc.* **2002**, *124*, 5664.
(113) Lee, J. H.; Kim, H. J.; Choi, Y. W.; Lee, Y. M.; Park, B. K.; Kim, C.; Kim, S.-J.; Kim, Y. *Polyhedron* **2007**, *26*, 1388.
(114) O'Hagan, D. *Chem. Soc. Rev.* **2008**, *37*, 308.
(115) Anzahaee, M. Y.; Watts, J. K.; Alla, N. R.; Nicholson, A. W.; Damha, M. J. *J. Am. Chem. Soc.* **2011**, *133*, 728.
(116) Krackl, S.; Inoue, S.; Driess, M.; Enthaler, S. *Eur. J. Inorg. Chem.* **2011**, 2103.
(117) Prakash, G. K. S.; Wang, F.; Rahm, M.; Shen, J.; Ni, C.; Haiges, R.; Olah, G. A. *Angew. Chem. Int. Ed.* **2011**, *50*, 11761.
(118) Liu, C. C.; So, L.-C.; Lo, J. C. Y.; Chan, M. C. W.; Kaneyoshi, H.; Makio, H. *Organometallics*, **2012**, *31*, 5274.
(119) So, L.-C.; Liu, C.-C.; Chan, M. C. W.; Lo, J. C. Y.; Sze, K.-H.; Zhu, N. *Chem. Eur. J.* **2012**, *18*, 565.
(120) Ciavardini, A.; Rondino, F.; Paladini, A.; Speranza, M.; Fornarini, S.; Satta, M.; Piccirillo, S. *Phys. Chem. Chem. Phys.* **2013**, *15*, 19360.
(121) Liu, C.-C.; Chan, M. C. W. *Acc. Chem. Res.* **2015**, *48*, 1580.
(122) Panini, P.; Chopra, D. In *Hydrogen Bonded Supramolecular Structures*; Li, Z. and Wu, L.-Z., Eds.; Springer-Verlag: Berlin, 2015; pp 37-67.
(123) Thalladi, V. R.; Weiss, H.-C.; Bläser, D.; Boese, R.; Nangia, A.; Desiraju, G. R. *J. Am. Chem. Soc.* **1998**, *120*, 8702.
(124) Wheeler, S. E.; McNeil, A. J.; Müller, P.; Swager, T. M.; Houk, K. N. *J. Am. Chem. Soc.* **2010**, *132*, 3304.

(125) Wheeler, S. E. *J. Am. Chem. Soc.* **2011**, *133*, 10262.
(126) Watt, M.; Hardebeck, L. K. E.; Kirkpatrick, C. C.; Lewis, M. *J. Am. Chem. Soc.* **2011**, *133*, 3854

2.7. Supporting Information

Supporting Discussion

NMR spectra were acquired on Bruker AVB-400, AVQ-400, and AV-600 instruments at the University of California, Berkeley, NMR facility. NMR spectra were obtained between 294 and 298.5 K, and all chemical shifts were referenced to residual solvent peaks. Elemental analyses were obtained from the Microanalytical Laboratory of the University of California, Berkeley, using a PerkinElmer 2400 series II combustion analyzer. Infrared spectra were collected on a PerkinElmer Avatar Spectrum 400 FTIR spectrophotometer equipped with a Pike attenuated total reflectance accessory (ATR) accessory. Anhydrous *N,N*-dimethylformamide (DMF) and anhydrous dichloromethane (CH_2Cl_2) were obtained from a JC Meyer solvent system. All other reagents were obtained from commercial vendors and used without further purification. Ultra-high purity (99.999% purity) dinitrogen, helium, and methane were used for all adsorption measurements.

Synthesis of H_2bdp derivatives

H_2(F-bdp) was prepared *via* a Suzuki-Miyaura coupling.[1] Specifically, 1,4-dibromo-2-fluorobenzene (3.03 g, 11.9 mmol, 1.0 equiv), 1-(2-tetrahydropyranyl)-1H-pyrazole-4-boronic acid pinacol ester (8.30 g, 29.8 mmol, 2.5 equiv), and K_3PO_4 (12.7 g, 60 mmol, 5 equiv) were suspended in toluene (24 mL) in a 40-mL glass scintillation vial with a magnetic stir bar and sparged with Ar for 10 minutes. XPhos Pd G2 (1.74 g, 2.4 mmol, 0.2 equiv) was added quickly in air, and vial was briefly purged with Ar, sealed with a PTFE-lined cap, and heated to 110 °C while stirring for 2 days. Upon completion, the reaction mixture was cooled to room temperature, concentrated under reduced pressure, and diluted with 250 mL of diethyl ether. The ether layer was washed 5 times with 250 mL of saturated aqueous $NaHCO_3$ solution, dried over $MgSO_4$, and concentrated under reduced pressure to yield a yellow oil, which was used in the subsequent reaction without additional purification. The crude ligand was dissolved in 90 mL of methanol in a 250-mL round-bottom flask with a magnetic stir bar, 18 mL of concentrated aqueous HCl was added, and the reaction mixture was stirred at 50 °C for 2 h, during which time a yellow precipitate formed. The reaction mixture was filtered, and the filtrate was suspended in water and neutralized with $NaHCO_3$. The precipitate was again isolated by filtration, washed with water, and dried *in vacuo* to yield **H_2(F-bdp)** (1.31 g, 5.8 mmol, 49%) as a beige powder. ^{1}H NMR (400 MHz, DMSO-d_6): δ 8.13 (s, 2H), 8.05 (s, 2H) 7.70 (t, J = 8.2 Hz, 1H), 7.52 (dd, J = 12.8, 1.8 Hz, 1H), 7.46 (dd, J = 8.1, 1.8 Hz, 1H) ppm; ^{13}C NMR (101 MHz, DMSO-d_6): δ 160.65, 158.22, 133.04 (d, J = 9.3 Hz), 128.58 (d, J = 5.0 Hz), 121.77, 120.55, 115.15, 112.79, 112.56 ppm; ^{19}F NMR (376 MHz, DMSO-d_6): δ -114.70 ppm. Note that the ^{1}H NMR signals from the hydrogen atoms bonded to the pyrazole nitrogen atoms are too broad to be visible. Anal. Calcd. for $C_{12}H_9FN_4$: C, 63.15,

H, 3.97, N, 24.55; found: C, 61.85, H, 3.99, N, 23.64. IR: 3137(w), 3079 (w), 2935 (m), 2848 (m), 1624 (w), 1587 (m), 1473 (m), 1452 (m), 1374 (m), 1271 (w), 1252 (w), 1230 (w), 1200 (w), 1157 (m), 1111(m), 1038(m), 984 (w), 961 (m), 950 (m), 876 (m), 857 (s), 814 (s), 750 (m), 724 (m), 669 (w), 661 (w), 594 (s), 556 (m), 533 (m), 520 (m), 508 (m), 498 (w), 483 (m), 471 (m), 459 (s), 452 (m) cm^{-1}.

H_2(*p*-F_2-bdp) was prepared *via* a Suzuki-Miyaura coupling.[1] Specifically, 1,4-dibromo-2,5-difluorobenzene (2.18 g, 8.0 mmol, 1.0 equiv), 1-(2-tetrahydropyranyl)-1H-pyrazole-4-boronic acid pinacol ester (5.56 g, 20.0 mmol, 2.5 equiv), and K_3PO_4 (8.48 g, 40 mmol, 5 equiv) were suspended in toluene (16 mL) in a 40-mL glass scintillation vial with a magnetic stir bar and sparged with Ar for 10 minutes. XPhos Pd G2 (1.26 g, 1.6 mmol, 0.2 equiv) was added quickly in air, and vial was briefly purged with Ar, sealed with a PTFE-lined cap, and heated to 110 °C while stirring for 2 days. Upon completion, the reaction mixture was cooled to room temperature, concentrated under reduced pressure, and diluted with 250 mL of diethyl ether. The ether layer was washed 5 times with 250 mL of saturated aqueous $NaHCO_3$ solution, dried over $MgSO_4$, and concentrated under reduced pressure to yield a yellow oil, which was used in the subsequent reaction without additional purification. The crude ligand was dissolved in 60 mL of methanol in a 250-mL round-bottom flask with a magnetic stir bar, 12 mL of concentrated aqueous HCl was added, and the reaction mixture was stirred at 50 °C for 2 h, during which time a white precipitate formed. The reaction mixture was filtered, and the filtrate was suspended in water and neutralized with $NaHCO_3$. The precipitate was again isolated by filtration, washed with water, and dried *in vacuo* to yield **H_2(*p*-F_2-bdp)** (0.86 g, 3.5 mmol, 44%) as a beige powder. ^{1}H NMR (400 MHz, DMSO-d_6): δ 8.11 (s, 4H), 7.68 (t, J = 9.3 Hz, 2H) ppm; ^{13}C NMR (101 MHz, DMSO-d_6): δ 156.06, 153.68, 132.40, 119.33 – 119.81 (m), 118.58 – 118.14 (m), 114.60 – 113.78 (m) ppm; ^{19}F NMR (400 MHz, DMSO-d_6): δ -119.78 (t, J = 9.3 Hz) ppm. Note that the ^{1}H NMR signals from the hydrogen atoms bonded to the pyrazole nitrogen atoms are too broad to be visible. Anal. Calcd. for $C_{12}H_8F_2N_4$: C, 58.54, H, 3.27, N, 22.75; found: C, 57.72, H, 3.35, N, 21.82. IR: 3139 (m), 3076 (w), 2966 (m), 2938 (m), 2850 (m), 1589 (m), 1539 (w), 1490 (m), 1435 (w), 1374 (m), 1350 (w), 1273 (m), 1241 (w), 1155 (s), 1041 (m), 963 (s), 867 (s), 818 (m), 780 (s), 698 (m), 668 (w), 605 (s), 549 (w), 531 (w), 512 (w), 482 (w), 472 (w), 460 (m) cm^{-1}.

H_2(*o*-F_2-bdp) was prepared *via* a Suzuki-Miyaura coupling.[1] Specifically, 1,4-dibromo-2,3-difluorobenzene (2.18 g, 8.0 mmol, 1.0 equiv), 1-(2-tetrahydropyranyl)-1H-pyrazole-4-boronic acid pinacol ester (5.56 g, 20.0 mmol, 2.5 equiv), and K_3PO_4 (8.48 g, 40 mmol, 5 equiv) were suspended in toluene (16 mL) in a 40-mL glass scintillation vial with a magnetic stir bar and sparged with Ar for 10 minutes. XPhos Pd G2 (1.26 g, 1.6 mmol, 0.2 equiv) was added quickly in air, and vial was briefly purged with Ar, sealed with a PTFE-lined cap, and heated to 110 °C while stirring for 2 days. Upon completion, the reaction mixture was cooled to room temperature, concentrated under reduced pressure, and diluted with 250 mL of diethyl ether. The ether layer was washed 5 times with 250 mL of saturated aqueous $NaHCO_3$ solution, dried over $MgSO_4$, and concentrated under reduced pressure to yield a yellow oil, which was used in the subsequent reaction without additional purification. The crude ligand was dissolved in 60 mL of methanol in a 250-mL round-bottom flask with a magnetic stir bar, 12 mL of concentrated aqueous HCl was

added, and the reaction mixture was stirred at 50 °C for 2 h, during which time a white precipitate formed. The reaction mixture was filtered, and the filtrate was suspended in water and neutralized with $NaHCO_3$. The precipitate was again isolated by filtration, washed with water, and dried *in vacuo* to yield **H_2(*o*-F_2-bdp)** (0.85 g, 3.5 mmol, 43%) as a beige powder. ^{1}H NMR (400 MHz, DMSO-d_6): δ 13.17 (s, 2H), 8.21 (s, 2H), 7.96 (s, 2H), 7.54 – 7.50 (m, 2H) ppm; ^{13}C NMR (101 MHz, DMSO-d_6): δ 148.74 (d, J = 15.4 Hz), 146.28 (d, J = 15.2 Hz), 122.96 – 122.77 (m), 120.15 – 199.99 (m), 114.27 ppm; ^{19}F NMR (376 MHz, DMSO-d_6): δ -140.93 ppm. Anal. Calcd. for $C_{12}H_8F_2N_4$: C, 58.54, H, 3.27, N, 22.75; found: C, 57.91, H, 3.27, N, 21.81. IR: 3130 (w), 3072 (w), 3000 (w), 2944 (m), 2841 (m), 1589 (w), 1529 (w), 1465 (m), 1378 (m), 1339 (w), 1290 (w), 1253 (w), 1215 (w), 1159 (m), 1047 (m), 1013 (w), 985 (m), 960 (m), 888 (m), 867 (s), 851 (s), 801 (s), 667 (m), 646 (w), 626 (s), 612 (w), 588 (s), 548 (w), 542 (w), 511 (w), 489 (w), 473 (w), 463 (w) cm^{-1}.

H_2(D_4-bdp) was prepared *via* a Suzuki-Miyaura coupling.[1] Specifically, 1,4-dibromobenzene-d_4 (2.0 g, 8.4 mmol, 1.0 equiv), 1-(2-tetrahydropyranyl)-1H-pyrazole-4-boronic acid pinacol ester (5.84 g, 21.0 mmol, 2.5 equiv), and K_3PO_4 (8.87 g, 41.9 mmol, 5 equiv) were suspended in toluene (16 mL) in a 40-mL glass scintillation vial with a magnetic stir bar and sparged with Ar for 10 minutes. XPhos Pd G2 (0.63 g, 0.8 mmol, 0.2 equiv) was added quickly in air, and vial was briefly purged with Ar, sealed with a PTFE-lined cap, and heated to 110 °C while stirring for 2 days. Upon completion, the reaction mixture was cooled to room temperature, concentrated under reduced pressure, and diluted with 250 mL of diethyl ether. The ether layer was washed 5 times with 250 mL of saturated aqueous $NaHCO_3$ solution, dried over $MgSO_4$, and concentrated under reduced pressure to yield a yellow oil, which was used in the subsequent reaction without additional purification. The crude ligand was dissolved in 60 mL of methanol in a 250-mL round-bottom flask with a magnetic stir bar, 12 mL of concentrated aqueous HCl was added, and the reaction mixture was stirred at 50 °C for 2 h, during which time a white precipitate formed. The reaction mixture was filtered, and the filtrate was suspended in water and neutralized with $NaHCO_3$. The precipitate was again isolated by filtration, washed with water, and dried *in vacuo* to yield **H_2(D_4-bdp)** (1.03 g, 4.8 mmol, 58%) as a beige powder. Due to the partial deuteration of the molecule, ^{13}C NMR and C/H/N elemental analysis were substituted with ^{2}H NMR and high-resolution mass spectrometry, respectively. ^{1}H NMR (400 MHz, DMSO-d_6): δ 8.06 (s, 4H) ppm; ^{2}H NMR (92 MHz, DMSO-d_6): δ 7.68 ppm. Note that the ^{1}H NMR signals from the hydrogen atoms bonded to the pyrazole nitrogen atoms are too broad to be visible. HRMS (EI+) for $C_{12}H_6D_4N_4$: 214.1157; found: 214.1157. IR: 3160 (w), 3110 (w), 3058 (w), 2979 (w), 1581 (w), 1527 (w), 1437 (w), 1396 (w), 1364 (w), 1318 (w), 1294 (w), 1150 (m), 1097 (w), 1028 (m), 964 (m), 945 (s), 870 (m), 815 (m), 740 (s), 691 (s), 616 (m), 600 (m), 534 (s), 516 (m), 510 (m), 500 (m), 489 (m), 455 (s) cm^{-1}.

H_2(*p*-Me_2-bdp) was prepared *via* a Suzuki-Miyaura coupling.[1] Specifically, 1,4-dibromo-2,5-dimethylbenzene (2.10 g, 8.0 mmol, 1.0 equiv), 1-(2-tetrahydropyranyl)-1H-pyrazole-4-boronic acid pinacol ester (5.56 g, 20.0 mmol, 2.5 equiv), and K_3PO_4 (8.48 g, 40 mmol, 5 equiv) were suspended in toluene (16 mL) in a 40-mL glass scintillation vial with a magnetic stir bar and sparged with Ar for 10 minutes. XPhos Pd G2 (0.63 g, 0.8

mmol, 0.1 equiv) was added quickly in air, and vial was briefly purged with Ar, sealed with a PTFE-lined cap, and heated to 110 °C while stirring for 2 days. Upon completion, the reaction mixture was cooled to room temperature, concentrated under reduced pressure, and diluted with 250 mL of diethyl ether. The ether layer was washed 5 times with 250 mL of saturated aqueous $NaHCO_3$ solution, dried over $MgSO_4$, and concentrated under reduced pressure to yield a yellow oil, which was used in the subsequent reaction without additional purification. The crude ligand was dissolved in 60 mL of methanol in a 250-mL round-bottom flask with a magnetic stir bar, 12 mL of concentrated aqueous HCl was added, and the reaction mixture was stirred at 50 °C for 2 h, during which time a white precipitate formed. The reaction mixture was filtered, and the filtrate was suspended in water and neutralized with $NaHCO_3$. The precipitate was again isolated by filtration, washed with water, and dried *in vacuo* to yield **H_2(*p*-Me_2-bdp)** (1.01 g, 4.2 mmol, 53%) as a white powder. ^{1}H NMR (400 MHz, DMSO-d_6): δ 12.95 (s, 2H), 7.95 (s, 2H), 7.73 (s, 2H), 7.28 (s, 2H), 2.35 (s, 6H); ^{13}C NMR (101 MHz, DMSO-d_6): δ 132.24, 131.22, 130.65, 120.51, 21.19. ppm. Anal. Calcd. for $C_{14}H_{14}N_4$: C, 70.57, H, 5.92, N, 23.51; found: C, 70.60, H, 5.97, N, 23.44. IR: 3124 (m), 2949 (m), 1527 (m), 1445 (w), 1368 (m), 1342 (m), 1247 (w), 1167 (m), 1047 (m), 1032 (w), 951 (s), 893 (m), 862 (s), 816 (s), 682 (s), 622 (w), 604 (m), 570 (w), 559 (w), 552 (w), 516 (w), 485 (w), 458 (m) cm^{-1}.

Synthesis of Co(bdp) derivatives

Co(bdp) was resynthesized in order to obtain an improved X-ray diffraction structure of the solvated material. Single crystals were obtained following the literature procedure.[2] By collecting data at 298 K, non-uniform structural changes induced by slow- or flash-cooling the crystal to 100 K were avoided, and an improved single crystal structure was obtained. Additional details on single crystal data collection are given below.

Co(F-bdp) was prepared using a strategy adapted from a previous report.[2] Specifically, a 100-mL solvent bomb was charged with a magnetic stirring bar, $Co(CF_3SO_3)_2$ (0.75 g, 2.1 mmol, 1.0 equiv), H_2(F-bdp) (0.48 g, 2.1 mmol, 1.0 equiv), and DMF (10.4 mL). The reaction mixture was degassed by the freeze–pump–thaw method for 5 cycles, then sealed by closing the stopcock of the solvent bomb while the frozen reaction mixture remained under vacuum. The solvent bomb was then heated at 160 °C for 3 days to afford a purple microcrystalline solid. (To obtain crystals suitable for single-crystal X-ray diffraction, the magnetic stir bar was omitted from reaction flask while maintaining all other conditions constant.) Upon completion, the solvent bomb was backfilled with Ar, the supernatant was removed under positive Ar pressure and discarded, and 80 mL of anhydrous DMF was added to the solid product while maintaining under inert atmosphere. The solvent bomb was then sealed under Ar and heated to 110 °C overnight. This solvent-exchange procedure was performed once daily for 7 days to completely remove unreacted starting material from the pores. Subsequently, the DMF was replaced with anhydrous CH_2Cl_2 following the same procedure but without heating; these CH_2Cl_2 exchanges were performed once daily for 3 days to allow activation from a lower-boiling solvent. To activate the material, the CH_2Cl_2 was removed under positive Ar pressure until 25 mL of solution remained. The resultant slurry was transferred to a 100-mL

Schlenk flask under inert atmosphere, and the CH_2Cl_2 was evaporated by flowing Ar at room temperature for 1 h. The resultant solid was dried by flowing Ar at 160 °C for 6 h, then placed under dynamic vacuum at 160 °C overnight to yield **Co(F-bdp)** (0.153 g, 0.5 mmol, 25%). The activated solid was immediately transferred to a glovebox and handled under a dinitrogen atmosphere for all further experiments. Anal. Calcd. for $C_{12}H_9CoFN_4$: C, 50.19, H, 3.16, N, 19.51; found: C, 47.39, H, 2.29, N, 18.29. IR: 1575 (m), 1490 (w), 1442 (w), 1374 (m), 1356 (m), 1331 (m), 1254 (m), 1236 (m), 1198 (w), 1170 (s), 1108 (m), 1079 (w), 1050 (s), 998 (m), 989 (m), 953 (s), 854 (s), 816 (s), 720 (w), 660 (m), 652 (m), 606 (s), 559 (s), 481 (s), 467 (s) cm^{-1}.

Co(*p*-F_2-bdp) was prepared using a strategy adapted from a previous report.[2] Specifically, a 50-mL solvent bomb was charged with a magnetic stirring bar, $Co(CF_3SO_3)_2$ (0.95 g, 2.7 mmol, 1.2 equiv), H_2(*p*-F_2-bdp) (0.55 g, 2.2 mmol,1.0 equiv), and DMF (11.0 mL). The reaction mixture was degassed by the freeze–pump–thaw method for 5 cycles, then sealed by closing the stopcock of the solvent bomb while the frozen reaction mixture remained under vacuum. The solvent bomb was then heated at 160 °C for 3 days to afford a purple microcrystalline solid. (To obtain crystals suitable for single-crystal X-ray diffraction, the magnetic stir bar was omitted from reaction flask while maintaining all other conditions constant.) Upon completion, the solvent bomb was backfilled with Ar, the supernatant was removed under positive Ar pressure and discarded, and 40 mL of anhydrous DMF was added to the solid product while maintaining under inert atmosphere. The solvent bomb was then sealed under Ar and heated to 110 °C overnight. This solvent-exchange procedure was performed once daily for 7 days to completely remove unreacted starting material from the pores. Subsequently, the DMF was replaced with anhydrous CH_2Cl_2 following the same procedure but without heating; these CH_2Cl_2 exchanges were performed once daily for 3 days to allow activation from a lower-boiling solvent. To activate the material, the CH_2Cl_2 was removed under positive Ar pressure until 25 mL of solution remained. The resultant slurry was transferred to a 100-mL Schlenk flask under inert atmosphere, and the CH_2Cl_2 was evaporated by flowing Ar at room temperature for 1 h. The resultant solid was dried by flowing Ar at 160 °C for 6 h, then placed under dynamic vacuum at 160 °C overnight to yield **Co(*p*-F_2-bdp)** (0.303 g, 1.0 mmol, 44%). The activated solid was immediately transferred to a glovebox and handled under a dinitrogen atmosphere for all further experiments. Anal. Calcd. for $C_{12}H_8CoF_2N_4$: C, 47.73, H, 2.63, N, 18.36; found: C, 46.98, H, 2.21, N, 18.14. IR: 2926 (m), 2858 (w), 1737 (m), 1581 (w), 1493 (w), 1467 (w), 1444 (w), 1367 (m), 1272 (s), 1162 (s), 1119 (s), 1057 (s), 967 (s), 880 (m), 851 (m), 777 (s), 696 (m), 617 (m), 553 (m), 530 (m), 472 (m), 452 (m) cm^{-1}.

Co(*o*-F_2-bdp) was prepared using a strategy adapted from a previous report.[2] Specifically, a 100-mL solvent bomb was charged with a magnetic stirring bar, $Co(CF_3SO_3)_2$ (0.72 g, 2.0 mmol, 1.05 equiv), H_2(*o*-F_2-bdp) (0.473 g, 1.9 mmol, 1.0 equiv), and DMF (10.0 mL). The reaction mixture was degassed by the freeze–pump–thaw method for 5 cycles, then sealed by closing the stopcock of the solvent bomb while the frozen reaction mixture remained under vacuum. The solvent bomb was then heated at 160 °C for 3 days to afford a purple microcrystalline solid. (To obtain crystals suitable for single-crystal X-ray diffraction, the magnetic stir bar was omitted from reaction flask

while maintaining all other conditions constant.) Upon completion, the solvent bomb was backfilled with Ar, the supernatant was removed under positive Ar pressure and discarded, and 80 mL of anhydrous DMF was added to the solid product while maintaining under inert atmoshere. The solvent bomb was then sealed under Ar and heated to 110 °C overnight. This solvent-exchange procedure was performed once daily for 7 days to completely remove unreacted starting material from the pores. Subsequently, the DMF was replaced with anhydrous CH_2Cl_2 following the same procedure but without heating; these CH_2Cl_2 exchanges were performed once daily for 3 days to allow activation from a lower-boiling solvent. To activate the material, the CH_2Cl_2 was removed under positive Ar pressure until 25 mL of solution remained. The resultant slurry was transferred to a 100-mL Schlenk flask under inert atmosphere, and the CH_2Cl_2 was evaporated by flowing Ar at room temperature for 1 h. The resultant solid was dried by flowing Ar at 160 °C for 6 h, then placed under dynamic vacuum at 160 °C overnight to yield **Co(*o*-F_2-bdp)** (0.182 g, 0.6 mmol, 31%). The activated solid was immediately transferred to a glovebox and handled under a dinitrogen atmosphere for all further experiments. Anal. Calcd. for $C_{12}H_8CoF_2N_4$: C, 47.73, H, 2.63, N, 18.36; found: C, 47.23, H, 2.18, N, 18.36. IR: 1582 (m), 1559 (w), 1466 (m), 1384 (m), 1345 (m), 1290 (w), 1253 (m), 1214 (w), 1175 (m), 1052 (s), 1024 (m), 998 (m), 868 (s), 852 (s), 807 (s), 657 (w), 643 (m), 624 (w), 591 (s), 544 (m), 455 (s) cm^{-1}.

Co(D_4-bdp) was prepared using a strategy adapted from a previous report.[2] Specifically, a 100-mL solvent bomb was charged with a magnetic stirring bar, $Co(CF_3SO_3)_2$ (1.62 g, 4.5 mmol, 1.2 equiv), H_2(D_4-bdp) (0.80 g, 3.7 mmol, 1.0 equiv), and DMF (19.0 mL). The reaction mixture was degassed by the freeze–pump–thaw method for 5 cycles, then sealed by closing the stopcock of the solvent bomb while the frozen reaction mixture remained under vacuum. The solvent bomb was then heated at 160 °C for 3 days to afford a purple microcrystalline solid. (To obtain crystals suitable for single-crystal X-ray diffraction, the magnetic stir bar was omitted from reaction flask while maintaining all other conditions constant.) Upon completion, the solvent bomb was backfilled with Ar, the supernatant was removed under positive Ar pressure and discarded, and 80 mL of anhydrous DMF was added to the solid product while maintaining under inert atmoshere. The solvent bomb was then sealed under Ar and heated to 110 °C overnight. This solvent-exchange procedure was performed once daily for 7 days to completely remove unreacted starting material from the pores. Subsequently, the DMF was replaced with anhydrous CH_2Cl_2 following the same procedure but without heating; these CH_2Cl_2 exchanges were performed once daily for 3 days to allow activation from a lower-boiling solvent. To activate the material, the CH_2Cl_2 was removed under positive Ar pressure until 25 mL of solution remained. The resultant slurry was transferred to a 100-mL Schlenk flask under inert atmosphere, and the CH_2Cl_2 was evaporated by flowing Ar at room temperature for 1 h. The resultant solid was dried by flowing Ar at 160 °C for 6 h, then placed under dynamic vacuum at 160 °C overnight to yield **Co(D_4-bdp)** (0.362 g, 1.3 mmol, 35%). The activated solid was immediately transferred to a glovebox and handled under a dinitrogen atmosphere for all further experiments. Anal. Calcd. for $C_{12}H_6CoD_4N_4$: C, 52.76, H, 2.21, N, 20.51; found: C, 50.55, H, 2.73, N, 19.55. IR: 1564 (w), 1396 (w), 1366 (m), 1313 (w), 1282 (m), 1219 (w), 1158 (m), 1072 (m), 1038 (s),

995 (m), 946 (s), 858 (s), 825 (m), 738 (s), 635 (s), 606 (w), 493 (s), 483 (s), 460 (s) cm^{-1}.

Co(*p*-Me$_2$-bdp) was prepared using a strategy adapted from a previous report.[2] Specifically, a 250-mL solvent bomb was charged with a magnetic stirring bar, $Co(CF_3SO_3)_2$ (3.50 g, 9.7 mmol, 1.8 equiv), H_2(*p*-Me$_2$-bdp) (1.25 g, 5.3 mmol, 1.0 equiv), and DMF (70.0 mL). The reaction mixture was degassed by the freeze–pump–thaw method for 5 cycles, then sealed by closing the stopcock of the solvent bomb while the frozen reaction mixture remained under vacuum. The solvent bomb was then heated at 160 °C for 36 h to afford a purple microcrystalline solid. (To obtain crystals suitable for single-crystal X-ray diffraction, the magnetic stir bar was omitted from reaction flask while maintaining all other conditions constant.) Upon completion, the solvent bomb was backfilled with Ar, the supernatant was removed under positive Ar pressure and discarded, and 80 mL of anhydrous DMF was added to the solid product while maintaining under inert atmoshere. The solvent bomb was then sealed under Ar and heated to 110 °C overnight. This solvent-exchange procedure was performed once daily for 7 days to completely remove unreacted starting material from the pores. Subsequently, the DMF was replaced with anhydrous CH_2Cl_2 following the same procedure but without heating; these CH_2Cl_2 exchanges were performed once daily for 3 days to allow activation from a lower-boiling solvent. To activate the material, the CH_2Cl_2 was removed under positive Ar pressure until 25 mL of solution remained. The resultant slurry was transferred to a 100-mL Schlenk flask under inert atmosphere, and the CH_2Cl_2 was evaporated by flowing Ar at room temperature for 1 h. The resultant solid was dried by flowing Ar at 160 °C for 6 h, then placed under dynamic vacuum at 160 °C overnight to yield **Co(p-Me$_2$-bdp)** (0.174 g, 0.6 mmol, 11%). The activated solid was immediately transferred to a glovebox and handled under a dinitrogen atmosphere for all further experiments. Anal. Calcd. for $C_{14}H_{14}CoN_4$: C, 56.76, H, 4.75, N, 18.85; found: C, 56.77, H, 3.96, N, 19.10. IR: 1694 (w), 1572 (m), 1458 (w), 1441 (w), 1407 (w), 1370 (s), 1356 (w), 1306 (m), 1239 (w), 1160 (s), 1118 (s), 1051 (s), 1005 (m), 955 (s), 892 (m), 853 (s), 771 (w), 671 (s), 623 (m), 521 (w), 504 (s), 463 (m), 453 (m) cm^{-1}.

Single Crystal X-ray Diffraction

Data for Co(F-bdp) were collected at 100 K. For single crystals of Co(bdp), Co(D_4-bdp), Co(*o*-F_2-bdp), and Co(*p*-F_2-bdp), both rapid and slow cooling to 100 K led to severe deterioration of crystal quality. It is highly likely that cooling crystals of these frameworks induces non-uniform structural changes arising from the framework flexibility. Therefore, data for these crystals were collected at 298 K, where crystal quality was preserved.

All crystals were refined as inversion twins in chiral space groups based on Flack parameter values near 0.5. Additional merohedral twinning was observed for Co(*p*-F_2-bdp), which was refined using the twin law, 0 1 0 1 0 0 0 0 –1. Raw data were corrected for Lorenz and polarization effects using Bruker AXS SAINT software[3] and were corrected for absorption using SADABS.[4] The structures were solved using SHELXT[5] and refined using SHELXL[6] operated in the OLEX2[7] interface. Thermal parameters were

refined anisotropically for all non-hydrogen atoms. All hydrogen atoms were placed geometrically and refined using a riding model.

Single crystals of Co(bdp) and all single crystal derivatives characterized here maintain an open structure containing *N,N*-diethylformamide solvent molecules in the as-synthesized form. However, these solvent molecules were found to be highly disordered, particularly for data sets collected at 298 K. Therefore, the unassigned electron density was accounted for using the PLATON routine SQUEEZE. For Co(*o*-F_2-bdp) and Co(*p*-F_2-bdp), displacement parameter restraints (RIGU and SIMU) were necessary to model the disorder of the organic linkers. Distance restraints (SADI) were additionally necessary to model disorder in the Co(*o*-F_2-bdp) structure. Selected structural information is given in Table 2.S1.

Powder X-ray Diffraction

The analysis of the diffraction data (pattern indexing, profile fitting, crystal structure solution and refinement) was performed with the program TOPAS 4.1.[8] The pattern indexing was done with the singular value decomposition method.[9] The pattern indexing provided a short list of space groups and the correct one was later confirmed by the structure solutions and Rietveld refinements. Precise lattice parameters were determined by Pawley fits.[10] The unknown crystal structures were solved by the global optimization method of simulated annealing (SA) in real space.[11] For the structure solution, rigid bodies were used (the connectivity between the atoms within the rigid bodies was defined with a *z* matrix notation). During the SA runs, three rotations, three translations, and all possible torsion angles were set as flexible for each rigid body. In addition, the positions of the Co atoms were freely varied (using an "occupancy-merge" command as a caution for special positions). An overall temperature factor for each atom type was included in the SA process. Once a global minimum was found, the crystal structures were subjected to Rietveld refinement,[12] in which bond lengths and angles were refined within the rigid bodies, together with free refinement of all profile and lattice parameters. All refinements converged quickly. The final Rietveld plots are presented in Figures 2.S5-2.S8, and selected structural information is given in Table 2.S2. Hydrogen atoms were added at calculated positions by the program Mercury.[13]

Gas Adsorption

Langmuir surface area measurements:

Langmuir surface areas were determined by measuring N_2 adsorption isotherms in a 77 K liquid N_2 bath using a Micromeritics ASAP 2020 or 2420 instrument. Because all of the reported metal-organic frameworks are flexible and undergo N_2-induced phase changes throughout the N_2 adsorption isotherms, Langmuir surface areas were calculated using the N_2 uptake at 0.9 bar to approximate the saturation capacity. This value (in mmol N_2/g) was converted to m^2/g assuming a value of 16.2 $Å^2$ for the molecular cross-sectional area of N_2 (see Table 2.S1). Note that BET surface areas cannot be accurately determined for either framework because of the steps in the low-pressure 77 K N_2 adsorption isotherms.

Accessible N_2 Surface Area and Pore Volume Calculations:
The accessible N_2 surface areas of collapsed Co(*p*-Me_2-bdp), Co(*p*-F_2-bdp), Co(D_4-bdp), and CH_4-expanded Co(*p*-F_2-bdp), were calculated from the crystal structures of the activated materials using an N_2-sized probe molecule, a technique that has been shown to be consistent with experimentally measured surface areas for a wide range of metal-organic frameworks.[14] The calculated accessible surface areas were then converted to a total pore volume using the cross-sectional area of N_2 (16.2 $Å^2$) and the density of liquid N_2 (0.808 g/mL), yielding pore volumes analogous to those that would be calculated from experimentally measured 77 K N_2 adsorption isotherms.

Pre-Step CH_4 Adsorption in Co(F-bdp):
In contrast to Co(D_4-bdp), Co(*p*-F_2-bdp) and Co(*o*-F_2-bdp), the CH_4 adsorption isotherm for Co(F-bdp) shows some degree of adsorption before the step. To understand this, *in situ* powder X-ray diffraction data was collected on an activated sample of Co(F-bdp) under dynamic vacuum, but the sample showed a mixture of collapsed and expanded phases. Repeated syntheses failed to produce a completely collapsed material at 0 bar, so crystal structures could not be obtained. We hypothesize that the pre-step CH_4 adsorption in Co(F-bdp) is the result of some particles failing to collapse under vacuum, which could be caused by the presence of impurities or unreacted ligand within the pores.

Cyclability of Co(bdp) Derivatives:
Extended cycling studies were not performed on the Co(bdp) derivatives; however, in addition to an initial high-pressure 25 °C CH_4 isotherm, a second isotherm at 38 °C was immediately performed on each derivative without removing it from the instrument for reactivation (see Figures 2.S17, 2.S18, 2.S19, 2.S21, and 2.S22). The 38 °C isotherms reproduced the isotherm shape of the corresponding material's 25 °C isotherm, indicating that the material had fully collapsed upon evacuation and was capable of subsequent re-expansion, thereby providing rudimentary evidence of cyclability.

Supporting Tables

Table 2.S1. Selected structrucal information for the DEF-solvated compounds studied via single crystal X-ray diffraction.

	Co(bdp)	**Co(D_4-bdp)**	**Co(F-bdp)**	**Co(*o*-F_2-bdp)**	**Co(*p*-F_2-bdp)**
Formula	$CoC_{12}H_8N_4$	$CoC_{12}H_4D_4N_4$	$CoC_{12}H_7FN_4$	$CoC_{12}H_6F_2N_4$	$CoC_{12}H_6F_2N_4$
Temperature (K)	298(2)	298(2)	100(2)	298(2)	298(2)
Crystal System	Tetragonal	Tetragonal	Tetragonal	Tetragonal	Tetragonal
Space Group	$P4_122$	$P4_322$	$P4_322$	$P4_322$	$P4_3$
a, b, c (Å)	13.2708(4), 13.2708(4), 14.3502(5)	13.2909(5), 13.2909(5), 14.3560(6)	13.3100(5), 13.3100(5), 13.9569(6)	13.2891(5), 13.2891(5), 43.2262(19)	13.2715(5), 13.2715(5), 14.6258(6)
α, β, γ (°)	90	90	90	90	90
V, (Å^3)	2527.27(18)	2536.0(2)	2472.6(2)	7633.8(7)	2576.1(2)
Z	4	4	4	12	4
Radiation, λ (Å)	Synchrotron, 0.7749	Synchrotron, 0.7749	Synchrotron, 0.7749	Synchrotron, 0.8856	Synchrotron, 0.8856
Data / Restraints / Parameters	2322 / 0 / 81	3051 / 0 / 81	2271 / 0 / 99	6994 / 210 / 289	5895 / 103 / 175
Goodness of Fit on F^2	1.128	1.149	1.116	1.066	1.072
R1[a], wR2[b] (I>2σ(I))	0.0279, 0.0810	0.0270, 0.0850	0.0297, 0.0816	0.0492, 0.1311	0.0354, 0.0909
R1[a], wR2[b] (all data)	0.0329, 0.0836	0.0300, 0.0868	0.0363, 0.0844	0.0601, 0.1409	0.0393, 0.0929
Largest Diff. Peak and Hole (e Å^{-3})	0.190 and –0.294	0.227 and –0.243	0.300 and –0.365	0.836 and –1.552	0.259 and –0.241

[a] $R_1 = \sum||F_o| - |F_c||/\sum|F_o|$. [b] $wR_2 = \{\sum[w(F_o^2 - F_c^2)^2]/\sum[w(F_o^2)^2]\}^{1/2}$

Table 2.S2. Selected structural information for the compounds studied via *in situ* powder X-ray diffraction.

	Co(D_4-bdp)	**Co(*p*-Me_2-bdp)**	**Co(*p*-F_2-bdp)**	**Co(*p*-F_2-bdp)**
Pressure / bar	0	0	0	19.7
Space group	*C*2/*c*	*C*2/*c*	$P2_1/c$	*C*2/*c*
a / Å	24.687(9)	24.640(3)	7.028(2)	20.912(9)
b / Å	6.667(1)	8.6962(9)	24.520(7)	16.530(5)
c / Å	7.091(3)	7.129(7)	7.320(7)	6.949(1)
α / °	90	90	90	90
β / °	92.40(4)	90.08(1)	111.9(1)	98.1(1)
γ / °	90	90	90	90
V / $Å^3$	1166.2(6)	1527.7(3)	1170.0(5)	2378(1)
Density / g/cm^3	1.5330(8)	1.3357(3)	1.7208(8)	0.8298(5)

Table 2.S3. Langmuir surface areas of Co(bdp) derivatives.

Material	Langmuir Surface Area
Co(F-bdp)	2529 m^2/g
Co(*p*-F_2-bdp)	2279 m^2/g
Co(*o*-F_2-bdp)	2668 m^2/g
Co(D_4-bdp)	2702 m^2/g
Co(*p*-Me_2-bdp)	1741 m^2/g

Supporting Figures

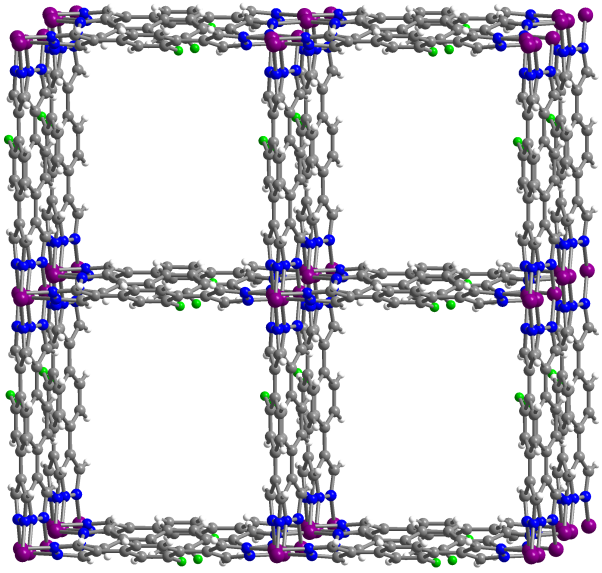

Figure 2.S1. Single-crystal X-ray diffraction structure of DEF-solvated Co(F-bdp). Gray, blue, white, purple, and green spheres represent C, N, H, Co, and F atoms, respectively. Note that although the fluorine atoms were found to be statistically disordered over the four benzene ring positions, only one position is shown for clarity. DEF molecules in the framework pores were found to be disordered and could not be modeled.

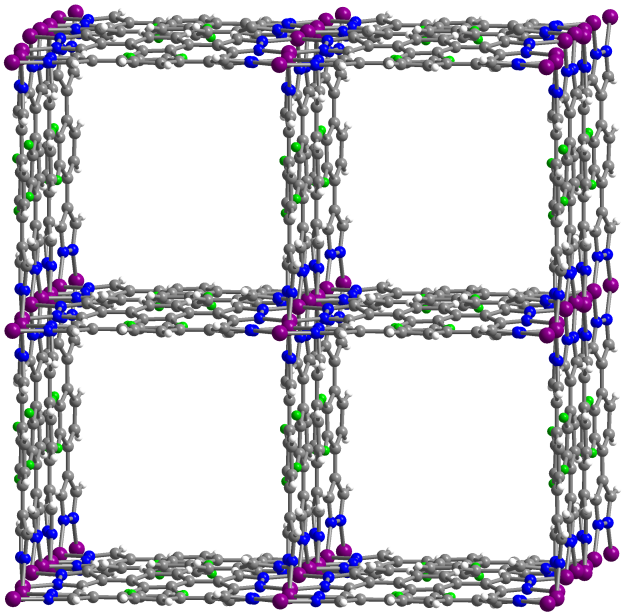

Figure 2.S2. Single-crystal X-ray diffraction structure of Co(*o*-F_2-bdp). Gray, blue, white, purple, and green spheres represent C, N, H, Co, and F atoms, respectively. Note that although the benzene rings were found to be rotationally disordered over two positions, only one position is shown for clarity. DEF molecules in the framework pores were found to be disordered and could not be modeled.

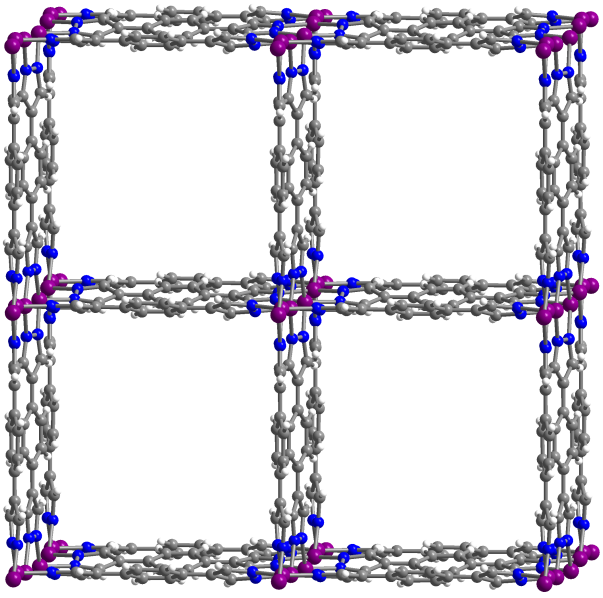

Figure S3. Single-crystal X-ray diffraction structure of Co(D_4-bdp). Gray, blue, white, purple, and green spheres represent C, N, H, Co, and F atoms, respectively. DEF molecules in the framework pores were found to be disordered and could not be modeled.

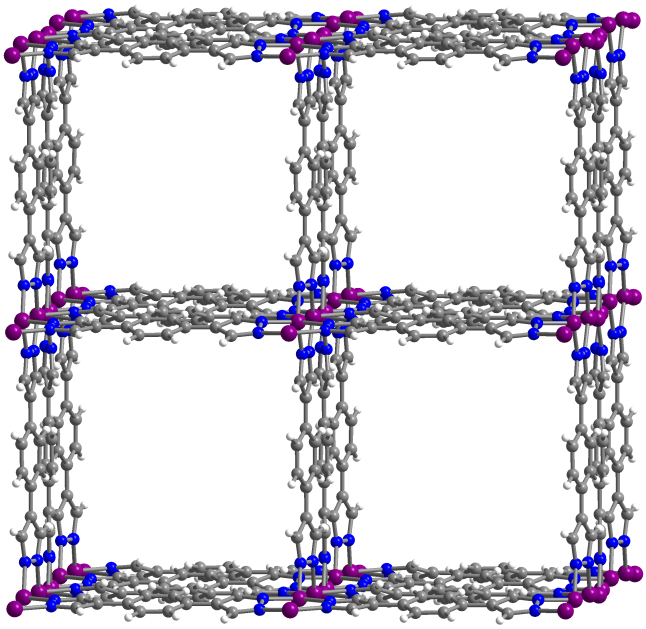

Figure 2.S4. Single-crystal X-ray diffraction structure of Co(bdp). Gray, blue, white, purple, and green spheres represent C, N, H, Co, and F atoms, respectively. DEF molecules in the framework pores were found to be disordered and could not be modeled.

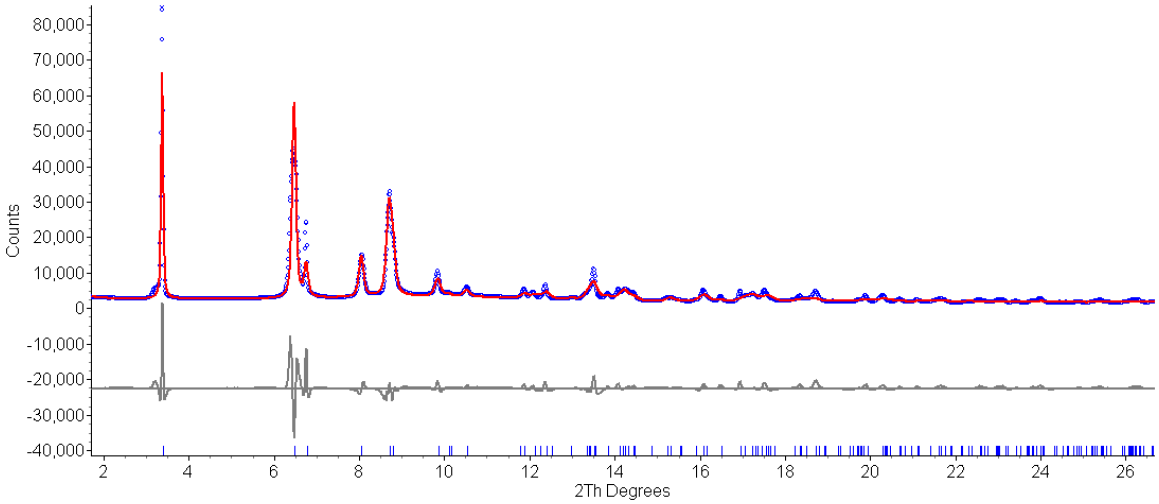

Figure 2.S5. Rietveld refinement plot of activated Co(D_4-bdp) collected at room temperature. Measured scattered intensity is presented with blue dots, the best fit with a red line, and the corresponding difference plot with a gray line. The Bragg reflections are given with blue bars. Note: the peak widths of Co(D_4-bdp) could not be modelled by convoluting conventional Gaussian and Lorentzian functions (or their combinations) with systematic tan(θ) or 1/cos(θ) dependency, respectively, nor could they be modelled with the spherical harmonics approach. This phenomenon is due to the presence of paracrystalinity, explained in detail for Co(bdp).[15]

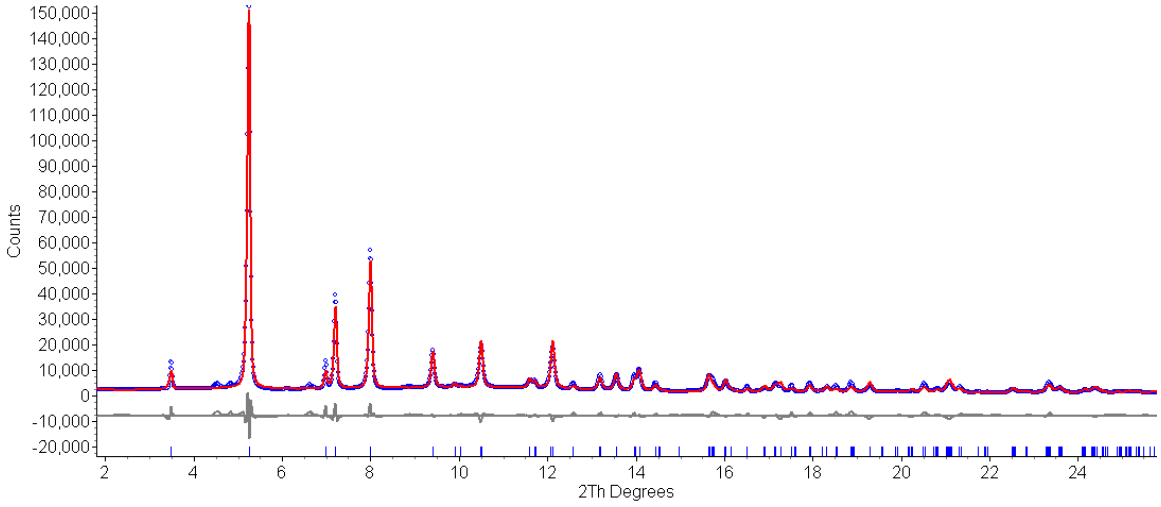

Figure 2.S6. Rietveld refinement plot of activated Co(*p*-Me_2-bdp) collected at room temperature. Measured scattered intensity is presented with blue dots, the best fit with a red line, and the corresponding difference plot with a gray line. The Bragg reflections are given with blue bars.

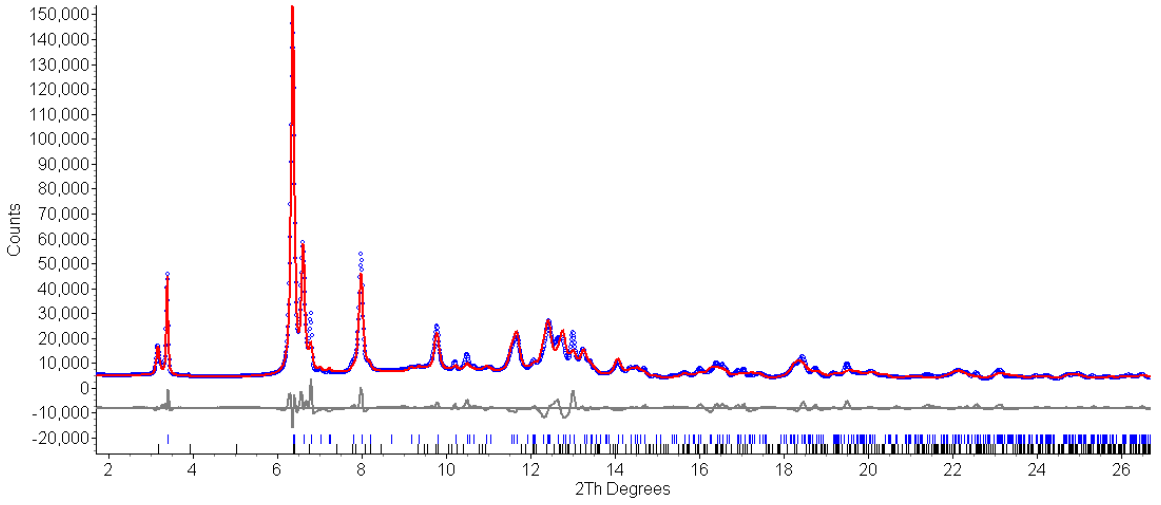

Figure 2.S7. Rietveld refinement plot of activated Co(*p*-F_2-bdp) collected at room temperature. Measured scattered intensity is presented with blue dots, the best fit with a red line, and the corresponding difference plot with a gray line. The Bragg reflections are given with blue bars. Note: the open-pore phase of Co(*p*-F_2-bdp) is present as a minor phase with 1.3 weight % (the Bragg positions are given with black bars).

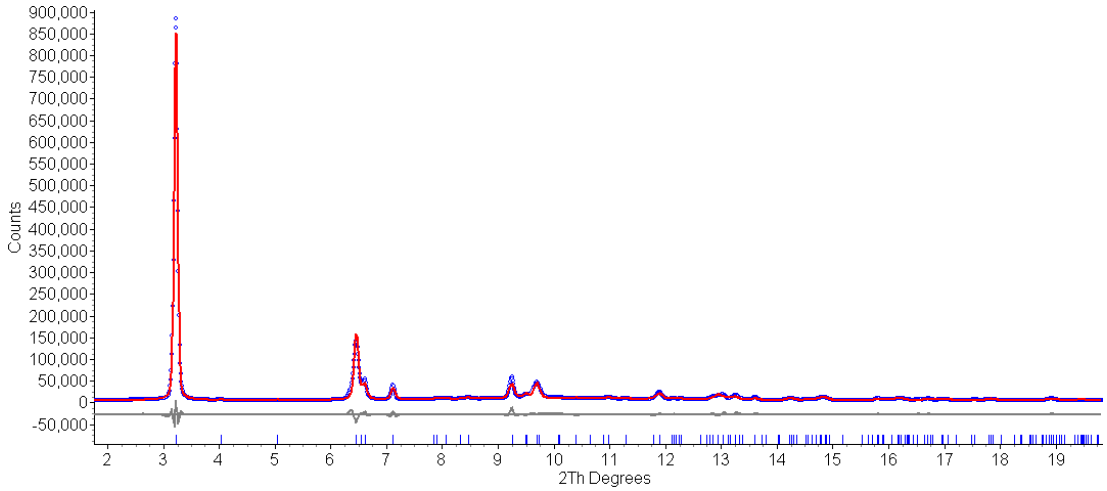

Figure 2.S8. Rietveld refinement plot of activated Co(*p*-F_2-bdp) collected at room temperature and 19.7 bar CH_4 pressure. Measured scattered intensity is presented with blue dots, the best fit with a red line, and the corresponding difference plot with a gray line. The Bragg reflections are given with blue bars.

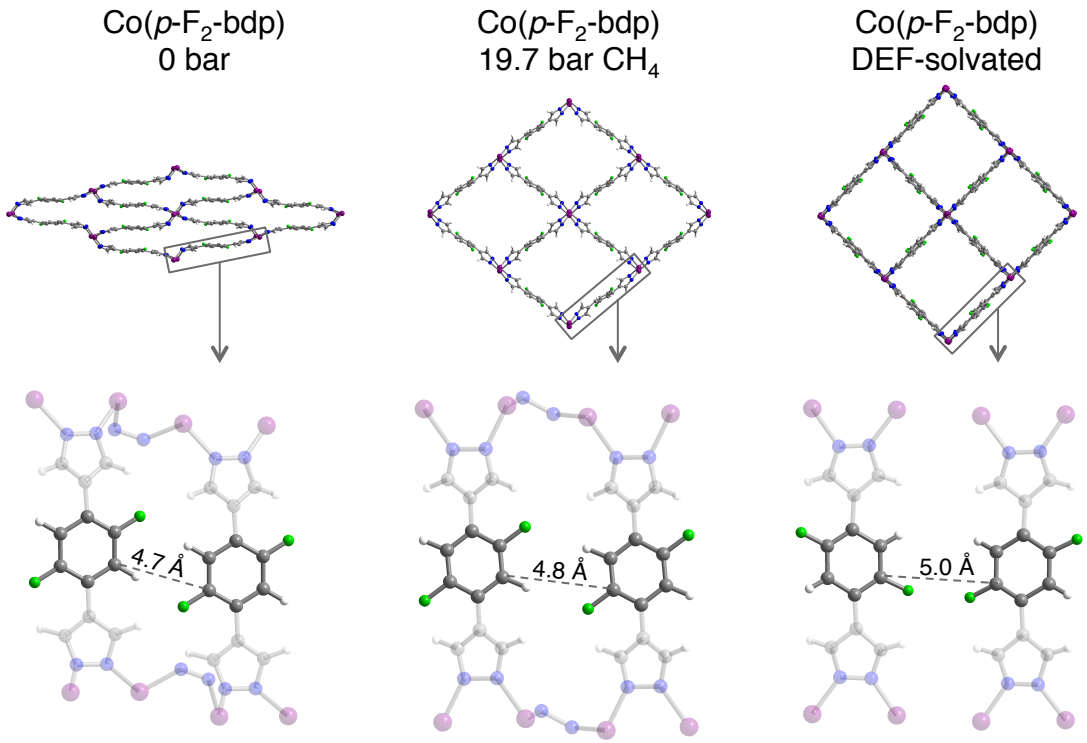

Figure 2.S9. Powder X-ray diffraction structures of Co(*p*-F_2-bdp) under vacuum (left) and under 19.7 bar CH_4 (center) show C–H···F–C interactions between the aryl rings of adjacent ligands. However, these interactions are replaced by F-F interactions when the material is in its fully-expanded, DEF-solvated state (right), implying that the increasing distance between these aryl rings affects the preference for C–F···F–C *versus* C–H···F–C interactions. Gray, blue, white, purple, and green spheres represent C, N, H, Co, and F atoms, respectively.

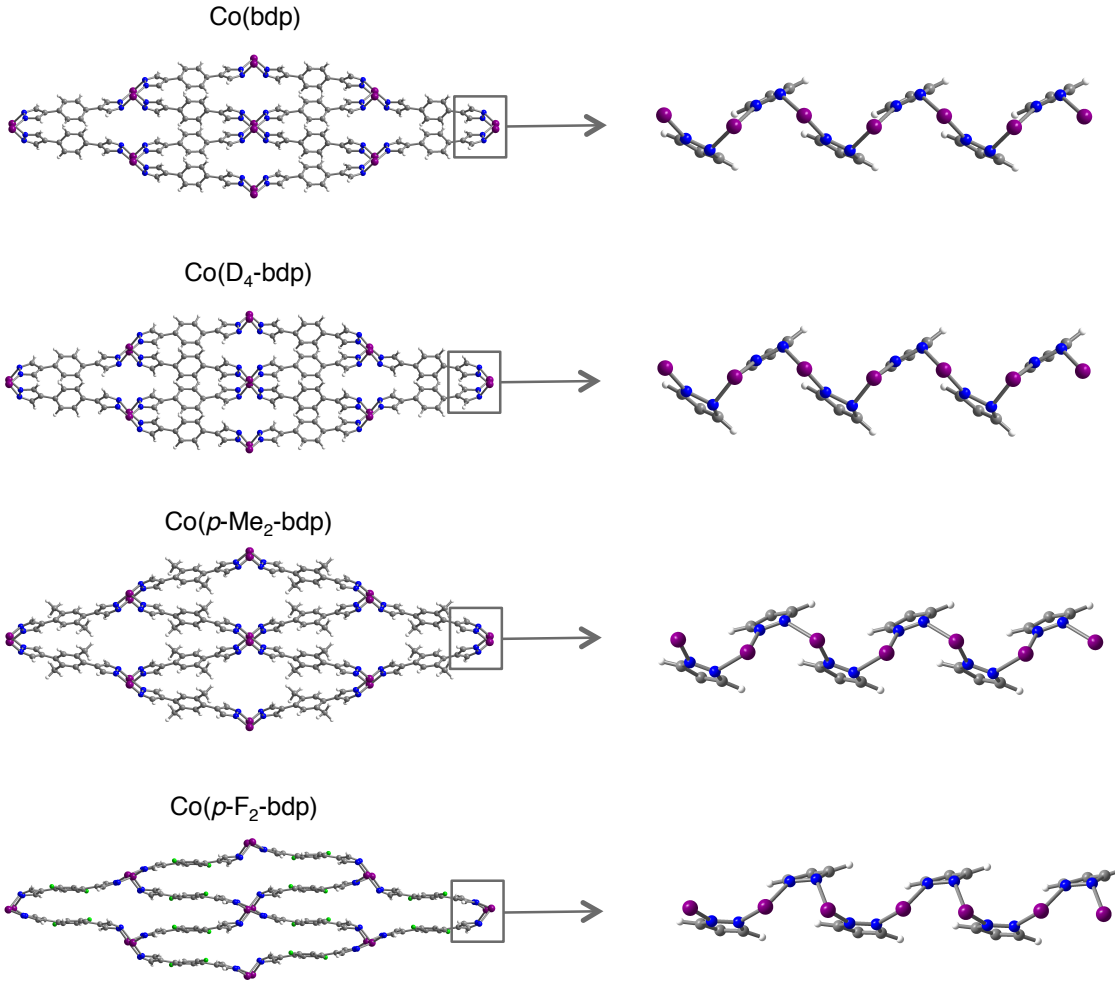

Figure 2.S10. Powder X-ray diffraction structures of activated samples of Co(bdp), Co(D_4-bdp), Co(*p*-Me_2-bdp), and Co(*p*-F_2-bdp), viewed down the pore channel (left) and perpendicular to the chains of cobalt atoms (right). The dihedral angles between adjacent ligands decrease from 73.7° in the case of Co(bdp) to 9.7° in the case of Co(*p*-F_2-bdp), minimizing the edge-to-face π–π interaction between adjacent ligands in the fluorinated material. Gray, blue, white, purple, and green spheres represent C, N, H, Co, and F atoms, respectively.

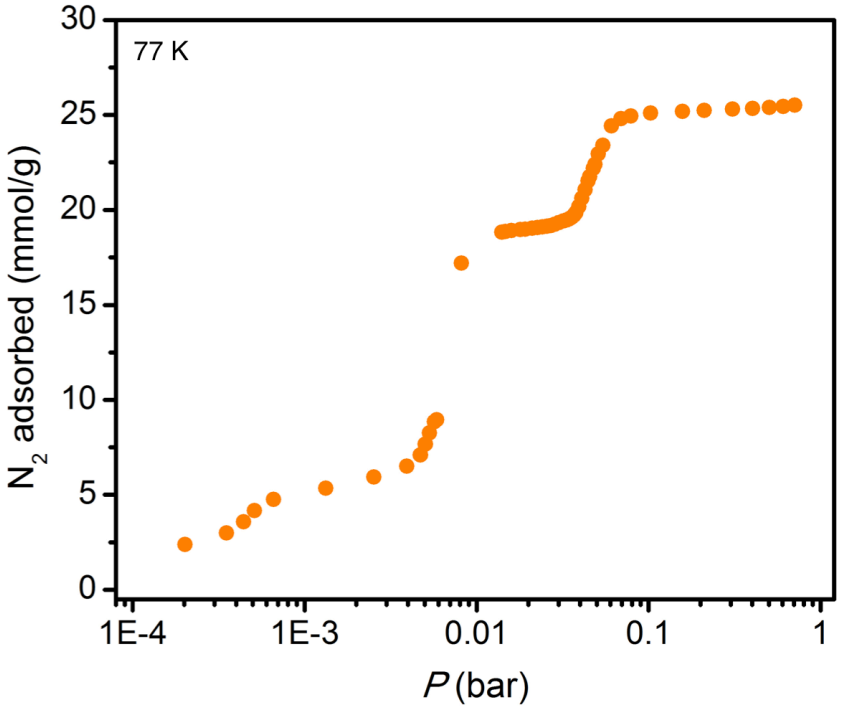

Figure 2.S11. Low-pressure N_2 adsorption in Co(F-bdp).

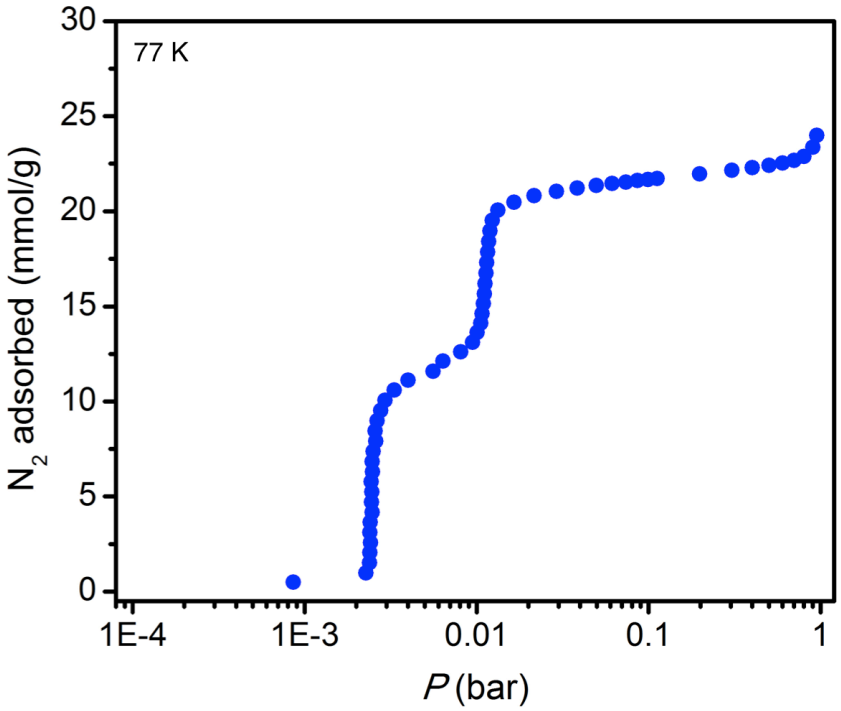

Figure 2.S12. Low-pressure N_2 adsorption in Co(*p*-F_2-bdp).

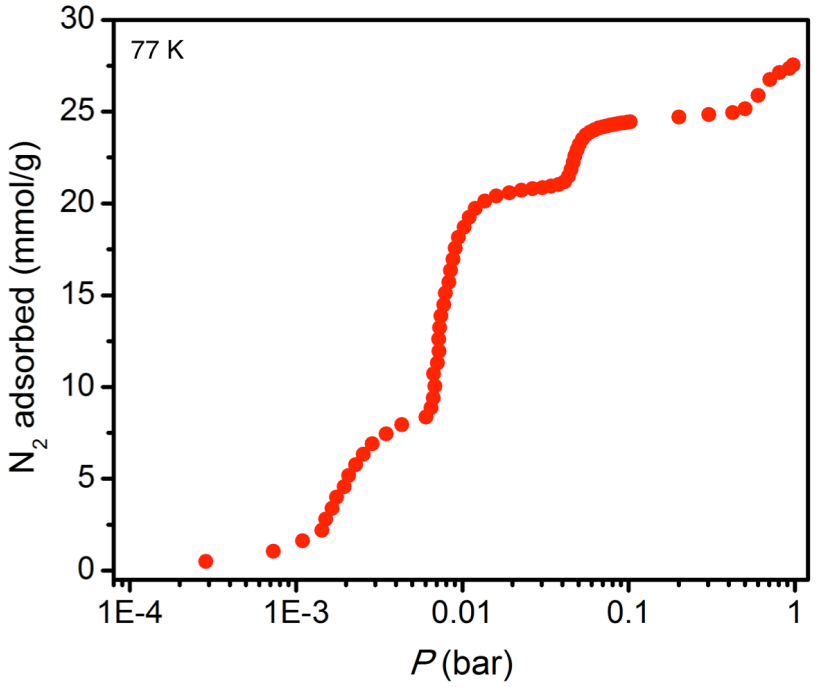

Figure 2.S13. Low-pressure N_2 adsorption in Co(*o*-F_2-bdp).

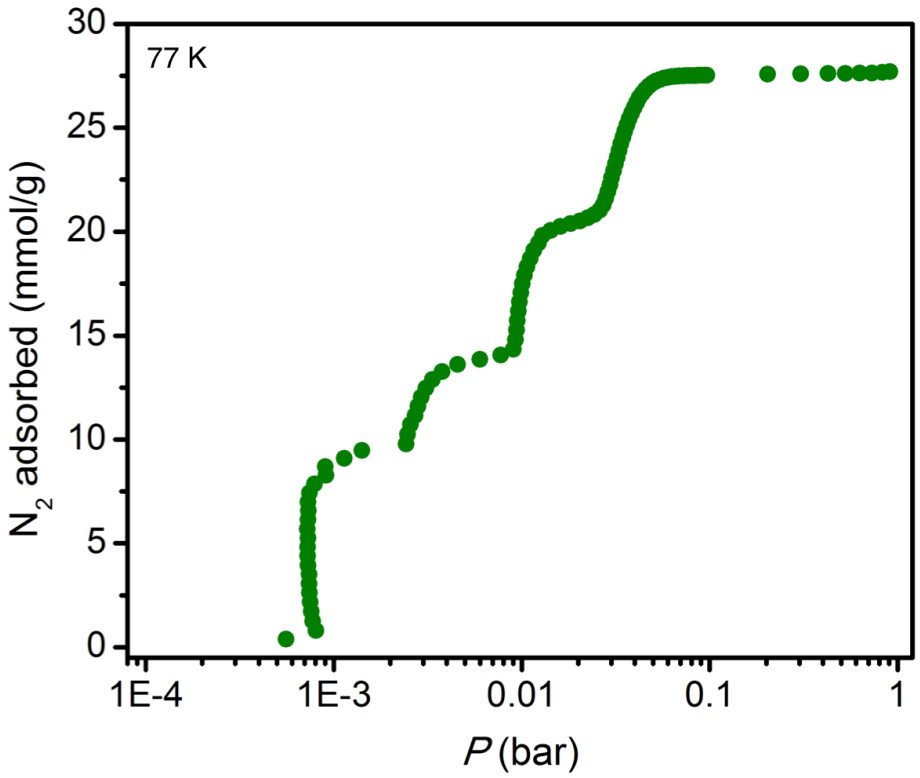

Figure 2.S14. Low-pressure N_2 adsorption in Co(D_4-bdp).

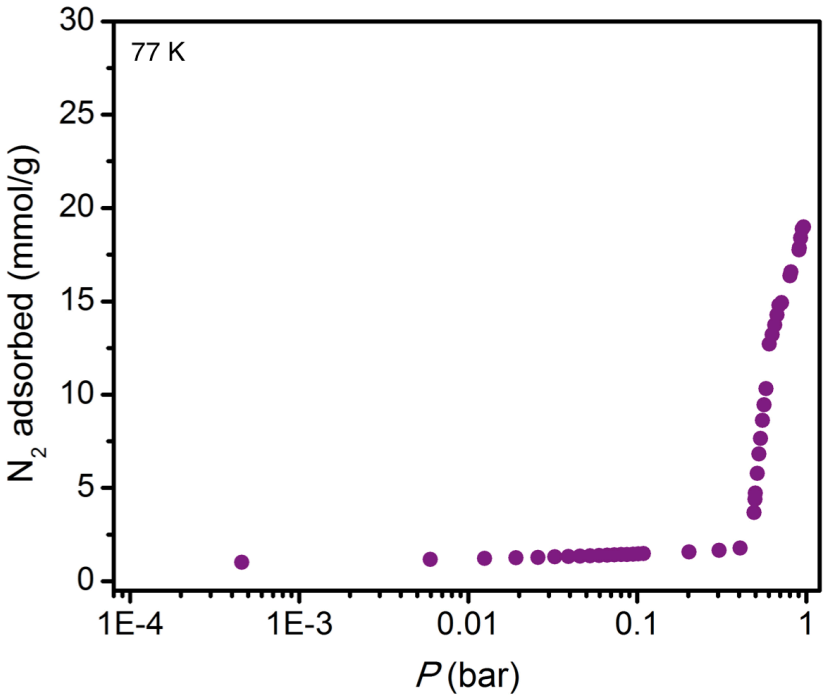

Figure 2.S15. Low-pressure N_2 adsorption in Co(*p*-Me_4-bdp).

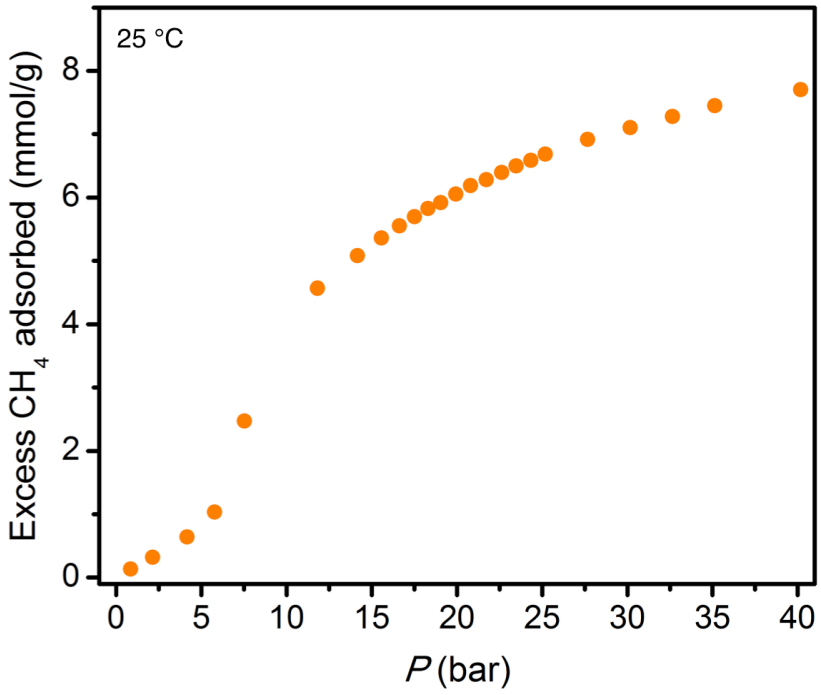

Figure 2.S16. High-pressure CH_4 adsorption in Co(F-bdp).

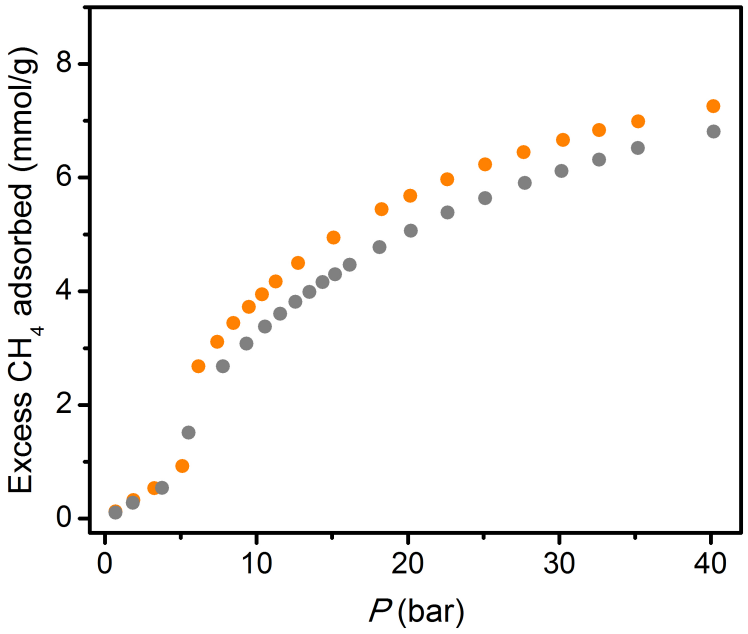

Figure 2.S17. High-pressure CH_4 adsorption in Co(F-bdp) at 25 °C (orange) and 38 °C (gray). Note that this sample of Co(F-bdp) is a different batch than the Co(F-bdp) used to generate the data in Figure S16 and in the main text of this paper, for which variable temperature data was not obtained.

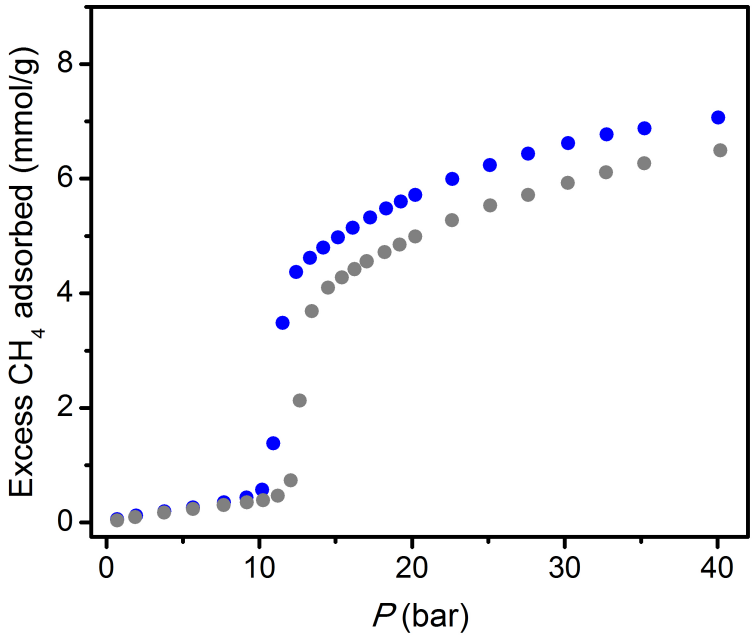

Figure 2.S18. High-pressure CH_4 adsorption in Co(*p*-F_2-bdp) at 25 °C (blue) and 38 °C (gray).

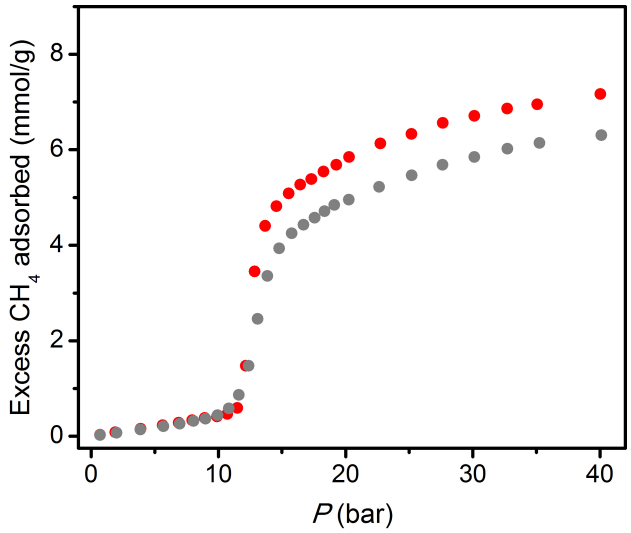

Figure 2.S19. High-pressure CH_4 adsorption in Co(*o*-F_2-bdp) at 25 °C (red) and 38 °C (gray).

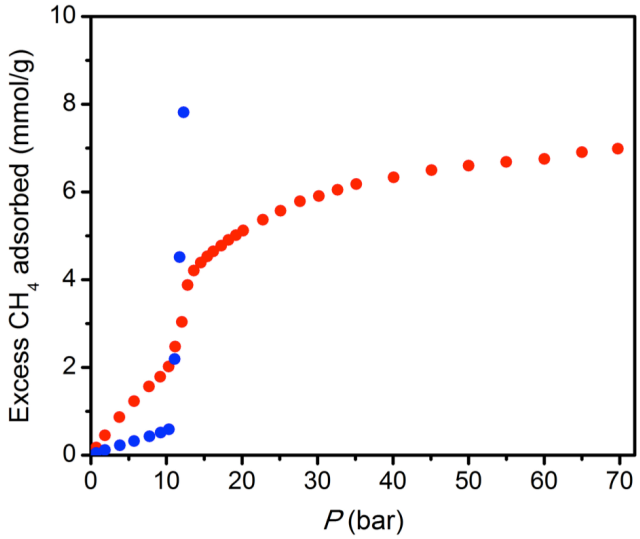

Figure 2.S20. High-pressure CH_4 adsorption in Co(*o*-F_2-bdp), before and after a leak occurred in the high-pressure sample holder (blue and red, respectively). The leak is indicated by the sharp rise in CH_4 adsorption in the blue curve; prior to the leak, the material showed minimal CH_4 adsorption in this pre-step region. After collecting the data shown in blue, the sample holder was removed, re-sealed, and returned to the instrument, and the material was re-activated by heating to 160 °C under vacuum for 12 hours. Subsequently, the red curve showed that the material now adsorbed significant CH_4 in the pre-step region of the isotherm. Because the leak exposed the material to air, this series of experiments indicates that the degradation caused by air exposure leads to pre-step adsorption, perhaps by preventing partially-degraded particles from collapsing under vacuum and achieving a non-porous phase.

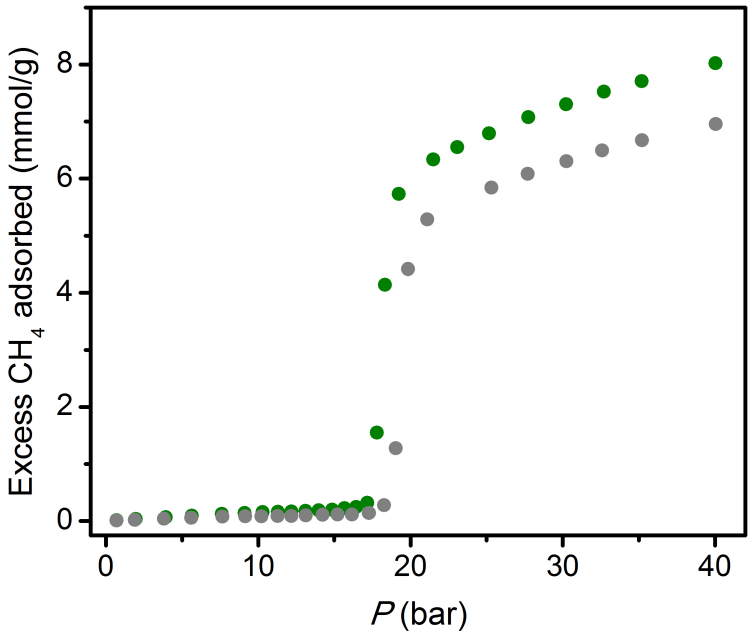

Figure 2.S21. High-pressure CH_4 adsorption in Co(D_4-bdp) at 25 °C (green) and 38 °C (gray).

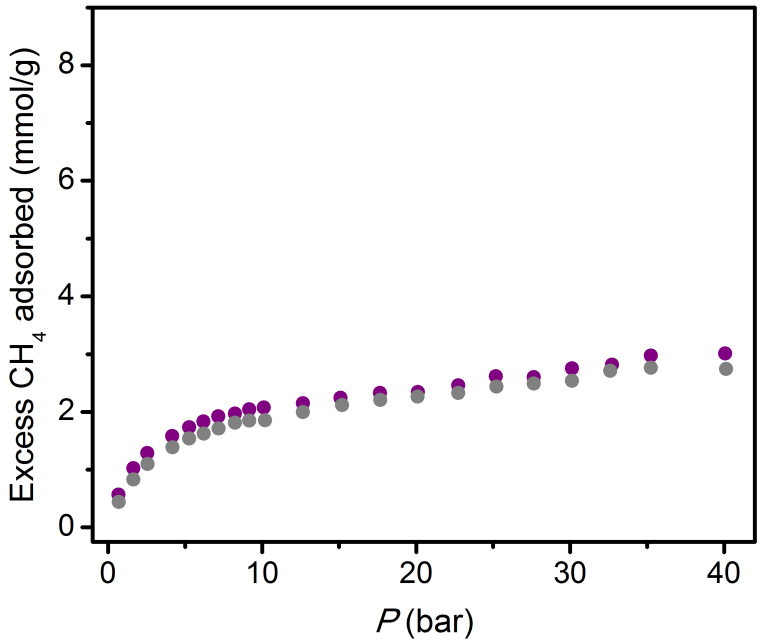

Figure 2.S22. High-pressure CH_4 adsorption in Co(*p*-Me_2-bdp) at 25 °C (purple) and 38 °C (gray).

Supporting References

(1) Kinzel, T.; Yong, Z.; Buchwald, S. L *J. Am. Chem. Soc.* **2010**, *132*, 14073.
(2) Choi, H. J.; Dincă, M.; Long, J. R. *J. Am. Chem. Soc.* **2008**, *130*, 7848.
(3) *SAINT and APEX 2 Software for CCD DIffractometers*, Bruker Analytical X-ray Systems Inc., Madison, WI, USA, 2014.
(4) Sheldrick, G. M. SADABS, Bruker Analytical X-ray Systems Inc., Madison, WI, USA, 2014.
(5) Sheldrick, G.M. (2015). Acta Cryst. A71, 3.
(6) Sheldrick, G.M. (2015). Acta Cryst. C71, 3.
(7) Dolomanov, O. V.; Bourhis, L. J.; Gildea, R. J; Howard, J. A. K.; and Puschmann, H. *J. Appl. Cryst.* **2009**, *42*, 339.
(8) Bruker AXS, Topas, version 4.1. **2007**.
(9) Coelho, A. A. *J. Appl. Cryst*, **2003**, *36*, 86.
(10) Pawley, G. S. *J. Appl. Cryst.* **1981**, *14*, 357.
(11) Andreev, Y. G.; MacGlashan, G. S.; Bruce, P. G. *Phys. Rev. B* **1997**, *55*, 12011.
(12) Rietveld, H. M. *J. Appl. Crystallogr*. **1969**, *2*, 65.
(13) Mercury CSD 3.3 (Build RC5), **2013**.
(14) Düren, T., Millange, F., Férey, G., Walton, K. S. & Snurr, R. Q. *J. Phys. Chem. C* **2007**, *111*, 15350.
(15) Mason, J. A.; Oktawiec, J.; Taylor, M. K.; Hudson, M. R.; Rodriguez, J.; Bachman, J. E.; Gonzalez, M. I.; Cervellino, A.; Guagliardi, A.; Brown, C. M.; Llewellyn, P. L.; Masciocchi, N.; Long, J. R. *Nature* **2015**, *527,* 357.

Chapter 3: Near-Perfect CO_2/CH_4 Selectivity Achieved through Reversible Guest Templating in the Flexible Metal–Organic Framework Co(bdp)

3.1. Introduction

Industrial separations are a major source of global energy demand and greenhouse gas emissions, currently comprising ~15% of the total U.S. energy consumption.[1] The separation of CO_2 from CH_4 is of particular importance due to the widespread and increasing use of natural gas as a fuel.[2,3] Highly selective adsorbents that exhibit reversible gas uptake could significantly reduce the energy spent on gas separations,[4] but the design of porous adsorbents that completely exclude one species while showing high capacities for another is difficult when considering mixtures of adsorbate molecules with similar sizes and properties.

Due to their high internal surface areas and tunable pore architectures, metal–organic frameworks are regarded as a particularly promising class of adsorbents for gas separation applications,[5,6] and some frameworks additionally exhibit structural flexibility that allows them to undergo reversible phase changes in response to external stimuli such as gas pressure.[7-9] Adsorbate-induced phase changes typically manifest as steep steps in adsorption isotherms, and these steps can occur at different pressures, depending on the adsorbate. Because of this unique adsorption behavior, flexible metal–organic frameworks have garnered increasing attention as possible gas separation materials.[10-35] However, while single-component adsorption isotherms for these materials may suggest selectivity for a given gas within a certain pressure range, very few studies have carried out the necessary multicomponent equilibrium adsorption experiments to confirm selectivity and demonstrate that it arises from adsorbate-dependent expansion.[16,18,21] Much therefore remains unknown about this separation mechanism in flexible frameworks, such as whether pore opening induced by one molecule will then enable the simultaneous uptake of other molecules. Assuming this simultaneous uptake does not occur, it is then unknown whether selectivity arising in a region where only one gas induces a phase change (e.g., the region highlighted in gray in Figure 3.1) will persist beyond subsequent steps in the respective single-component isotherms, and under what conditions the adsorption selectivity may be lost.

We sought to address these unknowns by studying the CO_2/CH_4 separation performance of the metal–organic framework Co(bdp) (bdp^{2-} = 1,4-benzenedipyrazolate). This framework exhibits significant structural flexibility under increasing gas pressure, undergoing endothermic structural phase changes in response to adsorption, and shows one of the highest CH_4 capacities to date.[36-39] Composed of coordinatively saturated, tetrahedral cobalt(II) centers linked by bdp^{2-} ligands (Figure 3.1a), Co(bdp) contains no open metal sites and is completely nonporous to gases in its collapsed phase, traits which simplify the interpretation of adsorption data and facilitate an unhindered investigation into the effect of structural phase changes on adsorption selectivities. Herein, we use multicomponent equilibrium adsorption measurements supplemented with *in situ* powder X-ray diffraction analyses to demonstrate high CO_2/CH_4 selectivity in Co(bdp) and to probe the limits of this selectivity.

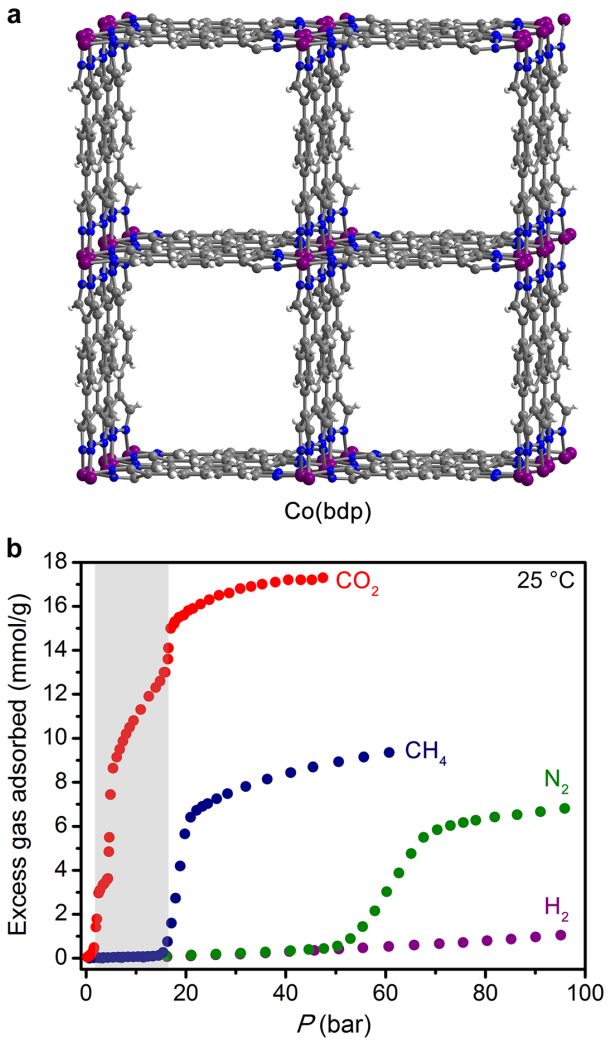

Figure 3.1. (a) Single-crystal X-ray diffraction structure at 298 K of the diethylformamide-solvated, fully-expanded phase of Co(bdp) showing the one-dimensional square channels of this material, which are bounded by rows of organic ligands and chains of tetrahedral cobalt(II) centers.[39] Solvent molecules in the framework pores are not depicted. Gray, blue, white, and purple spheres represent C, N, H, and Co atoms, respectively. (b) Single-component isotherms for CO_2, CH_4, N_2, and H_2 adsorption in Co(bdp) at 25 °C showing adsorbate-dependent phase change pressures. The isotherms suggest that Co(bdp) exhibits perfect CO_2/CH_4 selectivity within the gray highlighted region, a hypothesis examined with multicomponent adsorption experiments in this work. Desorption data and variable-temperature isotherm data are provided in the Supporting Information.

3.2. Experimental Section

Synthesis. Co(bdp) and Co(F-bdp) were synthesized according to previously published procedures;[38,39] synthetic details are provided in the Supporting Information.

Single-Component Gas Adsorption Experiments. Ultra-high purity (≥99.998% purity) dinitrogen, helium, carbon dioxide, methane, and dihydrogen were used for all adsorption measurements. Adsorption isotherms for pressures in the range of 0−1.1 bar were measured using a Micromeritics ASAP 2020 or 2420 gas adsorption analyzer. Activated samples were transferred under a N_2 atmosphere to preweighed analysis tubes, which were capped with a Transeal. Each sample was evacuated on the instrument until the outgas rate was less than 3 μbar/min. The evacuated analysis tube containing degassed sample was then transferred to an electronic balance and weighed to determine the mass of sample (typically 30−50 mg). For cryogenic measurements, the tube was fitted with an isothermal jacket. The tube was then transferred back to the analysis port of the instrument, and the outgas rate was again confirmed to be less than 3 μbar/min prior to analysis.

Adsorption isotherms for pressures in the range of 0−100 bar were measured on an HPVA-II-100 gas adsorption analyzer from Particulate Systems, a Micromeritics company. In a typical measurement, 0.2−0.5 g of activated sample was loaded into a tared stainless steel sample holder inside a glovebox under a N_2 atmosphere. The sample holder was weighed to determine the sample mass and was then connected to the high-pressure assembly inside the glovebox. The sample holder was then transferred to the HPVA-II-100, connected to the analysis port of the instrument via an OCR fitting, and evacuated at room temperature for at least 2 h. The sample holder was then placed inside an aluminum recirculating dewar connected to a Julabo FP89-HL isothermal bath filled with Syltherm XLT fluid. The temperature stability of the isothermal bath was ±0.02 °C. Methods for accurately measuring the relevant sample freespaces, involving the expansion of He from a calibrated volume at 0.7 bar and 25 °C to the evacuated sample holder, have been described in detail previously.[40] Nonideality corrections were performed using the compressibility factor of the appropriate gas, tabulated in the NIST REFPROP database,[41] for each measured temperature and pressure.

Multicomponent Gas Adsorption Experiments. Pre-mixed cylinders containing 50:50 and 10:90 CO_2:CH_4 gas mixtures were purchased from Praxair with an analytical accuracy of ±1%. Co(bdp) was dosed with one of the gas mixtures using the HPVA-II-100 instrument as described above and allowed to reach equilibrium, as evidenced by a pressure change of less than 0.003 bar over 2 min. The gas pressure of the manifold was recorded before and after equilibration (as is done for each point of a single-component isotherm). After taking each data point, the sample holder was sealed without desorbing the gas from the sample, removed from the HPVA-II-100, and attached to an evacuated volume. The gas mixture in the headspace of the sample holder as well as the gas adsorbed on the sample was expanded into the evacuated volume by heating the sample holder to 160 °C for 1 h. The gas mixture was then sampled with a mass spectrometer (MKS Microvision 2) to determine the relative concentrations of CO_2 and CH_4 that were present in the sample holder upon removal from the HPVA-II-100 instrument. Using the free-space and adsorption data provided by the HPVA-II-100 instrument, the CO_2:CH_4 ratio obtained from the mass spectrometer was used to calculate the amount of CO_2 and CH_4 adsorbed by Co(bdp). A complete discussion of these calculations is presented in the Supporting Information.

***In situ* Powder X-ray Diffraction Experiments.** High-resolution powder X-ray diffraction patterns were collected for Co(bdp) at Beamline 17-BM-B at the Advanced Photon Source of Argonne National Laboratory, with an average wavelength ranging from 0.4 to 0.7 Å. Scattered intensity was recorded by a PerkinElmer a-Si Flat Panel detector. Prior to measurement, samples were packed in quartz glass capillaries of 1.5 mm diameter under an N_2 atmosphere. Each capillary was attached to a custom-designed gas-dosing cell equipped with a gas valve, which was then mounted onto the goniometer head and connected to a gas-dosing manifold for *in situ* diffraction measurements. First, diffraction data were collected at room temperature under dynamic vacuum to obtain the structure of the material in the collapsed phase. Subsequently, the gas-dosing manifold was used to dose increasing pressures of pure CO_2, and diffraction data was collected after the sample reached equilibrium at each pressure (as evidenced by a constant pressure readout and unchanging diffraction pattern). The sample was then evacuated to regenerate the collapsed phase and subsequently dosed with increasing pressures of a 50:50 mixture of CO_2:CH_4. Diffraction data were again collected after the sample reached equilibrium at each mixed-gas pressure. A sample temperature of 298 K was maintained for all measurements by an Oxford CryoSystems Cryostream 800. Analysis of all diffraction data is discussed in the Supporting Information.

3.3. Results and Discussion

Single-Component Gas Adsorption Behavior. Single-component CO_2, CH_4, N_2, and H_2 adsorption isotherms were collected for Co(bdp) at 25 °C and are shown in Figure 3.1b (CO_2 and CH_4 isotherms at 25 °C for Co(bdp) have been reported previously;[37,38] variable-temperature isotherm data are provided in the Supporting Information). These isotherms illustrate that phase changes in Co(bdp) occur at markedly different pressures for different adsorbates: the first phase change (from a nonporous, collapsed structure to a porous, expanded structure) occurs at ~2 bar for CO_2 but not until 18 bar for CH_4 and 60 bar for N_2. While H_2 has been found to induce phase changes in Co(bdp) at cryogenic temperatures,[36] no phase change was observed below 100 bar for H_2 at 25 °C. Although the phase change pressure is influenced by a number of thermodynamic parameters, the relative position of the steps in the CO_2, CH_4, N_2, and H_2 isotherms can be explained in part by the relative binding enthalpies of these gases: Stronger-binding gases like CO_2 provide more energetic stabilization for the expanded phase, so less gas pressure is necessary to trigger the expansion.[42] The wide variation in phase change pressures implies that Co(bdp) has the potential to be used for numerous separations involving CO_2, CH_4, N_2, and H_2, including in the industrially important processes of natural gas sweetening,[43] hydrogen production,[44] and biogas purification.[45] We chose to focus our characterization efforts on the removal of CO_2 from mixtures with CH_4 because of the industrial relevance of this separation, because both the CO_2- and CH_4-induced phase change pressures are compatible with a variety of adsorption and diffraction experiments, and because of the notably high CO_2 capacity of Co(bdp).[46]

Equilibrium Multicomponent Adsorption Experiments. Comparison of the CO_2 and CH_4 single-component adsorption isotherms in Figure 3.1b suggests that Co(bdp) would be highly selective for CO_2 at pressures below those corresponding to the CH_4-induced phase change. However, calculating non-competitive selectivities for CO_2 and CH_4 from

these data would erroneously exclude the possibility that Co(bdp) could expand to a novel phase capable of then accommodating a mixture of CO_2 and CH_4 molecules in the pores. Furthermore, using ideal adsorbed solution theory to model mixed-gas isotherms (as is often done for rigid frameworks) is inappropriate for structurally flexible materials such as Co(bdp),[38] because this theory assumes that the thermodynamic state of the adsorbent remains constant during adsorption.[47] While progress has been made in developing a more representative computational method to predict mixed-gas selectivity in flexible metal–organic frameworks from their pure-gas isotherms,[48] the most thorough way to experimentally determine a flexible framework's selectivity is to perform multicomponent adsorption experiments, in which a sample is exposed to the relevant gas mixture. However, when multicomponent selectivity is reported in the literature, it is usually as the result of the dynamic breakthrough measurements.[49-50] The results of breakthrough experiments depend on many factors in addition to the inherent properties of the adsorbent, including gas flow rate, column size, shape, and length, packing density, and extra-column effects,[51] whereas equilibrium adsorption measurements entail fewer experimental variables and are not subject to kinetic effects. As such, equilibrium measurements provide a more fundamental picture of adsorbent behavior and enable direct comparisons between materials.[52]

Therefore we devised a multicomponent adsorption experiment that would allow us to study high-pressure, mixed-gas adsorption in Co(bdp) under equilibrium conditions. In brief, Co(bdp) was dosed with high pressures of a CO_2/CH_4 mixture and allowed to equilibrate at 25 °C, and mass spectrometry was then used to determine the composition of the adsorbed gas and the gas in the headspace (see the Supporting Information for further details). This experiment was performed for equilibrium pressures of 6.7, 13.9, and 25.3 bar, corresponding to equilibrium CO_2:CH_4 molar ratios of 46:54, 42:58, and 43:57, respectively (Figure 3.2a). For each examined pressure, the amount of CO_2 adsorbed coincides with the pure-CO_2 isotherm when plotted versus the equilibrium partial pressure of CO_2, while the amount of CH_4 adsorbed approaches zero for all cases. Thus, the hypothesis based on the single-component CO_2 and CH_4 isotherms is indeed correct, and under the conditions tested Co(bdp) has an outstanding CO_2/CH_4 selectivity. Because Co(bdp) adsorbs approximately no CH_4 at the examined pressures, calculated selectivity values are not meaningful, and the framework is most accurately described as having near-perfect CO_2 selectivity under these conditions.

***In situ* Powder X-ray Diffraction with Mixed-Gas Dosing.** Synchrotron X-ray powder diffraction experiments were employed to further examine the phase behavior of Co(bdp) upon exposure to a mixture of CO_2 and CH_4. Data were first collected on an evacuated sample of the framework and confirmed that in this state Co(bdp) exhibits a collapsed structure identical to that previously published[38] (Rietveld refinement results are provided in Figure 3.S22). The activated sample was then dosed with increasing pressures of pure CO_2 from 0 to 19.4 bar in 0.5–2 bar increments, and X-ray diffraction data were collected at each pressure following sample equilibration, as evidenced by a lack of change in both pressure and the diffraction pattern (Figure 3.3a). After obtaining diffraction data for the highest pressure, the sample was evacuated to recover the collapsed phase, and a similar procedure was repeated with a 50:50 mixture of CO_2:CH_4 dosed at pressures ranging from 1.3 to 50 bar (Figure 3.3b).

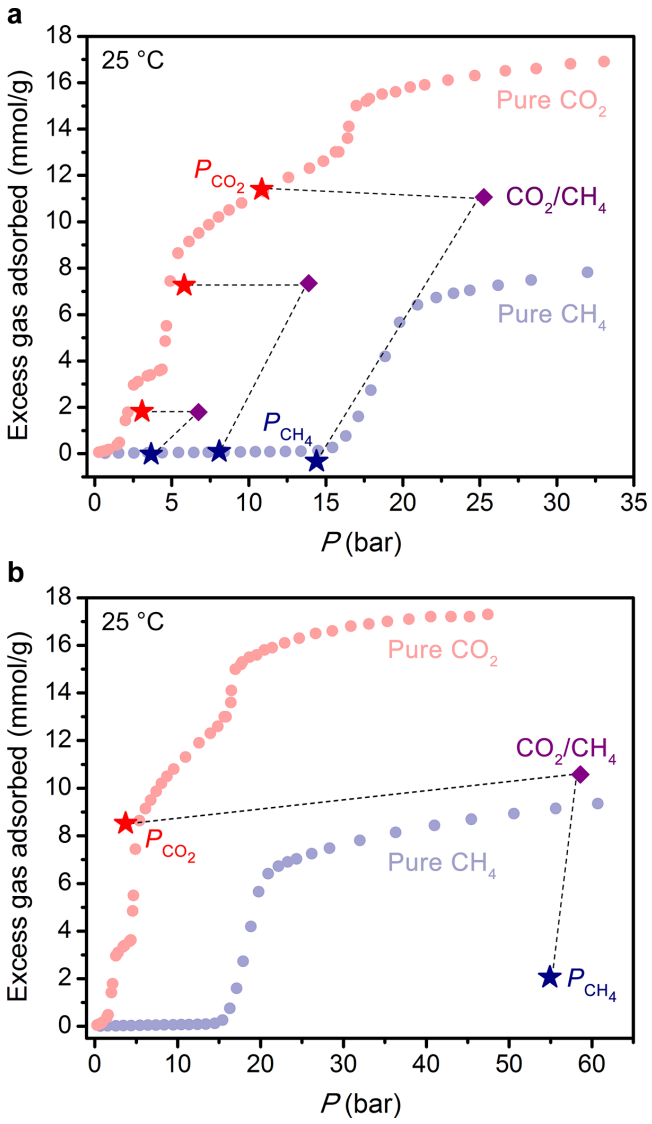

Figure 3.2. (a) Multicomponent adsorption experiments for CO_2/CH_4 mixtures in Co(bdp) show near-perfect CO_2 selectivity at 6.7, 13.9, and 25.3 bar, under equilibrium CO_2:CH_4 molar ratios of 46:54, 42:58, and 43:57, respectively. (b) Multicomponent adsorption experiment performed under a CH_4-rich atmosphere (with an equilibrium CO_2:CH_4 molar ratio of 6:94) shows that Co(bdp) adsorbs a only small amount of CH_4 at this ratio, leading to a selectivity of 61 ± 4. For (a) and (b), purple diamonds represent the overall amount of gas adsorbed by Co(bdp) (y-axis) from a CO_2/CH_4 mixture at a given equilibrium pressure (x-axis). Each purple diamond is paired with a corresponding red and blue star: red stars represent the CO_2 adsorbed from the mixture (y-axis) at the equilibrium partial pressure of CO_2 (x-axis), and blue stars represent the CH_4 adsorbed from the mixture (y-axis) at the equilibrium partial pressure of CH_4 (x-axis). Single-component isotherms of CO_2 (red circles) and CH_4 (blue circles) in Co(bdp) are shown for reference.

A comparison of the diffraction patterns obtained after pure-CO_2 dosing with those obtained after CO_2/CH_4 dosing reveals these patterns to be strikingly similar at comparable CO_2 partial pressures (and distinct from the previously published CH_4-dosed diffraction patterns[38]). Indeed, diffraction patterns collected for Co(bdp) equilibrated with 3.6 bar of pure CO_2 and with 7.2 bar of a 50:50 CO_2:CH_4 mixture (P_{CO2} = 3.6 bar) were solved to yield identical structural models that represent the phase giving rise to the first plateau in the pure-CO_2 adsorption isotherm (Figure 3.3d,e). The adsorbed gas molecules could be located in both structures and were identified and refined as CO_2 only. The complete exclusion of CH_4 can be understood by examining the size of the channels in this initial expanded phase of the framework, which opens just enough to accommodate a single CO_2 molecule per formula unit but no additional molecules of CO_2 or CH_4 (Figure 3.3e). This CO_2 adsorption behavior is reminiscent of hydrocarbon selectivity recently identified in a copper-based metal–organic framework, which behaves as an ideal molecular sieve with pores that are sized to adsorb acetylene while completely excluding ethylene.[53] Similarly, Co(bdp) can be considered as a CO_2-templated molecular sieve with flexibility that allows it to achieve pores sized for near-perfect CO_2 selectivity, since incorporation of an occasional, differently-shaped methane molecule would destabilize many surrounding unit cells within the crystal. Importantly, this highly selective templating is reversible, and the collapsed nonporous phase can be regenerated upon CO_2 desorption. Upon increasing the dosed CO_2 partial pressures beyond the magnitudes associated with the first plateau in the pure-gas isotherm, the diffraction patterns undergo successive discrete changes associated with structural expansions of the framework. In between these discrete phase changes, which are marked by the sudden appearance of new diffraction peaks and the disappearance of others, Co(bdp) exhibits "breathing" behavior—i.e., a gradual expansion in response to increasing gas pressure. This framework breathing is evidenced by gradually shifting diffraction peaks, in contrast to the discrete phase changes described above (Figure 3.3a,b). These more subtle expansions are associated with shallow increases in the CO_2 adsorption capacity (for example, from 8.6 to 13.0 mmol/g over 5.4–16.5 bar in the pure CO_2 isotherm, Figure 3.1).

As the CO_2/CH_4-dosed material expands due to breathing and phase changes, the *in situ* diffraction patterns yield unit cell volumes that are similar to or greater than those of the previously reported CH_4-expanded phase of Co(bdp),[38] indicating that the framework is sufficiently expanded to admit CH_4 molecules into the pores. For example, equilibration with 14.9 bar of the 50:50 CO_2:CH_4 mixture leads to an increase in unit cell volume from 1182.97(9) $Å^3$ in the nonporous phase[38] to 2185.5(11) $Å^3$ (Pawley refinement provided in Figure 3.S27), which is similar to that of the CH_4-expanded phase (2293.8(5) $Å^3$)[38]. In spite of its large unit cell volume, Co(bdp) continues to exhibit near-perfect CO_2/CH_4 selectivity in this pressure region, as evidenced by the 13.9 bar data point in Figure 3.2. Consequently, the remarkable CO_2/CH_4 selectivity in this region can no longer be ascribed to size-exclusion and instead likely arises due to the formation of a reversible CO_2-templated clathrate within the pores, with a packing arrangement that maximizes the van der Waals contacts between CO_2 molecules and the walls of the framework. The ability to form guest-specific clathrates, with pores templated around an optimal packing of identical guest molecules, confers a distinct advantage on highly flexible frameworks such as Co(bdp) for gas separation applications.

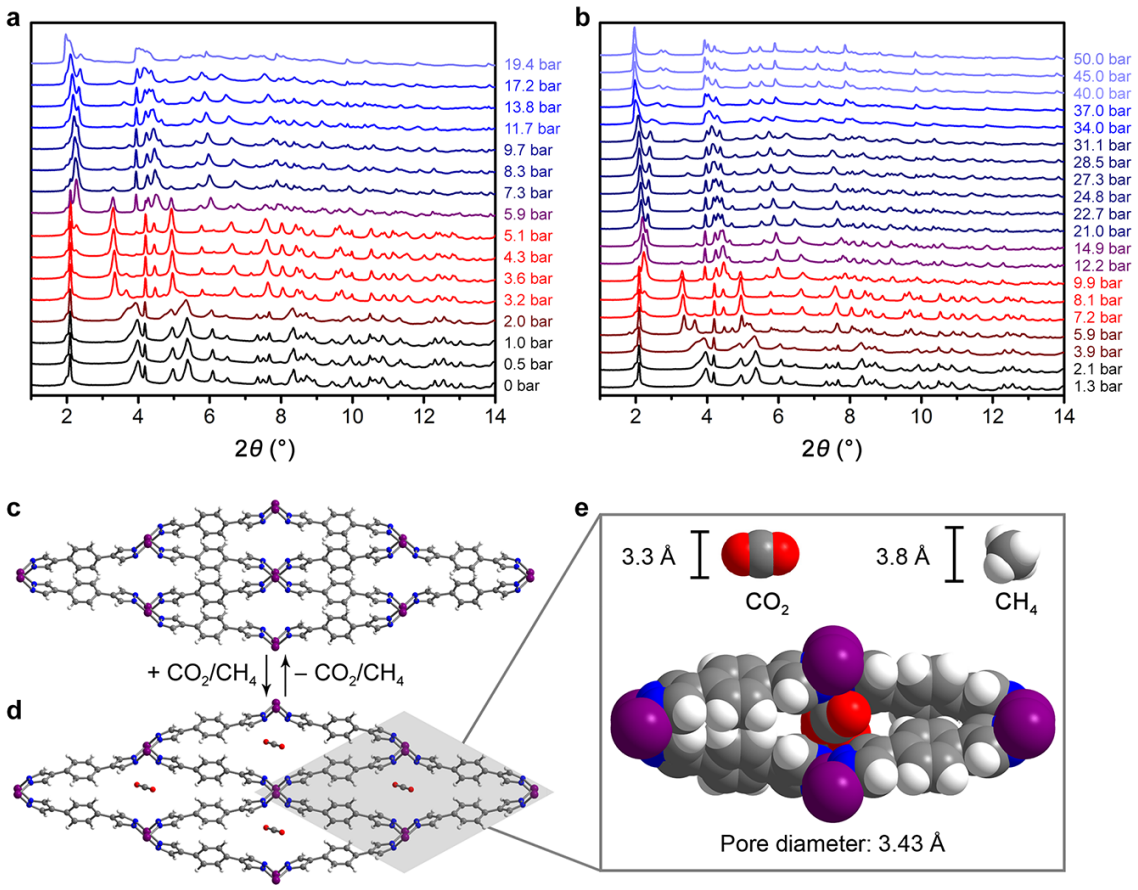

Figure 3.3. (a, b) Powder X-ray diffraction data for Co(bdp) dosed with pure CO_2 (a) and a 50:50 mixture of CO_2:CH_4 (b) over a range of pressures. In both data sets, the abrupt appearance or disappearance of peaks indicates discrete phase changes, whereas gradually shifting peaks indicate framework breathing. Colors are for clarity only. All data were collected at λ = 0.45336 Å and 25 °C. (c, d) Both pure CO_2 at 3.6 bar and a 50:50 CO_2:CH_4 mixture at 7.2 bar induce a structural change in Co(bdp), resulting in an expansion of the one-dimensional channels of the collapsed framework (c) to an aperture ideally-sized to adsorb CO_2 and exclude CH_4 (d). Gray, blue, white, purple, and red spheres represent C, N, H, Co, and O atoms, respectively. (e) The pore diameter of 3.43 Å refers to the distance between opposing N atoms across the one-dimensional channel (in the collapsed phase, this distance is 1.55 Å.) The kinetic diameters of CO_2 and CH_4 (3.3 and 3.8 Å, respectively) are shown for comparison.

Differential Enthalpy of CO_2 versus CH_4 Adsorption. A more quantitative comparison of the energetic favorability of a CO_2-templated pore compared to a CH_4-templated pore can be made by examining the differential enthalpy of adsorption (h_{ads}) for each gas within Co(bdp). To determine h_{ads} of CO_2 adsorption, CO_2 adsorption isotherms were collected across a range of temperatures (Figure 3.4a; isotherm fitting and h_{ads} calculations are described in the Supporting Information.) Similar to the data previously reported for CH_4,[38] a plot of the differential enthalpies of CO_2 adsorption reveals significant reductions in the amount of heat released upon CO_2 adsorption during the discrete, endothermic structural phase changes relative to the regions between these phase changes (Figure 3.4b). For comparison, the isostructural metal–organic frameworks Ni(bdp) and Zn(bdp), which retain their expanded framework structures upon desolvation and do not exhibit flexibility, both display differential enthalpies of CO_2 adsorption of –20 kJ/mol at zero coverage.[54] Notably, these h_{ads} values are very close to those observed for Co(bdp) between its CO_2-induced phase changes. During the first phase change, Co(bdp) shows h_{ads} values in the range of –24 to –26 kJ/mol, which are significantly lower in magnitude than what might be expected, given that each CO_2 molecule is tightly enclathrated within the framework (Figure 3.3d,e). During the second and third CO_2-induced phase changes, the magnitude of h_{ads} plummets dramatically, reaching values as small as –11 and –16 kJ/mol, respectively. Thus, the structural phase changes of Co(bdp) both give rise to selective CO_2 adsorption, and, because of their endothermic nature, can also serve to substantially mitigate the amount of heat that must be dissipated during adsorption.

It is important to note that the differential enthalpy of adsorption for CH_4 in Co(bdp) is much lower than for CO_2, varying from –8 kJ/mol during the first phase change to –14 kJ/mol after the phase change.[38] Therefore it is much more enthalpically favorable for Co(bdp) to adopt a pure-CO_2 phase rather than to adopt a pure-CH_4 phase, or even to replace some of the adsorbed CO_2 molecules with CH_4 to form a mixed CO_2/CH_4 phase. We hypothesize that it is this enthalpy difference that leads to the CO_2/CH_4 selectivity observed in Co(bdp), and that this effect may extend to other metal–organic frameworks capable of expanding continuously from a nonporous evacuated structure to a large-pore structure that would not otherwise be expected to exhibit selective adsorption via size-exclusion.

CO_2/CH_4 Selectivity Under a CH_4-Rich Atmosphere. Although the adsorption of CO_2 in Co(bdp) is enthalpically favored over CH_4 for a ~50:50 ratio of the two gases, we wanted to probe whether the near-perfect selectivity persisted under a radically different gas ratio. To this end, the framework was exposed to equilibrium pressures of 3.7 bar CO_2 and 54.9 bar CH_4, representing a 6:94 molar ratio of CO_2:CH_4. Under these conditions, we found that although the material remains selective for CO_2 (adsorbing 8.5 mmol/g), a significant amount of CH_4 (2.1 mmol/g) is also adsorbed (Figure 3.2b). Thus, the calculated CO_2/CH_4 selectivity is reduced to 61 ± 4 under these conditions (see Supporting Information for selectivity calculations and a discussion of error). This result highlights that even if near-perfect selectivity persists beyond several phase changes in a flexible metal–organic framework, it is not correct to assume that it will persist for all equilibrium ratios for a given gas mixture. We note, however, that the measured multicomponent selectivity for CO_2 under CH_4-rich conditions is still significantly

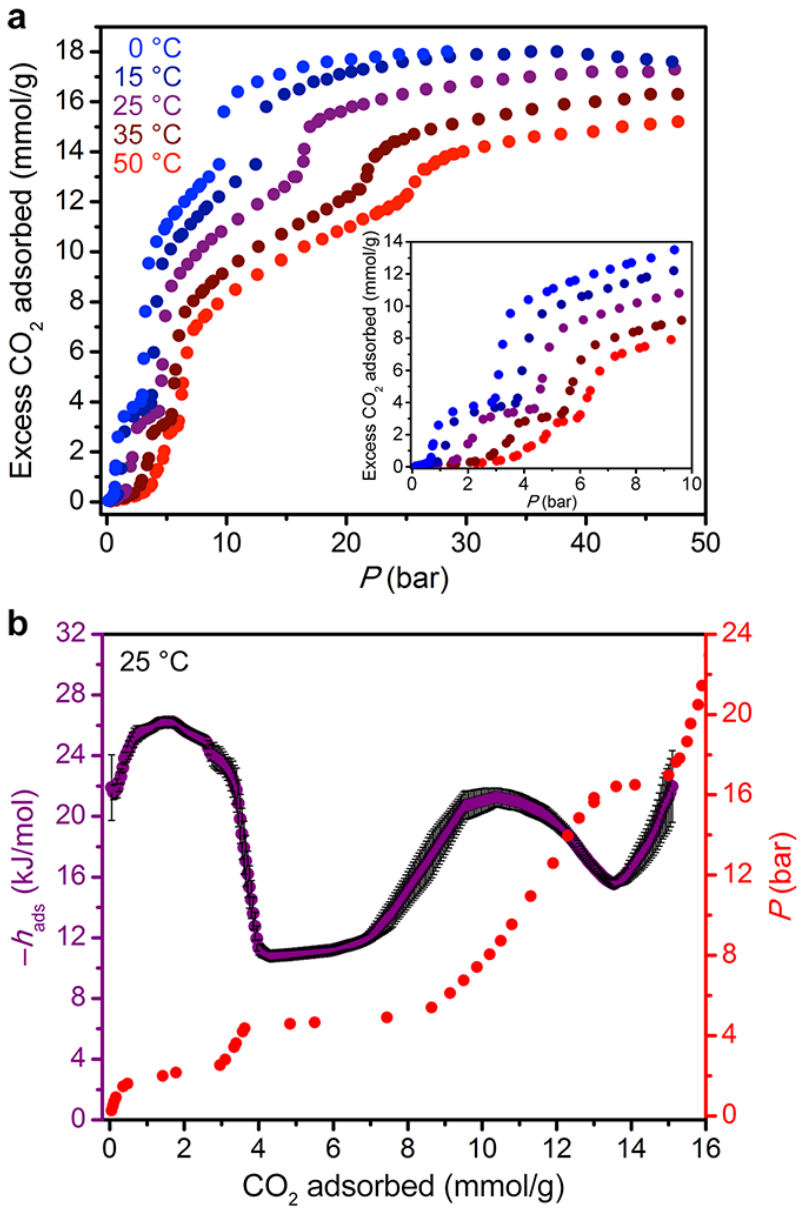

Figure 3.4. (a) Variable-temperature CO_2 adsorption data for Co(bdp). Minor changes in temperature move the pressure at which the CO_2-induced phase changes occur, offering a straightforward way to tailor the step pressure to a desired set of separation conditions. (b) Differential enthalpies (h_{ads}) of CO_2 adsorption in Co(bdp) are shown in purple (standard errors are shown as black bars) as a function of CO_2 loading. Local minima in $-h_{ads}$ correspond to regions in which Co(bdp) undergoes an endothermic structural expansion, which offsets some of the heat released upon CO_2 adsorption and provides intrinsic thermal management. The single-component CO_2 adsorption isotherm (red circles) is provided for comparison.

greater than the selectivity of 5.7 calculated at the corresponding pressures from the single-component adsorption isotherms (see the Supporting Information).

Tuning the Phase-Change Pressure. To supplement the equilibrium adsorption experiments described above, the separation ability of Co(bdp) was tested under dynamic breakthrough conditions. A 50:50 mixture of CO_2:CH_4 was flowed through a column of Co(bdp) at 7 bar and 22 °C to simulate the first data point of Figure 3.2a, and the results of the breakthrough experiment uphold the equilibrium findings at these conditions. The material adsorbs only CO_2, with CH_4 adsorption within error of zero (see the Supporting Information for calculations and experimental details). However, because the first CO_2-induced step in the 25 °C isotherm occurs at 2 bar (Figure 3.1b) and Co(bdp) adsorbs no CO_2 below this pressure, a 22 °C breakthrough experiment will always allow ~2 bar of CO_2 to slip through the column, as discussed previously for flexible adsorbents.[55] Thus, the pressure of the first CO_2-induced phase change makes Co(bdp) impractical for the production of pure CH_4 under these conditions, owing to the low purity of the outlet stream.

There are several straightforward ways to improve the purity of the outlet stream. First, as seen in Figure 3.4a, relatively minor changes in temperature have a dramatic effect on the step pressure; for example, by reducing the temperature from 25 °C to 12 °C, the CO_2 pressure necessary to induce a phase change is cut in half. Alternatively, we have shown previously that fluorination of the bdp^{2-} linker can lower the CH_4-induced step pressure, as fluorine disrupts intraframework π–π interactions that stabilize the collapsed phase.[39] Indeed, fluorination of the linker lowers the first CO_2-induced step pressure from ~2 bar to ~0.6 bar (Figure 3.5). Finally, the wider community has identified many other flexible metal–organic frameworks with a variety of step pressures under various gases,[7-9] and because our findings indicate that flexible frameworks can exhibit very high inherent selectivities under equilibrium conditions, further research into the multicomponent adsorption behavior of a diverse set of flexible frameworks may ultimately make it possible to choose an adsorbent with step pressures tailored to a given separation.

3.4. Conclusions

Using multicomponent equilibrium adsorption and *in situ* powder X-ray diffraction measurements, we have demonstrated that the flexible metal–organic framework Co(bdp) achieves high CO_2/CH_4 selectivity for a wide range of pressures via reversible CO_2 templating. At 7.2 bar of CO_2/CH_4 (corresponding to a CO_2 partial pressure of 3.6 bar), the diffraction results show that CO_2/CH_4 selectivity results from size-exclusion, as Co(bdp) adopts a phase with a pore aperture large enough to admit CO_2 but not CH_4. At higher pressures, Co(bdp) expands to phases with larger pores capable of admitting CH_4 molecules, but the enthalpic favorability of CO_2-clathrate formation drives the continued exclusion of CH_4. For a CO_2:CH_4 ratio of 6:94 heavily favoring CH_4, however, this exceptional selectivity is diminished, indicating the importance of using multicomponent equilibrium experiments across a wide range of conditions to achieve an accurate understanding of the gas separation performance of a structurally flexible

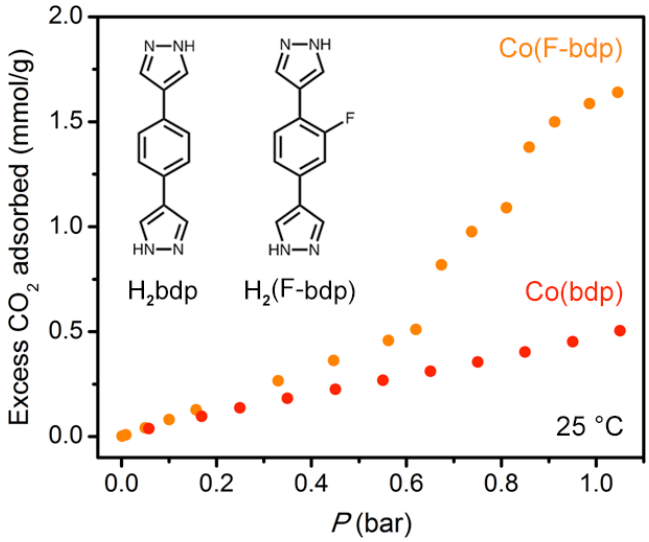

Figure 3.5. Low-pressure CO_2 adsorption isotherms for Co(bdp) and a fluorinated derivative, Co(F-bdp). Functionalization of the H_2bdp linker with a single fluorine atom shifts the first CO_2-induced step from ~2 bar to ~0.6 bar, providing a means of synthetic control over the adsorption and separation properties of the material.

material. Finally, single-component CO_2, CH_4, N_2, and H_2 adsorption isotherms collected for Co(bdp) suggest that this material may achieve high selectivities and capacities in other important gas separations, including CO_2 from N_2, CO_2 from H_2, CH_4 from N_2, and CH_4 from H_2. Importantly, as previously demonstrated for CH_4 storage applications,[39] adding substituents to the bdp^{2-} linkers in Co(bdp) provides a means of controlling the adsorption isotherm step pressure, which should allow these flexible adsorbents to be customized for specific separations.

3.5. Acknowledgements

First and foremost, I acknowledge my coauthors on this work, Tomče Runčevski, Julia Oktawiec, Jonathan E. Bachman, Rebecca L. Siegelman, Henry Jiang, Jarad A. Mason, Jacob D. Tarver, and Jeffrey R. Long. This research was supported by the Center for Gas Separations Relevant to Clean Energy Technologies, an Energy Frontier Research Center supported by the U.S. Department of Energy, Office of Science, Office of Basic Energy Sciences, under Award DE-SC0001015. Powder X-ray diffraction data were collected on the 17-BM-B Beamline at the Advanced Photon Source, a U.S. Department of Energy Office of Science User Facility operated by Argonne National Laboratory. Use of the Advanced Photon Source at Argonne National Laboratory was supported by the U.S. Department of Energy, Office of Science, Office of Basic Energy Sciences, under Contract No. DE-AC02-06CH11357. J.D.T. gratefully acknowledges research support from the U.S. Department of Energy, Office of Energy Efficiency and Renewable Energy, Fuel Cell Technologies Office, under Contract No. DE-AC36-08GO28308. I further thank the National Science Foundation for providing graduate fellowship support for M.K.T., J.O., and J.A.M.; Dr. Miguel I. Gonzalez, Dr. Matthew T. Kapelewski, and

Dr. C. Michael McGuirk for helpful discussions and experimental assistance; and Dr. Katie R. Meihaus for editorial assistance.

3.6. References

(1) Sholl, D. S.; Lively, R. P. *Nature* **2016,** *532,* 435.
(2) Zhang, Y.; Sunarso, J.; Liu, S.; Wang, R. *Int. J. Greenhouse Gas Control* **2013,** *12,* 84.
(3) Service, R. F. *Science* **2014,** *346,* 538.
(4) Rufford, T. E.; Smart, S; Watson, G. C. Y.; Graham, B. F.; Boxall, J.; Diniz da Costa; May, E. F. *J. Pet. Sci. Eng.* **2012,** *94-95,* 123.
(5) Li, J.-R.; Kuppler, R. J.; Zhou, H.-C. *Chem. Soc. Rev.* **2009,** *38,* 1477.
(6) Yu, J.; Xie, L.-H.; Li, J.-R.; Ma, Y.; Seminario, J. M; Balbuena, P. B. *Chem. Rev.* **2017,** *117,* 9674.
(7) Horike, S.; Shimomura, S.; Kitagawa, S. *Nat. Chem.* **2009,** *1,* 695.
(8) Schneemann, A.; Bon, V.; Schwedler, I; Senkovska, I.; Kaskel, S.; Fischer, R. A. *Chem. Soc. Rev.* **2014,** *43,* 6062.
(9) Elsaidi, S. K.; Mohamed, M. H.; Banerjee, D.; Thallapally, P. K. *Coord. Chem. Rev.* **2018,** *358,* 125.
(10) Thallapally, P. K.; Tian, J.; Kishan, M. R.; Fernandez, C. A.; Dalgarno, S. J.; McGrail, P. B.; Warren, J. E.; Atwood, J. L. *J. Am. Chem. Soc.* **2008,** *130,* 16842.
(11) Choi, H.-S.; Suh, M. P. *Angew. Chem. Int. Ed.* **2009,** *48,* 6865.
(12) Couck, S.; Denayer, J. F. M.; Baron, G. V.; Remy, T.; Gascon, J.; Kapteijn, F. *J. Am. Chem. Soc* **2009,** *131,* 6326.
(13) Hamon, L.; Llewellyn, P. L.; Devic, T.; Ghoufi, A.; Clet, G.; Guillerm, V.; Pirngruber,G. D.; Maurin, G.; Serre, C.; Driver, G.; van Beek, W.; Jolimaître, E.; Vimont, A.; Daturi, M; Férey, G. *J. Am. Chem. Soc.* **2009,** *131,* 17490.
(14) Kanoh, H.; Kondo, A.; Noguchi, H.; Kajiro, H.; Tohdoh, A.; Hattori, Y.; Xu, W.-C.; Inoue, M.; Sugiura, T.; Morita, K.; Tanaka, H.; Ohba, T.; Kaneko, K. *J. Colloid Interface Sci.* **2009,** *334,* 1.
(15) Fernandez, C. A.; Thallapally, P. K.; Motkuri, R. K.; Nune, S. K.; Sumrak, J. C.; Tian, J.; Liu, J. *Cryst. Growth Des.* **2010**, *10*, 1037.
(16) Inubushi, Y.; Horike, S.; Fukushima, T.; Akiyama, G.; Matsuda, R.; Kitagawa, S. *Chem. Commun.* **2010**, *46*, 9229.
(17) Kishan, M. R.; Tian, J.; Thallapally, P. K.; Fernandez, C. A.; Dalgarno, S. J.; Warren, J. E.; McGrail, B. P.; Atwood, J. L. *Chem. Commun.,* **2010**, *46*, 538.
(18) Nakagawa, K.; Tanaka, D.; Horike, S.; Shimomura, S.; Higuchi, M.; Kitagawa, S. *Chem. Commun.* **2010,** *46,* 4258.
(19) Wu, H.; Reali, R. S.; Smith, D. A.; Trachtenberg, M. C.; Li, J. *Chem. Eur. J.* **2010,** *16,* 13951.
(20) Zhang, J.; Wu, H.; Emge, T. J.; Li, J. *Chem. Commun.* **2010,** *46,* 9152.
(21) Kauffman, K. L.; Culp, J. F.; Allen, A. J.; Espinal, L.; Wong-Ng, W.; Brown, T. D.; Goodman, A.; Bernardo, M. P.; Pancoast, R. J.; Chirdon, D.; Matranga, C. *Angew. Chem. Int. Ed.* **2011,** *50*, 10888.

(22) Xiang, S.-C.; Zhang, Z.; Zhao, C.-G.; Hong, K.; Zhao, X.; Ding, D.-R.; Xie, M.-H.; Wu, C.-D.; Das, M. C.; Gill, R.; Thomas, K. M.; Chen, B. *Nat. Comm.* **2010,** *2*, 204.
(23) Horike, S.; Inubushi, Y.; Hori, T.; Fukushima, T.; Kitagawa, S. *Chem. Sci.* **2012**, *3*, 116.
(24) Liao, P.Q.; Zhou, D.-D.; Zhu, A.-X.; Jiang, L.; Lin, R.-B.; Zhang, J.-P.; Chen, X.-M. *J. Am. Chem. Soc.* **2012**, *134*, 17380.
(25) Nijem, N.; Wu, H.; Canepa, P.; Marti, A.; Balkus, K. J., Jr.; Thonhauser, T.; Li, J.; Chabal, Y. J. *J. Am. Chem. Soc.* **2012,** *134*, 15201.
(26) Yuan, B.; Ma, D.; Wang, X.; Li, Z.; Li, Y.; Liu, H.; He, D. *Chem. Commun.* **2012,** *48,* 1135.
(27) Lin, Z.-J.; Huang, Y.-B.; Liu, T.-F.; Li, X.-Y.; Cao, R. *Inorg. Chem.* **2013,** *52,* 3127.
(28) Sato, H.; Kosaka, W.; Matsuda, R.; Hori, A.; Hijikata, Y.; Belosludov, R. V.; Sakaki, S.; Takata, M.; Kitagawa, S. *Science* **2014,** *343,* 167.
(29) Chen, D.-M.; Zhang, X.-P.; Shi, W.; Cheng, P. *Inorg. Chem.* **2015,** *54,* 5512.
(30) Li, L.; Wang, Y.; Yang, J.; Wang, X.; Li, J. *J. Mater. Chem. A.* **2015,** *3,* 22574.
(31) Foo, M. L.; Matsuda, R.; Hijikata, Y.; Krishna, R.; Sato, H.; Horike, S.; Hori, A.; Duan, J.; Sato, Y.; Kubota, Y.; Takata, M.; Kitagawa, S. *J. Am. Chem. Soc.* **2016**, *138*, 3022.
(32) Zhao, Y.-P.; Li, Y.; Cui, C.-Y.; Xiao, Y.; Li, R.; Wang, S.-H.; Zheng, F.-K.; Guo, G.-C. *Inorg. Chem.* **2016,** *55*, 7335.
(33) Carrington, E. J.; McAnally, C. A.; Fletcher, A. J.; Thompson, S. P.; Warren, M.; Brammer, L. *Nat. Chem.* **2017,** *9,* 882.
(34) Hiraide, S.; Tanaka, H.; Ishikawa, N.; Miyahara, M. T. *ACS Appl. Mater. Interfaces* **2017,** *9,* 41066.
(35) Wang, H.; Cao, H.; Zheng, J.-J.; Mathew, S.; Hosono, H.; Zhou, B.; Lyu, H.; Kusaka, S.; Jin, W.; Kitagawa, S.; Duan, J. *Chem. Eur. J.* **2018,** *24,* 6412.
(36) Choi, H. J.; Dincă, M.; Long, J. R. *J. Am. Chem. Soc.* **2008,** *130,* 7848.
(37) Herm, Z. R.; Swisher, J. A.; Smit, B.; Krishna, R.; Long, J. R. *J. Am Chem. Soc.* **2011,** *133,* 5664.
(38) Mason, J. A.; Oktawiec, J.; Taylor, M. K.; Hudson, M. R.; Rodriguez, J.; Bachman, J. E.; Gonzalez, M. I.; Cervellino, A.; Guagliardi, A.; Brown, C. M.; Llewellyn, P. L.; Masciocchi, N.; Long, J. R. *Nature* **2015**, *527,* 357.
(39) Taylor, M. K.; Runčevski, T.; Oktawiec, J.; Gonzalez, M. I.; Siegelman, R. L.; Mason, J. A.; Ye, J.; Brown, C. M.; Long, J. R. *J. Am. Chem. Soc.* **2016,** *138,* 15019.
(40) Mason, J. A.; Veenstra, M.; Long, J. R. *Chem. Sci.* **2014,** *5,* 32.
(41) Lemmon, E. W.; Huber, M. L.; McLinden, M. O. *NIST Standard Reference Database 23: Reference Fluid Thermodynamic and Transport Properties REFPROP Version 8.0;* National Institute of Standards and Technology: Gaithersburg, MD, 2007.
(42) Coudert, F.-X.; Jeffroy, M.; Fuchs, A. H.; Boutin, A.; Mellot-Draznieks, C. *JACS*, **2008**, *130*, 14294.
(43) Saha, D.; Grappe, H. A.; Chakraborty, A.; Orkoulas, G. *Chem. Rev.* **2016,** *116,* 11436.
(44) Saeidi, S.; Fazlollahi, F.; Najari, S.; Iranshahi, D.; Klemeš, J. J.; Baxter, L. L. *J. Ind. Eng. Chem.* **2017,** *49,* 1.
(45) Abatzoglou, N.; Boivin, S. *Biofuels, Bioprod. Bioref.* **2009,** *3,* 42.
(46) Zhang, Z.; Yao, Z.-Z.; Xiang, S.; Chen, B. *Energy Environ. Sci.* **2014,** *7,* 2868.

(47) Myers, A. L.; Prausnitz, J. M. *AIChE J.* **1965,** *11,* 121.
(48) Coudert, F.-X.; Mellot-Draznieks, C.; Fuchs, A. H.; Boutin, A. *J. Am. Chem. Soc.* **2009,** *131,* 11329.
(49) Sircar, S. *Ind. Eng. Chem. Res.* **2006**, *45*, 5435.
(50) Broom, D. P.; Thomas, K. M. *MRS Bull.* **2013**, *38*, 412.
(51) Rajendran, A.; Kariwala, V.; Farooq, S. *Chem. Eng. Sci.* **2008**, *63*, 2696.
(52) Mason, J. A.; McDonald, T. M.; Bae, T.-H.; Bachman, J. E.; Sumida, K.; Dutton, J. J.; Kaye, S. S.; Long, J. R. *J. Am. Chem. Soc.* **2015,** *137,* 4787.
(53) Li, B.; Cui, X.; O' Nolan, D.; Wen, H.-M.; Jiang, M.; Krishna, R.; Wu, H.; Lin, R.-B.; Chen, Y.-S.; Yuan, D.; Xing, H.; Zhou, W.; Ren, Q.; Qian, G.; Zaworotko, M. J.; Chen, B. *Adv. Mater.* **2017,** *29,* 1704210.
(54) Colombo, V.; Montoro, C.; Maspero, A.; Palmisano, G.; Masciocchi, N.; Galli, S.; Barea, E.; Navarro, J. A. R. *J. Am. Chem. Soc.* **2012,** *134,* 12830.
(55) Sotomayor, F. J.; Lastoskie, C. M. *Langmuir*, **2017,** *33,* 11670.

3.7. Supporting Information

General Information. Anhydrous *N,N*-dimethylformamide (DMF) and anhydrous dichloromethane (CH_2Cl_2) were obtained from a JC Meyer solvent system. All other reagents were obtained from commercial vendors and used without further purification. Ultra-high purity (≥99.998% purity) dinitrogen, helium, carbon dioxide, methane, and dihydrogen were used for all adsorption measurements.

Synthesis of Co(bdp). Co(bdp) was prepared according to a previously published procedure.[1] Specifically, a 100 mL solvent bomb was charged with a magnetic stir bar, $Co(CF_3SO_3)_2$ (0.72 g, 2.0 mmol, 1.1 equiv), H_2bdp (1.9 mmol, 1.0 equiv),[2] and 10 mL of *N,N*-diethylformamide (DEF). The mixture was degassed using five freeze-pump-thaw cycles and then sealed by closing the stopcock of the solvent bomb while the frozen reaction mixture remained under vacuum. The solvent bomb was then heated at 160 °C for 3 d to afford a purple microcrystalline solid. Upon completion of the reaction, the solvent bomb was backfilled with Ar, the supernatant was removed under positive Ar pressure and discarded, and 80 mL of anhydrous *N,N*-dimethylformamide (DMF) was added to the solid product under an Ar atmosphere. The solvent bomb was then sealed under Ar and heated to 110 °C overnight. This solvent-exchange procedure was performed once daily for 7 d to completely remove unreacted starting material from the pores. Subsequently, the DMF was replaced with anhydrous CH_2Cl_2 following the same procedure but without heating. These CH_2Cl_2 exchanges were performed once daily for 3 d to allow activation from a lower-boiling solvent. To activate the material, the CH_2Cl_2 was evaporated under positive Ar pressure until 25 mL of solution remained. The resultant slurry was transferred to a 100 mL Schlenk flask under inert atmosphere, and the CH_2Cl_2 was evaporated over the course of 1 h under a flow of Ar at room temperature. The resultant solid was dried under a flow of Ar at 160 °C for 6 h and then placed under dynamic vacuum at 160 °C overnight. The activated solid was immediately transferred to a glovebox and handled under a dinitrogen atmosphere for all further experiments.

Synthesis of H_2(F-bdp). H_2(F-bdp) was prepared according to a previously published procedure[3] *via* a Suzuki-Miyaura coupling.[4] Specifically, 1,4-dibromo-2-fluorobenzene (3.03 g, 11.9 mmol, 1.0 equiv), 1-(2-tetrahydropyranyl)-1H-pyrazole-4-boronic acid pinacol ester (8.30 g, 29.8 mmol, 2.5 equiv), and K_3PO_4 (12.7 g, 60 mmol, 5 equiv) were suspended in toluene (24 mL) in a 40-mL glass scintillation vial with a magnetic stir bar and sparged with Ar for 10 minutes. XPhos Pd G2 (1.74 g, 2.4 mmol, 0.2 equiv) was added quickly in air, and vial was briefly purged with Ar, sealed with a PTFE-lined cap, and heated to 110 °C while stirring for 2 days. Upon completion, the reaction mixture was cooled to room temperature, concentrated under reduced pressure, and diluted with 250 mL of diethyl ether. The ether layer was washed 5 times with 250 mL of saturated aqueous $NaHCO_3$ solution, dried over $MgSO_4$, and concentrated under reduced pressure to yield a yellow oil, which was used in the subsequent reaction without additional purification. The crude ligand was dissolved in 90 mL of methanol in a 250-mL round-bottom flask with a magnetic stir bar, 18 mL of concentrated aqueous HCl was added, and the reaction mixture was stirred at 50 °C for 2 h, during which time a yellow precipitate formed. The reaction mixture was filtered, and the filtrate was suspended in water and neutralized with $NaHCO_3$. The precipitate was again isolated by filtration, washed with water, and dried *in vacuo* to yield **H_2(F-bdp)** (1.31 g, 5.8 mmol, 49%) as a beige powder. ^{1}H NMR (400 MHz, DMSO-d_6): δ 8.13 (s, 2H), 8.05 (s, 2H) 7.70 (t, J = 8.2 Hz, 1H), 7.52 (dd, J = 12.8, 1.8 Hz, 1H), 7.46 (dd, J = 8.1, 1.8 Hz, 1H) ppm; ^{13}C NMR (101 MHz, DMSO-d_6): δ 160.65, 158.22, 133.04 (d, J = 9.3 Hz), 128.58 (d, J = 5.0 Hz), 121.77, 120.55, 115.15, 112.79, 112.56 ppm; ^{19}F NMR (376 MHz, DMSO-d_6): δ -114.70 ppm. Note that the ^{1}H NMR signals from the hydrogen atoms bonded to the pyrazole nitrogen atoms are too broad to be visible. Anal. Calcd. for $C_{12}H_9FN_4$: C, 63.15, H, 3.97, N, 24.55; found: C, 61.85, H, 3.99, N, 23.64. IR: 3137(w), 3079 (w), 2935 (m), 2848 (m), 1624 (w), 1587 (m), 1473 (m), 1452 (m), 1374 (m), 1271 (w), 1252 (w), 1230 (w), 1200 (w), 1157 (m), 1111(m), 1038(m), 984 (w), 961 (m), 950 (m), 876 (m), 857 (s), 814 (s), 750 (m), 724 (m), 669 (w), 661 (w), 594 (s), 556 (m), 533 (m), 520 (m), 508 (m), 498 (w), 483 (m), 471 (m), 459 (s), 452 (m) cm^{-1}.

Synthesis of Co(F-bdp). Co(F-bdp) was prepared according to a previously published procedure.[3] Specifically, a 100-mL solvent bomb was charged with a magnetic stirring bar, $Co(CF_3SO_3)_2$ (0.75 g, 2.1 mmol, 1.0 equiv), H_2(F-bdp) (0.48 g, 2.1 mmol, 1.0 equiv), and DMF (10.4 mL). The reaction mixture was degassed by the freeze–pump–thaw method for 5 cycles, then sealed by closing the stopcock of the solvent bomb while the frozen reaction mixture remained under vacuum. The solvent bomb was then heated at 160 °C for 3 days to afford a purple microcrystalline solid. (To obtain crystals suitable for single-crystal X-ray diffraction, the magnetic stir bar was omitted from reaction flask while maintaining all other conditions constant.) Upon completion, the solvent bomb was backfilled with Ar, the supernatant was removed under positive Ar pressure and discarded, and 80 mL of anhydrous DMF was added to the solid product while maintaining under inert atmosphere. The solvent bomb was then sealed under Ar and heated to 110 °C overnight. This solvent-exchange procedure was performed once daily for 7 days to completely remove unreacted starting material from the pores. Subsequently, the DMF was replaced with anhydrous CH_2Cl_2 following the same procedure but without heating; these CH_2Cl_2 exchanges were performed once daily for 3 days to allow activation from a lower-boiling solvent. To activate the material, the

CH_2Cl_2 was removed under positive Ar pressure until 25 mL of solution remained. The resultant slurry was transferred to a 100-mL Schlenk flask under inert atmosphere, and the CH_2Cl_2 was evaporated by flowing Ar at room temperature for 1 h. The resultant solid was dried by flowing Ar at 160 °C for 6 h, then placed under dynamic vacuum at 160 °C overnight to yield **Co(F-bdp)** (0.153 g, 0.5 mmol, 25%). The activated solid was immediately transferred to a glovebox and handled under a dinitrogen atmosphere for all further experiments. Anal. Calcd. for $C_{12}H_9CoFN_4$: C, 50.19, H, 3.16, N, 19.51; found: C, 47.39, H, 2.29, N, 18.29. IR: 1575 (m), 1490 (w), 1442 (w), 1374 (m), 1356 (m), 1331 (m), 1254 (m), 1236 (m), 1198 (w), 1170 (s), 1108 (m), 1079 (w), 1050 (s), 998 (m), 989 (m), 953 (s), 854 (s), 816 (s), 720 (w), 660 (m), 652 (m), 606 (s), 559 (s), 481 (s), 467 (s) cm^{-1}.

Background single-component adsorption corrections

Background adsorption isotherms were measured using an empty sample holder for H_2, N_2, and CH_4 at all temperatures for which isotherms are reported herein, and all of these background isotherms showed negligible background adsorption. However, when adsorption isotherms were measured for CO_2 using an empty sample holder at the corresponding temperatures, significant background adsorption was observed. This background CO_2 adsorption was fit using 6th-order polynomial functions (Figures 3.S1-3.S5). These functions were then used to correct the raw CO_2 adsorption data, by subtracting the background adsorption from the measured adsorption at each observed pressure.

Complete single-component adsorption and desorption data

The experimental procedure for single-component adsorption measurements is provided in the main text. Variable temperature isotherms for H_2, N_2, and CO_2 adsorption in Co(bdp) are shown in Figures 3.S6-3.S16. Variable temperature isotherms for CH_4 adsorption in Co(bdp) have already been reported[1], but CH_4 adsorption was measured again at 25 °C on the same Co(bdp) sample used throughout this work to verify reproducibility and sample quality, and this CH_4 adsorption isotherm is shown in Figure 3.S17.

Calculation of h_{ads} for CO_2 in Co(bdp)

To obtain the differential enthalpies (h_{ads}) of CO_2 adsorption, the high-pressure CO_2 adsorption isotherms at 0, 12, 25, 40, and 50 °C were first fit with linear splines (Figure 3.S18). Using the isotherm fits, the exact pressures (P) corresponding to specific CO_2 loadings (n) were determined at each temperature (T). The Clausius−Clapeyron relationship was then used to calculate the differential enthalpies of adsorption (h_{ads}) based on the slopes of the linear trendlines fit to ln P vs. $1/T$ at each value of n in Eq. S1 below. Standard errors were calculated from the deviations of the best-fit lines.

$$(\ln P)_n = \frac{h_{ads}}{RT} + C \qquad \textit{Eq. S1}$$

Multicomponent equilibrium adsorption: Partial CO_2 and CH_4 pressures of adsorbed phase and headspace

A complete description of the experimental procedure is provided in the main text. In summary, a high-pressure adsorption instrument (HPVA-II-100) and a mass spectrometer (MKS Microvision 2) were used in tandem to analyze the adsorbed gas after Co(bdp) equilibrated under a known mixture of CO_2 and CH_4. An explanation of the data analysis is provided below.

The raw data provided by the HPVA-II-100 are:

- Pressure of dosing manifold + sample holder after equilibration: $\mathbf{P_{eq}}$ (bar)
- Temperature of the manifold ($\mathbf{T_m}$) and temperature of the sample ($\mathbf{T_s}$)

These data are used by the HPVA-II-100 software to calculate the following experimental values:

- Volume of gas in dosing manifold before opening to sample: $\mathbf{V_{dosed}}$ (cc STP)
- Volume of gas adsorbed onto sample after equilibration: $\mathbf{V_{ads}}$ (cc STP)

The raw data provided by the MKS Microvision 2 are:

- Mole fraction CO_2 relative to all gas in the sample holder after equilibration: $\mathbf{x_{CO2}}$
- Mole fraction CH_4 relative to all gas in the sample holder after equilibration: $\mathbf{x_{CH4}}$

Known experimental variables are:

- Sample mass: **m** (g)
- Mole fraction CO_2 dosed: $\mathbf{y_{CO2}}$
- Mole fraction CH_4 dosed: $\mathbf{y_{CH4}}$
- Free space of sample holder: $\mathbf{V_{FS}}$ (cc STP)

The raw data provided by the HPVA-II-100 can be converted to moles using the following equations:

$$\frac{\mathbf{V_{dosed}}}{2.24 \times 10^4 \text{ cc/mol}} = \mathbf{n_{dosed}} \qquad \textit{Eq. S2}$$

$$\frac{\mathbf{P_{eq}} \times \mathbf{V_{FS}}}{(8.314 \times 10^{-5} \text{ cc bar/K mol}) \times \mathbf{T_S}} = \mathbf{n_{headspace}} \qquad \textit{Eq. S3}$$

$$\frac{\mathbf{V_{ads}}}{2.24 \times 10^4 \text{ cc/mol}} = \mathbf{n_{ads}} \qquad \textit{Eq. S4}$$

Figure 3.S19 shows a schematic of the multicomponent adsorption experimental set-up, illustrating $\mathbf{n_{dosed}}$, $\mathbf{n_{headspace}}$, and $\mathbf{n_{ads}}$.

The mole fractions given by the MKS Microvision 2 ($\mathbf{x_{CO2}}$ and $\mathbf{x_{CH4}}$) can be converted to moles ($\mathbf{n_{CO2}}$ and $\mathbf{n_{CH4}}$) as follows.

$\mathbf{x_{CO2}}$ is defined as moles CO_2 divided by moles total gas:

$$\mathbf{x_{CO2}} = \frac{\mathbf{n_{CO2}}}{\mathbf{n_{CO2}} + \mathbf{n_{CH4}}} \qquad \textit{Eq. S5}$$

$\mathbf{x_{CH4}}$ is related to $\mathbf{x_{CO2}}$ according to:

$$\mathbf{x_{CH4}} = 1 - \mathbf{x_{CO2}} \qquad \textit{Eq. S6}$$

The ratio of the mole fractions is equal to the ratio of the molar values:

$$\frac{1 - \mathbf{x_{CO2}}}{\mathbf{x_{CO2}}} = \frac{\mathbf{n_{CH4}}}{\mathbf{n_{CO2}}} \qquad \textit{Eq. S7}$$

We can define this ratio as a constant *k*:

$$\frac{1 - \mathbf{x_{CO2}}}{\mathbf{x_{CO2}}} = k \qquad \textit{Eq. S8}$$

Substituting *k* into Equation S7 gives:

$$k \times \mathbf{n_{CO2}} = \mathbf{n_{CH4}} \qquad \textit{Eq. S9}$$

The total moles of gas are given by the HPVA-II-100 data:

$$\mathbf{n_{CO2}} + \mathbf{n_{CH4}} = \mathbf{n_{headspace}} + \mathbf{n_{ads}} \qquad \textit{Eq. 10}$$

Substituting Equation S9 for $\mathbf{n_{CH4}}$ into Equation S10 gives:

$$\mathbf{n_{CO2}} + (k \times \mathbf{n_{CO2}}) = \mathbf{n_{headspace}} + \mathbf{n_{ads}} \qquad \textit{Eq. S11}$$

Simplifying Equation S11 allows us to solve for $\mathbf{n_{CO2}}$ numerically:

$$\mathbf{n_{CO2}} = \frac{\mathbf{n_{headspace}} + \mathbf{n_{ads}}}{1 + k} \qquad \textit{Eq. S12}$$

Using the value for $\mathbf{n_{CO2}}$ found in Equation S12, Equation S9 can be used to solve numerically for $\mathbf{n_{CH4}}$. The above values can then be used to determine the moles CO_2 and moles CH_4 adsorbed onto Co(bdp) as follows.

$\mathbf{n_{CO2manifold}}$ is defined as the moles CO_2 in the dosing manifold after equilibration:

$$(\mathbf{n_{dosed}} \times \mathbf{y_{CO2}}) - \mathbf{n_{CO2}} = \mathbf{n_{CO2manifold}} \qquad \textit{Eq. S13}$$

$\mathbf{n_{CH4manifold}}$ is defined as the moles CH_4 in the dosing manifold after equilibration:

$$(\mathbf{n_{dosed}} \times \mathbf{y_{CH4}}) - \mathbf{n_{CH4}} = \mathbf{n_{CH4manifold}} \qquad \textit{Eq. S14}$$

$\mathbf{x_{CO2manifold}}$ is defined as the mole fraction of CO_2 in the dosing manifold after equilibration.

$$\frac{\mathbf{n_{CO2manifold}}}{\mathbf{n_{CO2manifold}} + \mathbf{n_{CH4manifold}}} = \mathbf{x_{CO2manifold}} \qquad \textit{Eq. S15}$$

$\mathbf{x_{CO2headspace}}$ is defined as the mole fraction of CO_2 in the headspace of the sample after equilibration, which is necessarily equal to $\mathbf{x_{CO2manifold}}$.

$$\mathbf{x_{CO2manifold}} = \mathbf{x_{CO2headspace}} \qquad \textit{Eq. S16}$$

$\mathbf{x_{CO2headspace}}$ can be converted to moles:

$$\mathbf{x_{CO2headspace}} \times \mathbf{n_{headspace}} = \mathbf{n_{CO2headspace}} \qquad \textit{Eq. S17}$$

$\mathbf{n_{CO2headspace}}$ can be used to find $\mathbf{n_{CH4headspace}}$:

$$\mathbf{n_{headspace}} - \mathbf{n_{CO2headspace}} = \mathbf{n_{CH4headspace}} \qquad \textit{Eq. S18}$$

By substracting the moles CO_2 in the manifold and headspace from the moles CO_2 dosed, we can calculate the moles CO_2 adsorbed onto Co(bdp) ($\mathbf{n_{CO2ads}}$):

$$(\mathbf{n_{dosed}} \times \mathbf{y_{CO2}}) - (\mathbf{n_{CO2manifold}} + \mathbf{n_{CO2headspace}}) = \mathbf{n_{CO2ads}} \qquad \textit{Eq. S19}$$

By substracting the moles CH_4 in the manifold and headspace from the moles CH_4 dosed, we can calculate the moles CH_4 adsorbed onto Co(bdp) ($\mathbf{n_{CH4ads}}$):

$$(\mathbf{n_{dosed}} \times \mathbf{y_{CH4}}) - (\mathbf{n_{CH4manifold}} + \mathbf{n_{CH4headspace}}) = \mathbf{n_{CH4ads}} \qquad \textit{Eq. S20}$$

The partial CO_2 pressure of the headspace at equilibrium can be calculated as follows:

$$\mathbf{x_{CO2headspace}} \times \mathbf{P_{eq}} = \mathbf{P_{CO2}} \qquad \textit{Eq. S21}$$

The partial CH4 pressure of the headspace at equilibrium can be calculated as follows:

$$(1 - \mathbf{x_{CO2headspace}}) \times \mathbf{P_{eq}} = \mathbf{P_{CH4}} \qquad \textit{Eq. S22}$$

CO_2/CH_4 selectivity calculations

To determine the CO_2/CH_4 selectivity ($\boldsymbol{\alpha}$) of Co(bdp) under conditions in which a significant amount of CH_4 was adsorbed, the following expression was used:

$$\boldsymbol{\alpha} = \frac{\frac{\mathbf{n_{CO2ads}}}{\mathbf{n_{CH4ads}}}}{\frac{\mathbf{n_{CO2headspace}}}{\mathbf{n_{CH4headspace}}}} \qquad \textit{Eq. S23}$$

For comparison to the experimentally-determined selectivity value of 61 ± 4 discussed in the main text, the theoretical CO_2/CH_4 selectivity under CH_4-rich conditions was calculated from single-component CO_2 and CH_4 adsorption isotherms. The data points used from each adsorption isotherm were (3.62 bar CO_2, 3.39 mmol CO_2/g) and 55.64 bar CH_4, 9.15 mmol CH_4/g), respectively. Plugging these values into Eq. S23 yields a CO_2/CH_4 selectivity of 5.7, significantly smaller than the selectivity determined under multicomponent equilibrium conditions. This discrepancy further highlights the importance of using multicomponent equilibrium measurements to study gas separations in flexible metal–organic frameworks.

Multicomponent compressibility factors

A compressibility factor is a correction used to describe the extent to which a gas deviates from ideal gas behavior, as shown in Equation S24.[5]

$$\mathrm{Z} = \frac{\mathrm{PV}}{\mathrm{RT}} \qquad \textit{Eq. S24}$$

It is necessary to use compressibility factors in the data analysis of volumetric adsorption experiments, which rely on the change in volume of a gas to determine the amount adsorbed by a sample. The compressibility factor of a certain pure gas or gas mixture can be obtained from the NIST REFPROP database[6] for a given pressure and temperature. In all single-component adsorption experiments reported herein, the appropriate compressibility factors were used by the HPVA-II-100 software to calculate the volume of that gas adsorbed by the sample.

In the case of multicomponent adsorption experiments, the starting ratio of components is known and can be used to obtain the corresponding compressibility factor from the NIST REFPROP database.[6] However, the final ratio of components in the headspace (after equilibration with the sample) is not known, because the sample may show selectivity for one component over the other. Our experimental set-up made it necessary to choose equilibrium compressibility factors without knowing the equilibrium

composition of the headspace, because the determination of this composition via the mass spectrometry data requires knowledge of the total amount of gas adsorbed (See Part I of the Multicomponent Adsorption Data Analysis section of the Supporting Information). Therefore, we made the conservative estimate that Co(bdp) would show no selectivity for CO_2 or CH_4, and we used compressibility factors corresponding to the starting ratio of components for all steps of the multicomponent adsorption calculations performed by the HPVA-II-100 software, both before and after equilibration.

To verify that this choice of compressibility factors is valid, we performed the adsorption calculations for the same mixed gas experiment three times, using three different assumptions:

1) That Co(bdp) shows no CO_2 or CH_4 selectivity, leaving the equilibrium headspace composition equal to the starting headspace composition
2) That Co(bdp) shows perfect CO_2 selectivity and adsorbs only CO_2, leaving the equilibrium headspace enriched in CH_4 relative to the starting headspace composition
3) That Co(bdp) shows perfect CH_4 selectivity and adsorbs only CH_4, leaving the equilibrium headspace enriched in CO_2 relative to the starting headspace composition

This analysis was performed on the highest-pressure data point of Figure 3.2, in which Co(bdp) was dosed with a 50:50 mixture of CO_2:CH_4. To perform adsorption calculations based on Assumption 1, equilibrium compressibility factors were used that correspond to a 50:50 mixture of CO_2:CH_4 (since the starting ratio is unchanged in this scenario). These calculations yield a total adsorption value of **11.1 mmol/g**, which is shown in Figure 3.2.

To perform adsorption calculations based on Assumption 2, we estimated the theoretical maximum CO_2 capacity at this CO_2 partial pressure using the pure CO_2 isotherm shown in Figure 3.1b. In the mixed-gas experiment in question, Co(bdp) equilibrated under 25.25 bar of a 50:50 mixture of CO_2:CH_4, which corresponds to a partial CO_2 pressure of 12.63 bar. At this point (12.63 bar) on the pure CO_2 isotherm, Co(bdp) adsorbs 10.2 mmol/g of CO_2. If Co(bdp) were to exhibit this same CO_2 capacity in the mixed-gas experiment, it would result in an equilibrium headspace CO_2:CH_4 ratio of 44:56. This ratio was used to obtain equilibrium compressibility factors, which yield a total adsorption value of **11.2 mmol/g**. This value (which assumes perfect CO_2 selectivity) is only 1% greater than the value obtained using the conservative Assumption 1 (which assumes *no* selectivity), indicating that our choice to use Assumption 1 to determine equilibrium compressibility factors is valid and that variations in the equilibrium compressibility factors do not distort the data.

We also performed adsorption calculations based on Assumption 3. This assumption is the least plausible, as it assumes Co(bdp) will adsorb only CH_4 and not CO_2, even though Co(bdp) is not even porous at the corresponding point on the pure CH_4 isotherm (Figure 3.1). Indeed, the assumption that Co(bdp) is perfectly CH_4 selective is incompatible with our body of experimental evidence. However, for the sake of completeness, we obtained compressibility factors using the assumption that Co(bdp) adsorbed 10.2 mmol CH_4/g (the same amount of gas as in Assumption 2). This

hypothetical CH_4 capacity would result in an equilibrium headspace CO_2:CH_4 ratio of 56:44, and the corresponding compressibility factors yield a total adsorption value of **10.2 mmol/g**. This value is only 7% less than the value obtained using Assumption 1, which again upholds the validity of our chosen equilibrium compressibility factors.

Error for 6:94 CO_2:CH_4 experiment

To verify the reproducibility of our experimental design, we repeated the 6:94 CO_2:CH_4 multicomponent adsorption experiment with the same target dosing pressure, and obtained a very similar result in terms of total mixed-gas adsorbed, as shown by the diamonds in Figure 3.S20. For each of the 6:94 CO_2:CH_4 experiments, we also analyzed the gas mixture twice by mass spectrometry, and we used these results to calculate a standard error for each experiment (Figure 3.S21). Although we did not perform multiple mass spectrometry and/or adsorption trials for all of the gas mixtures reported in Figure 3.2, the error bars shown in Figure 3.S21 give a general picture of the error associated with the multicomponent equilibrium measurements.

Powder X-ray Diffraction

The experimental conditions of powder X-ray diffraction data collection are provided in the main text. The crystal structure analyses (indexing, solution and refinement) were performed with the program TOPAS 4.1.[7] Pattern indexing of the powder X-ray diffraction pattern of evacuated Co(bdp), accomplished *via* the the singular value decomposition method,[8] indicated a unit cell similar to that previously published for the evacuated phase of Co(bdp).[1] When the space group was assigned as C2/c and Pawley refinement attempted using the data, the precise unit cell lattice parameters matched very closely to reported values. In addition, Rietveld refinement using the published structure of evacuated Co(bdp) gave an excellent fit to the experimental data, as shown in Figure 3.S22, confirming that the evacuated Co(bdp) sample used in this study is isostructural to the published model. Figures of merit are presented in Table 3.S1.

After dosing to 3.6 bar of carbon dioxide, the sample adopted the structure of the first CO_2-expanded phase, which remained unchanged upon further dosing to 5.2 bar as evidenced by absence of changes in the collected scattered X-ray intensity (see Figure 3.3a). This powder diffraction pattern was selected for crystal structure solution and refinement. The pattern indexing was done with the singular value decomposition method,[8] resulting in a monoclinic unit cell. Based on the observed reflections, the space group was assumed to be *C*2/*c*, which was later confirmed by the Rietveld refinement. A Pawley fit[9] determined precise unit cell lattice and peak profile parameters, which were used for the crystal structure solution.

The crystal structure of the first CO_2-expanded phase was solved by the global optimization method of simulated annealing (SA) in real space.[10] Considering the *C*2/*c* space group symmetry and the unit cell parameters, one cobalt atom was placed at a special position with multiplicity of 4, where the *x* and *z* fractional coordinates were set to 0 and 1/4, respectively; whereas the *y* fractional coordinate was set as a variable. One half of the ligand was described as a rigid body in a *z* matrix notation (Figure 3.S23), and the other half was created by a symmetry operation imposed by the space group symmetry. During the SA runs, the three rotations, three translations, and the torsion angle of the

rigid body were set flexible. The carbon dioxide molecule was described as a single rigid body in a *z* matrix notation, which was freely rotated and translated during the SA runs. The occupancy factors of the linker atoms, and the cobalt atom, were set to 1, whereas the occupancy factors of the carbon dioxide atoms were varied as a single parameter. An overall thermal displacement factor for each rigid body, and the cobalt atom, were included as variables in the SA process within expected limits.

Once a global minimum was found, the crystal structure was subjected to Rietveld refinement,[11] in which bond lengths and angles were refined within the rigid bodies, together with free refinement of all profile and lattice parameters, as well as the *y* fractional coordinate of the cobalt atom. The refinement converged quickly, with the figures of merit presented in Table 3.S2. The final Rietveld plot is presented in Figure 3.S24. Hydrogen atoms were added at calculated positions by the program Mercury.[12] It is noted that this material displays a high degree of strain, visible in the broadness and paracrystallinity of the peaks in the X-ray diffraction pattern. As a result, the refinement resulted in low precision on the C-C bonds of the structural model. While this is not ideal, the values obtained are reasonable given the limitations of the data.

The same procedure was repeated for the sample collected at 7.2 bar gas pressure of 50:50 CO_2:CH_4. The crystal structure was found to be identical to that of the first CO_2-expanded phase described above (Figure 3.3d). The final Rietveld plot is presented in Figure 3.S25.

Additionally, powder X-ray diffraction patterns of Co(bdp) obtained under 11.7 bar of pure carbon dioxide gas and 14.9 bar of 50:50 CO_2:CH_4 were analyzed. While structural determination was ultimately unsuccessful, pattern indexing was done with the singular value decomposition method[8], resulting in a monoclinic unit cell. The space group was assumed to be *C*2/*c*, and Pawley refinements[9] were used to determine the precise unit cell lattice and peak profile parameters for the two powder X-ray diffraction patterns (Table 3.S1; Figures 3.S26-3.S27).

Breakthrough Experiments

Breakthrough experiments were conducted with Co(bdp) as a microcrystalline powder due to difficulty in forming pellets capable of withstanding the large volume change of the framework upon adsorption. A 6" stainless-steel column (0.25" OD, wall thickness 0.035") was packed with 0.51 g of activated Co(bdp) in a nitrogen-filled glovebox. The final length of packed material was approximately 3", and the remaining column volume was filled loosely with glass wool to allow room for adsorption-induced expansion of Co(bdp). The final packed volume of material was approximately 1.25 cm^3. The column was sealed with VCR fittings using 2 μm fritted, stainless steel gaskets and was then attached to a U-shaped piece of stainless-steel tubing fitted with quarter-turn Swagelok plug valves. The column was removed from the glovebox and attached to a manifold consisting of a minimum volume of 1/8" copper tubing fed by four individual Parker-Porter mass flow controllers. The manifold was purged with He through a bypass line before opening the adsorbent column to the manifold. (Note that Co(bdp) degrades upon exposure to humid air.) The U-shaped column was kept in a 4 L water bath at room temperature (22(1) °C).

An SRI Instruments 8610V GC with a 6' Haysep-D column and a thermal conductivity detector (TCD) was used to monitor the breakthrough profile at 1 min

intervals. The TCD was calibrated using a series of pre-mixed, Certified Standard tanks of varying percent CO_2 (10, 50, and 90%) in CH_4 as well as pure, research-grade CO_2 and CH_4. A total inlet flow rate of 5 standard cubic centimeters per minute (sccm) or 15 sccm was used for all experiments, as specified in the figure captions. Flow rates were validated using an Agilent ADM Universal Flow Meter and were monitored every 0.5 s at the GC outlet over the course of each experiment. A Swagelok KPB series back-pressure regulator was placed between the column outlet and GC inlet to control the column pressure. An Ashcroft DG25 digital pressure gauge was placed at the column inlet to determine the pressure drop across the column. Activation between breakthrough experiments was performed under a flow of 5 sccm of He at room temperature (22(1) °C) and atmospheric pressure for 12 h. The system deadspace was estimated by measuring the initial breakthrough time of Ar (a non-adsorbing probe gas) on a column pre-equilibrated under He with equivalent experimental conditions. Prior to each experiment, the column was equilibrated under He at the experimental temperature (22 °C) and pressure (1 bar or 7 bar absolute pressure, as specified in the figure captions). To begin each experiment, He flow to the column was stopped as a flow of 50% CO_2 in CH_4 was simultaneously switched to the column inlet. Following complete breakthrough of CO_2, the capacity of each gas (q_i, mmol/g) was determined using the following formula:

$$q_i = \left[\frac{Q}{22.414\frac{cc_{STP}}{mmol}}\left(\int_0^t\left(1-\frac{F_i}{F_{0,i}}\right)dt - t_{0,\mathrm{Ar}}\right) - \varepsilon V\left(\frac{y_i P}{RT}\right)\right]\left(\frac{y_i}{m}\right)$$

Here, Q is the average total flow rate in sccm, t is the corrected time in min, F_i is the molar flow rate of species i at time t, $F_{0,i}$ is the inlet molar flow rate of species i, ε is the interparticle void fraction, V is the volume of pelletized adsorbent in cm^3, $t_{0,\mathrm{Ar}}$ is the initial breakthrough time of Ar under equivalent experimental conditions, y_i is the mole fraction of species i, P is the total pressure, R is the universal gas constant, T is the column temperature during the experiment, and m is the mass of adsorbent. The interparticle void fraction ε is calculated as

$$\varepsilon = 1 - \frac{\rho_{bulk}}{\rho_{particle}}$$

where ρ_{bulk} is the bulk density in kg/m^3, calculated as m/V = 408 kg/m^3, and $\rho_{particle}$ is the particle density in kg/m^3, estimated as 774 kg/m^3, the previously reported crystallographic density of Co(bdp)[1]. The term corresponding to the void volume accounted for <0.5% of the total adsorbed gas in a typical experiment in this work.

Breakthrough data are shown in Figures 3.S30–3.S34. For experiments at 7 bar absolute pressure, significant back-mixing was observed in the column. To quantify and correct for this, Ar was used as a non-adsorbing probe gas to collect breakthrough curves under equivalent conditions (Figure 3.S31). In this case, the CO_2 and CH_4 capacities were instead calculated by subtracting the integrated breakthrough time for Ar from that of each adsorbate under equivalent experimental conditions:

$$q_i = \left[\frac{Q}{22.414 \frac{cc_{STP}}{mmol}} \left(\int_0^t \left(1 - \frac{F_i}{F_{0,i}} \right) dt - \int_0^t \left(1 - \frac{F_{\mathrm{Ar}}}{F_{0,\mathrm{Ar}}} \right) dt \right) - \varepsilon V \left(\frac{y_i P}{RT} \right) \right] \left(\frac{y_i}{m} \right)$$

A CO_2 breakthrough capacity of 3.0 ± 0.3 mmol/g was calculated from the experiment performed under 15 sccm of 50:50 CO_2:CH_4 at 7 bar absolute pressure and 22 °C (shown in Figure 3.S30). The low GC scan resolution (1 scan per min), back-mixing, and small sample volume led to large uncertainties on the order of ±0.3 mmol/g in the calculated CO_2 capacities. The CH_4 breakthrough capacity was within error of zero following correction from the Ar breakthrough curve collected under equivalent conditions. Therefore the breakthrough experiments yielded the same result as the equilibrium experiments in the main text: Co(bdp) selectively adsorbs CO_2 and negligible CH_4 from a 50:50 CO_2:CH_4 mixture at 7 bar.

The unusual CO_2 breakthrough profile observed in Figures 3.S30 and 3.S33 results from the inability of Co(bdp) to capture CO_2 at partial pressures below the first CO_2 phase transition pressure (~2 bar at 22 °C, or 29% of the total pressure). This phenomenon has been discussed previously for other flexible frameworks.[13] To control amount of CO_2 in the product stream, the temperature at which the breakthrough separation is performed can be varied, as the pressure at which the first CO_2-induced phase change occurs has a strong temperature dependence (Figure 3.4a). Alternatively, the position of the CO_2-induced step can be controlled by functionalization of the bdp^{2-} linker (Figure 3.5).

Supporting Tables

Table 3.S1. Crystallographic parameters for evacuated Co(bdp) and for gas-dosed phases. Experimental conditions, unit cell parameters and figures-of-merit as determined by Rietveld and Pawley refinement using powder X-ray diffraction patterns of evacuated Co(bdp), as well as Co(bdp) dosed with pure CO_2 gas and a 50:50 mixture of CO_2:CH_4 at 11.7 bar and 14.9 bar, respectively.

	Evacuated Co(bdp)	Co(bdp) dosed with 11.7 bar CO_2	Co(bdp) dosed with 14.9 bar CO_2/CH_4
λ (Å)	0.45336	0.45336	0.45336
Temp. (K)	298 K	298 K	298 K
Space Group	*C*2/*c*	*C*2/*c*	*C*2/*c*
a (Å)	24.838(6)	22.514(12)	22.577(8)
b (Å)	6.7527(11)	14.056(7)	13.953(4)
c (Å)	7.1380(13)	7.006(4)	6.980(2)
β (º)	92.41(2)	96.14(4)	96.32(2)
V (Å^3)	1196.2(4)	2204(2)	2185.5(11)
R_{wp}	11.31%	7.69%	7.01%
R_{exp}	2.61%	2.02%	1.99%
R_{Bragg}	4.20%	0.90%	4.10%
R_p	8.46%	4.32%	4.30%
GoF	4.34	3.81	3.52

Table 3.S2. Crystallographic parameters for solved structures. Experimental conditions, unit cell parameters and figures-of-merit as determined by Rietveld refinement of crystal structures against the powder X-ray diffraction patterns of Co(bdp) dosed with pure CO_2 gas and a 50:50 mixture of CO_2:CH_4 at 3.6 bar and 7.2 bar, respectively. These two patterns can be fit to isostructural, partially-expanded phases (Figure 3.3d).

	Co(bdp) dosed with 3.6 bar of CO_2	Co(bdp) dosed with 7.2 bar CO_2/CH_4
λ (Å)	0.45336	0.45336
Temp. (K)	298 K	298 K
Space Group	*C*2/*c*	*C*2/*c*
a (Å)	24.701(7)	24.700(6)
b (Å)	8.211(3)	8.211(2)
c (Å)	7.089(19)	7.089(17)
β (º)	90.26(5)	90.24(4)
V (Å^3)	1437.9(7)	1437.7(6)
R_{wp}	10.82%	10.00%
R_{exp}	2.56%	2.50%
R_{Bragg}	2.57%	2.09%
R_p	7.55%	6.65%
GoF	4.23	4.01

Supporting Figures

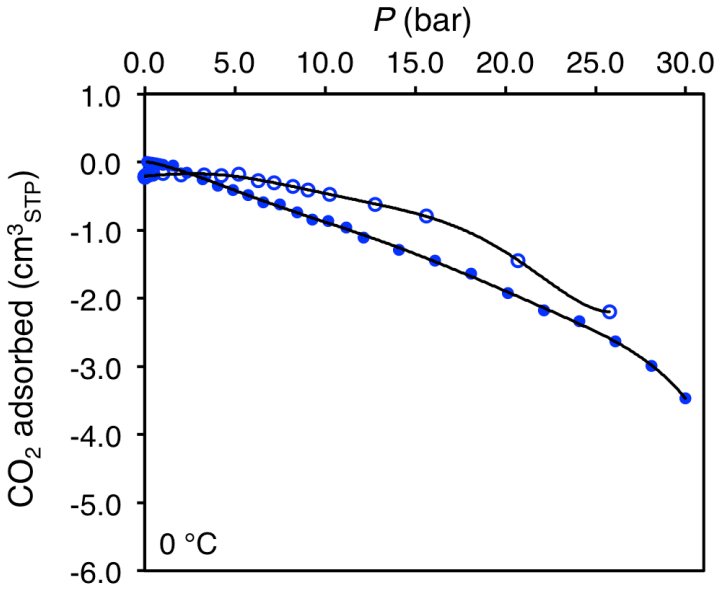

Figure 3.S1. Background CO_2 adsorption at 0 °C. Background CO_2 adsorption was measured with an empty sample holder at 0 °C. Closed circles represent adsorption, open circles represent desorption, and black lines are polynomial fits of the data.

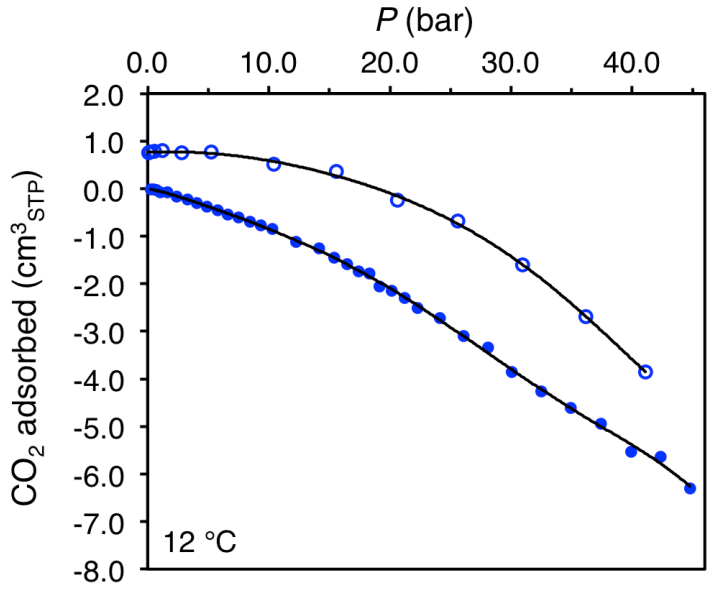

Figure 3.S2. Background CO_2 adsorption at 12 °C. Background CO_2 adsorption was measured with an empty sample holder at 12 °C. Closed circles represent adsorption, open circles represent desorption, and black lines are polynomial fits of the data.

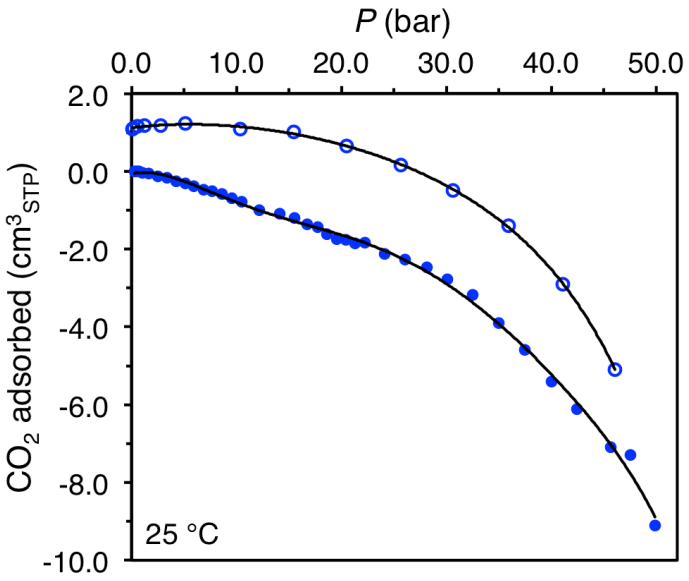

Figure 3.S3. Background CO_2 adsorption at 25 °C. Background CO_2 adsorption was measured with an empty sample holder at 25 °C. Closed circles represent adsorption, open circles represent desorption, and black lines are polynomial fits of the data.

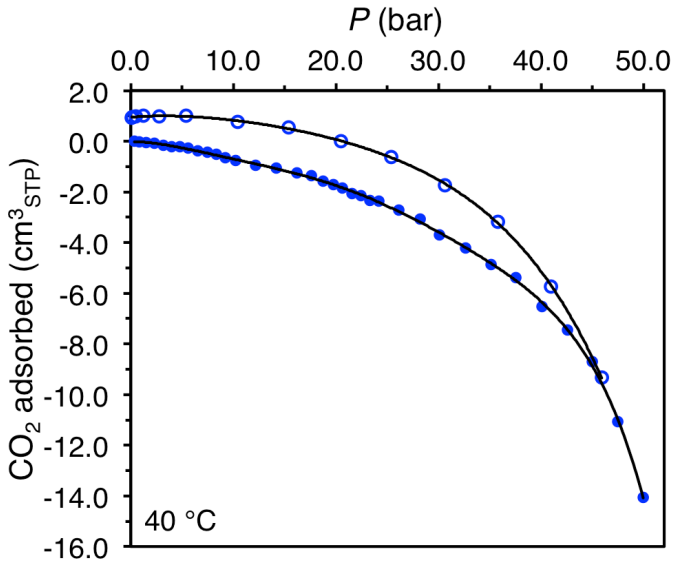

Figure 3.S4. Background CO_2 adsorption at 40 °C. Background CO_2 adsorption was measured with an empty sample holder at 40 °C. Closed circles represent adsorption, open circles represent desorption, and black lines are polynomial fits of the data.

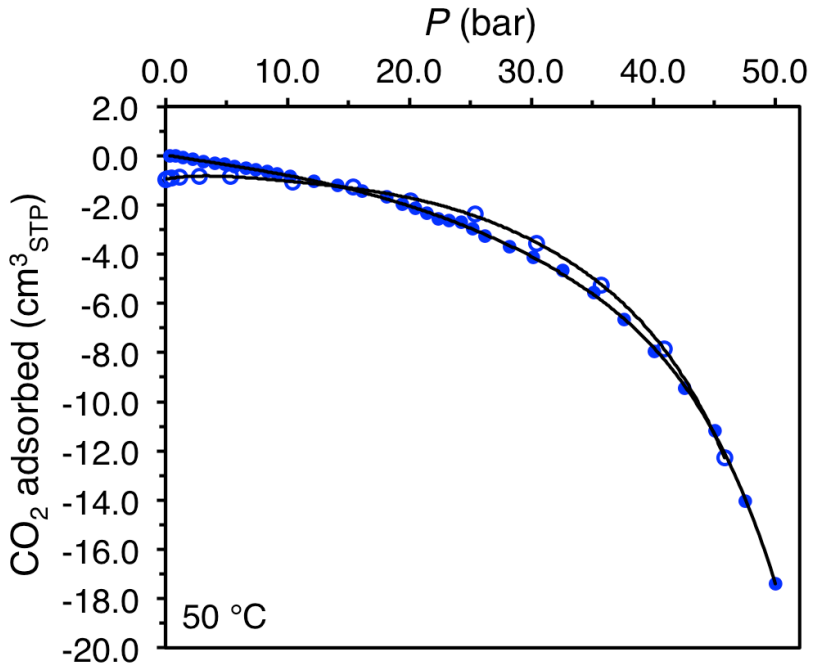

Figure 3.S5. Background CO_2 adsorption at 50 °C. Background CO_2 adsorption was measured with an empty sample holder at 50 °C. Closed circles represent adsorption, open circles represent desorption, and black lines are polynomial fits of the data.

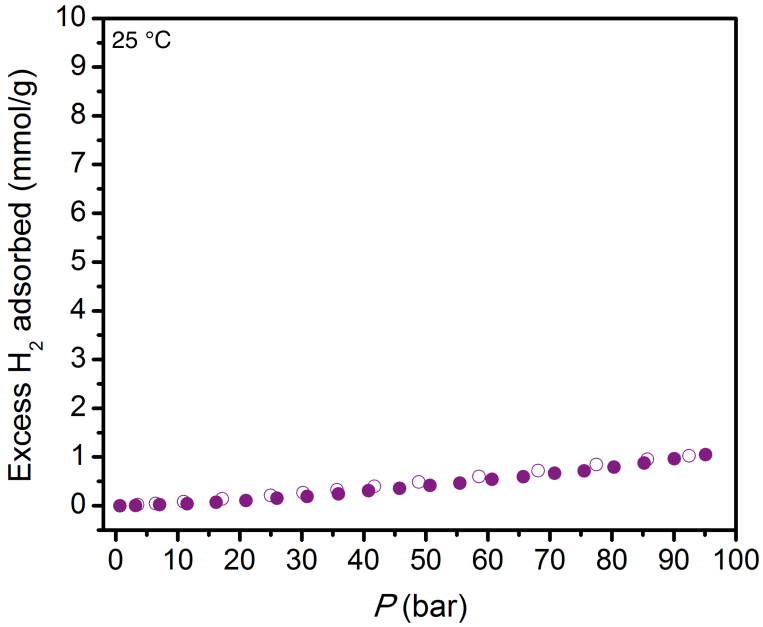

Figure 3.S6. H_2 adsorption in Co(bdp). H_2 adsorption (closed circles) and desorption (open circles) was measured at 25 °C in Co(bdp).

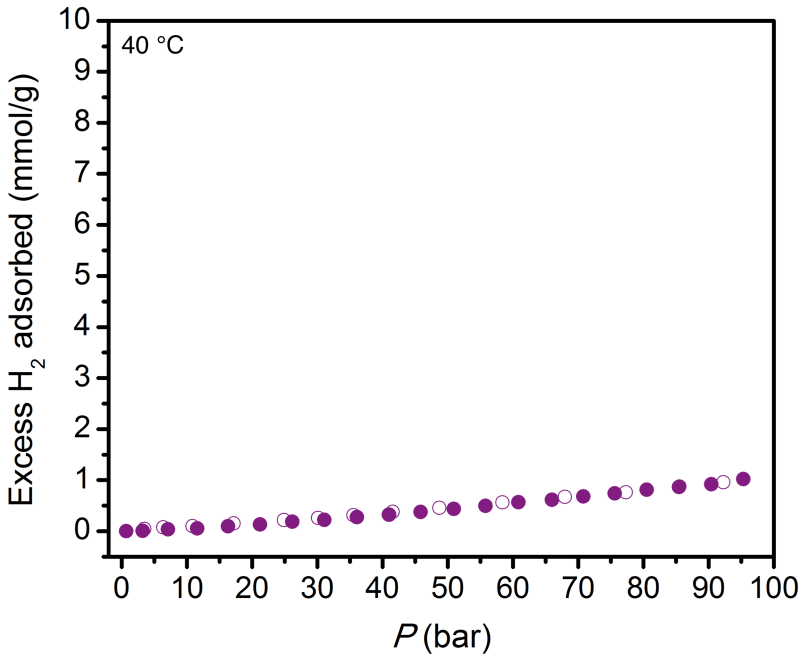

Figure 3.S7. H_2 adsorption in Co(bdp). H_2 adsorption (closed circles) and desorption (open circles) was measured at 40 °C in Co(bdp).

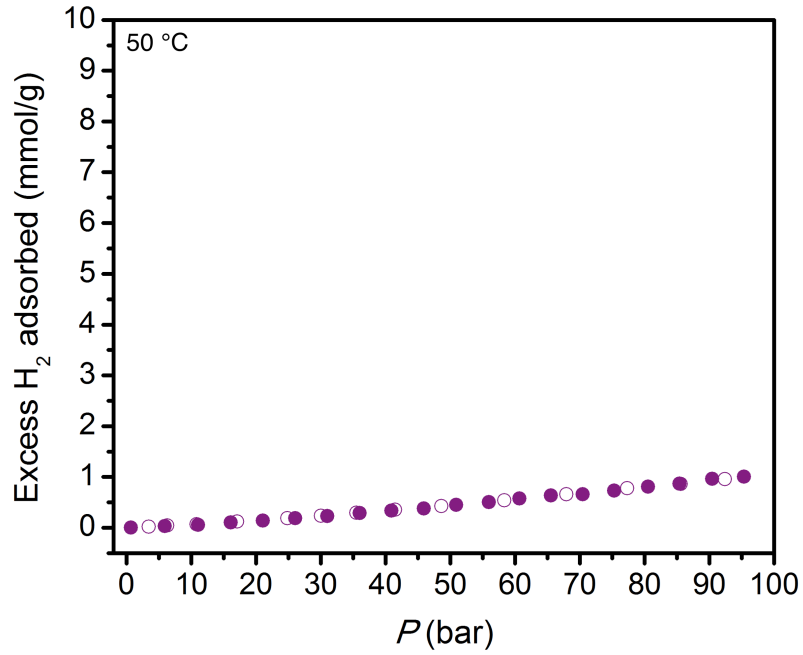

Figure 3.S8. H_2 adsorption in Co(bdp). H_2 adsorption (closed circles) and desorption (open circles) was measured at 50 °C in Co(bdp).

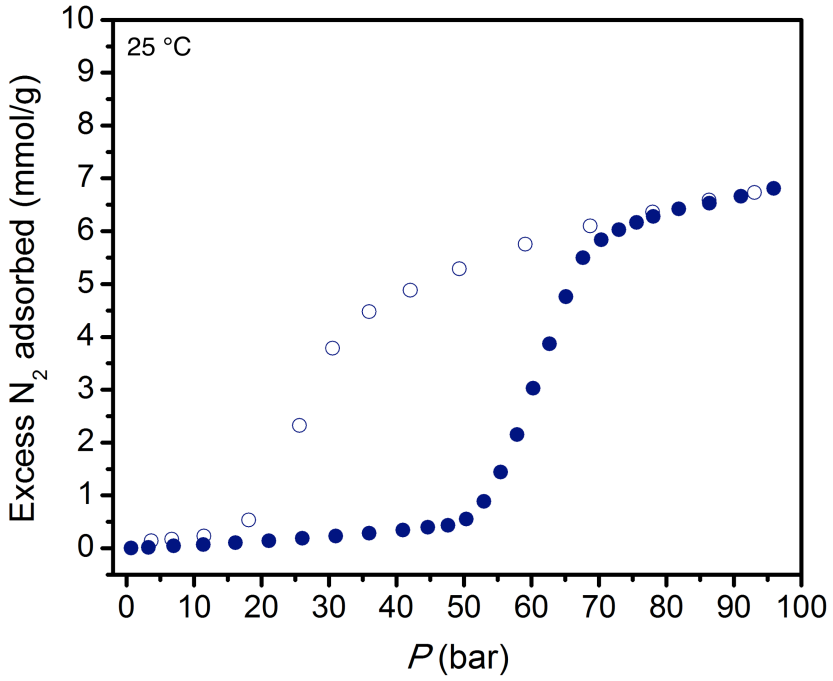

Figure 3.S9. N_2 adsorption in Co(bdp). N_2 adsorption (closed circles) and desorption (open circles) was measured at 25 °C in Co(bdp).

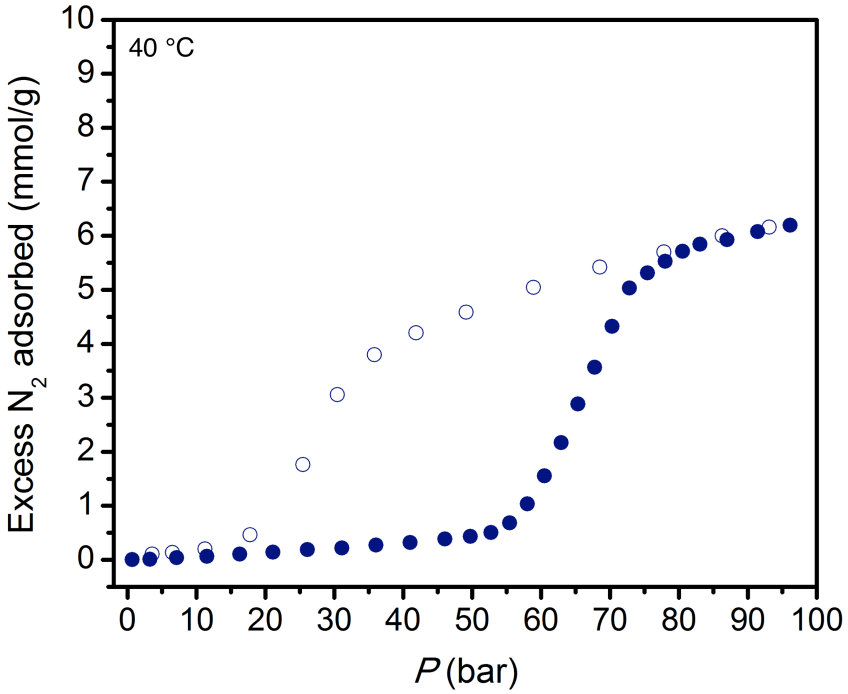

Figure 3.S10. N_2 adsorption in Co(bdp). N_2 adsorption (closed circles) and desorption (open circles) was measured at 40 °C in Co(bdp).

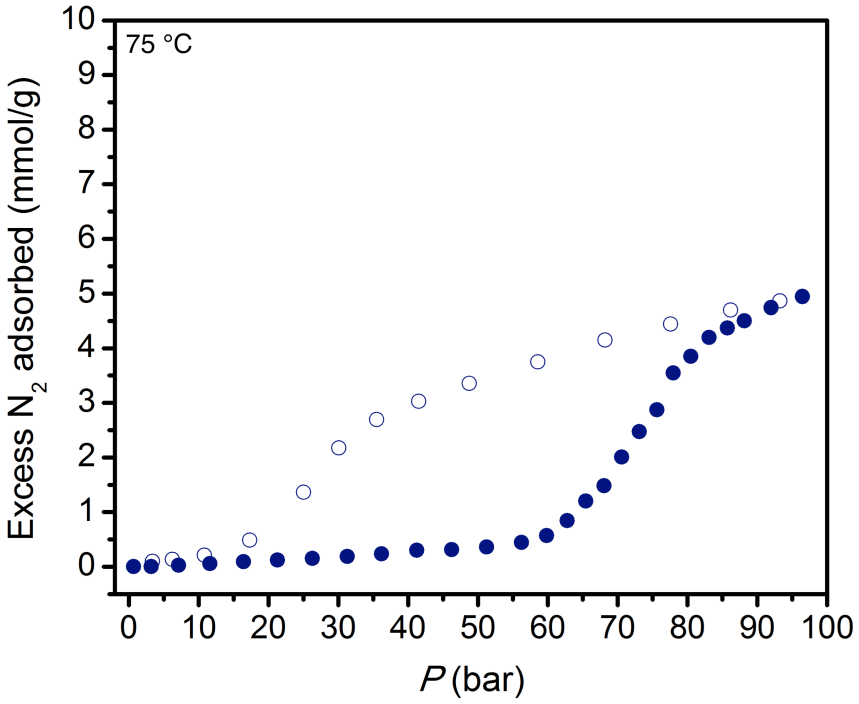

Figure 3.S11. N_2 adsorption in Co(bdp). N_2 adsorption (closed circles) and desorption (open circles) was measured at 75 °C in Co(bdp).

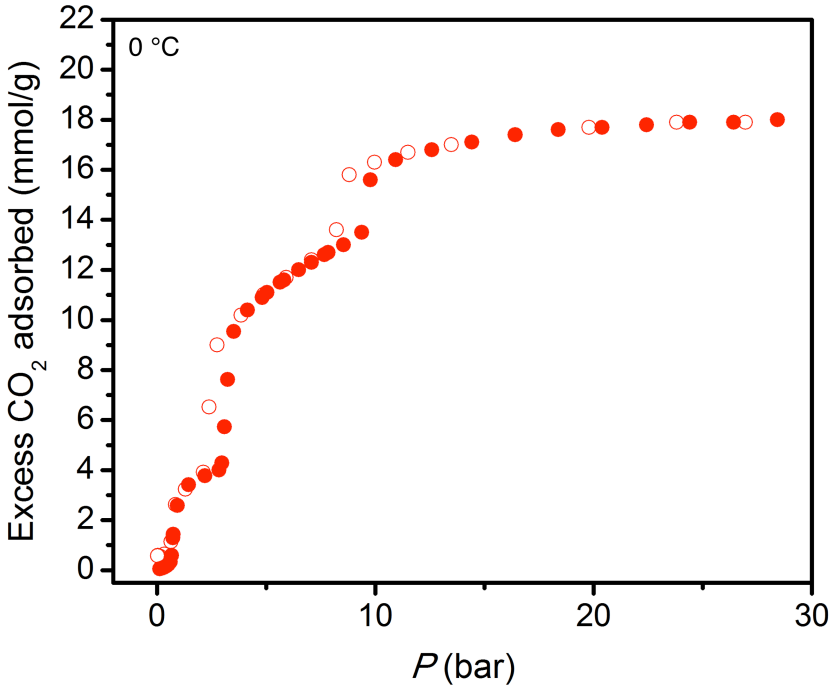

Figure 3.S12. CO_2 adsorption in Co(bdp). CO_2 adsorption (closed circles) and desorption (open circles) was measured at 0 °C in Co(bdp).

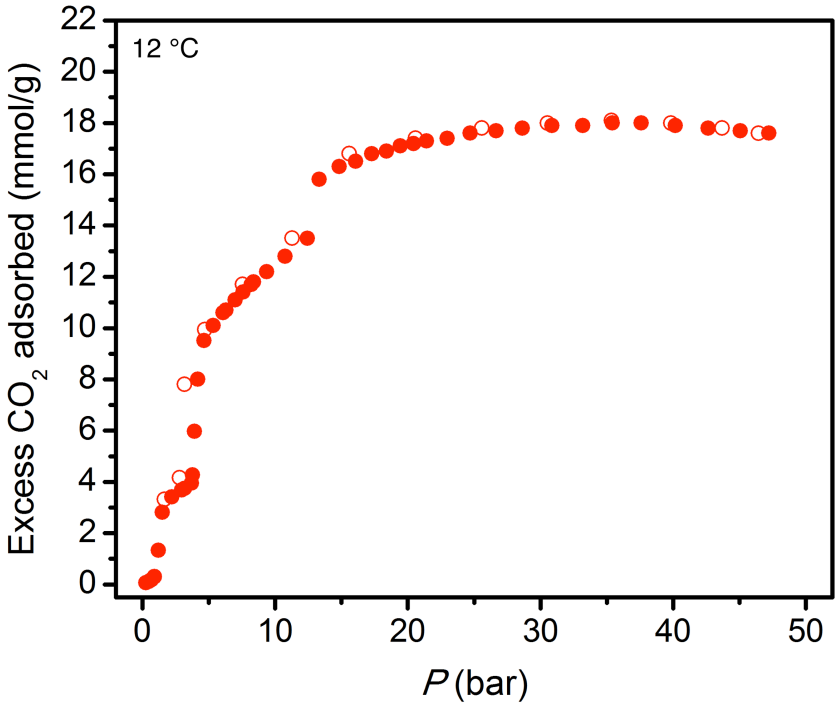

Figure 3.S13. CO_2 adsorption in Co(bdp). CO_2 adsorption (closed circles) and desorption (open circles) was measured at 12 °C in Co(bdp).

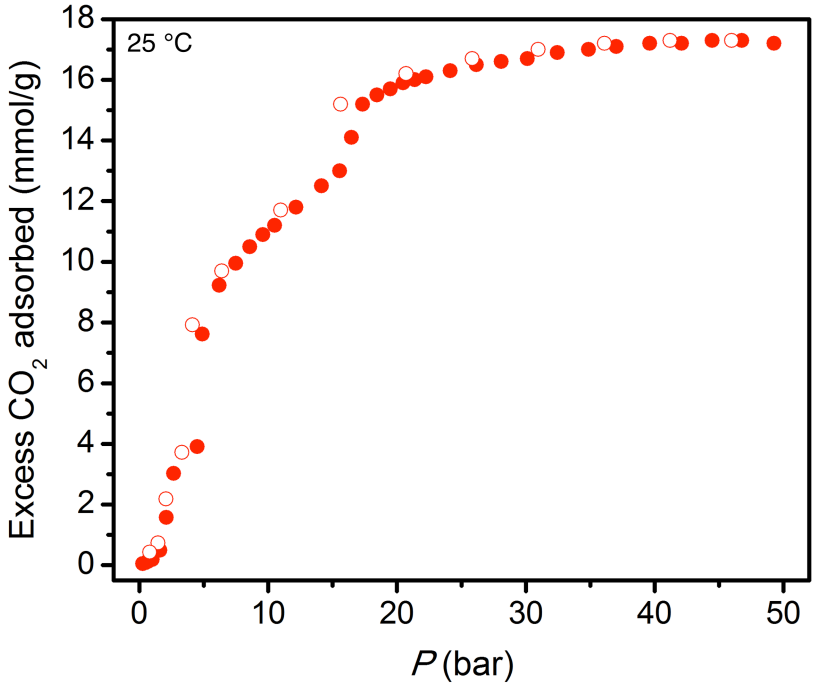

Figure 3.S14. CO_2 adsorption in Co(bdp). CO_2 adsorption (closed circles) and desorption (open circles) was measured at 25 °C in Co(bdp).

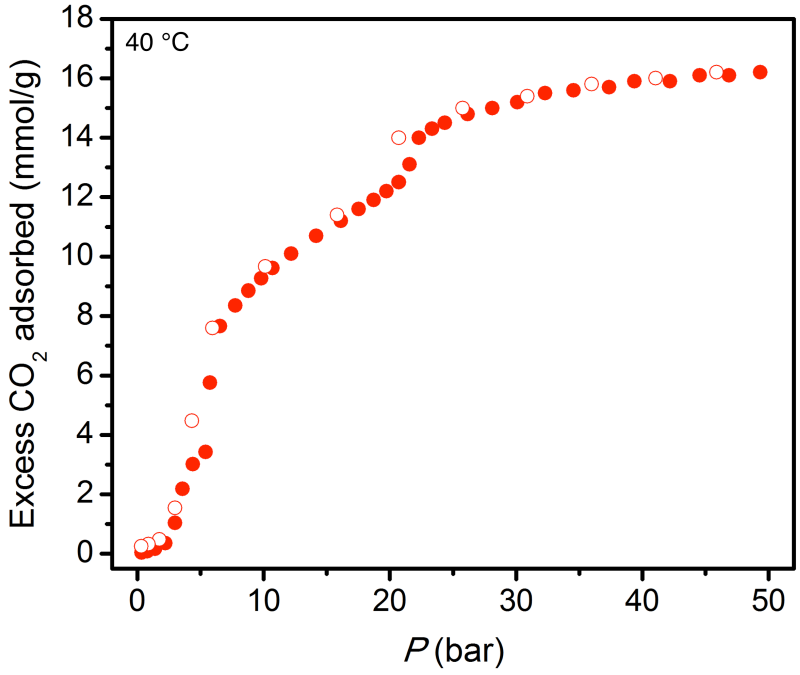

Figure 3.S15. CO_2 adsorption in Co(bdp). CO_2 adsorption (closed circles) and desorption (open circles) was measured at 40 °C in Co(bdp).

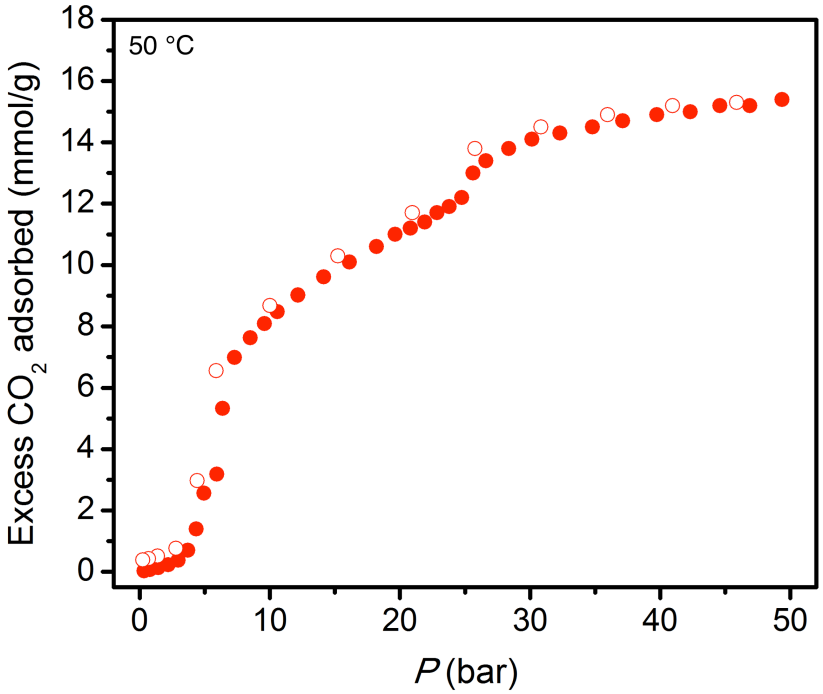

Figure 3.S16. CO_2 adsorption in Co(bdp). CO_2 adsorption (closed circles) and desorption (open circles) was measured at 50 °C in Co(bdp).

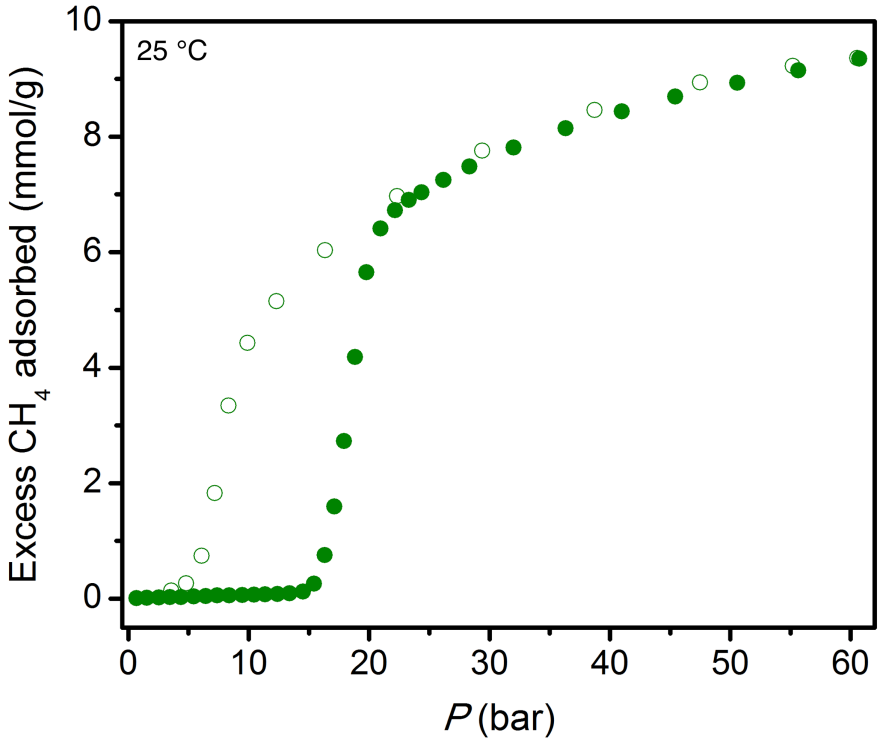

Figure 3.S17. CH_4 adsorption in Co(bdp). CH_4 adsorption (closed circles) and desorption (open circles) was measured at 25 °C in Co(bdp).

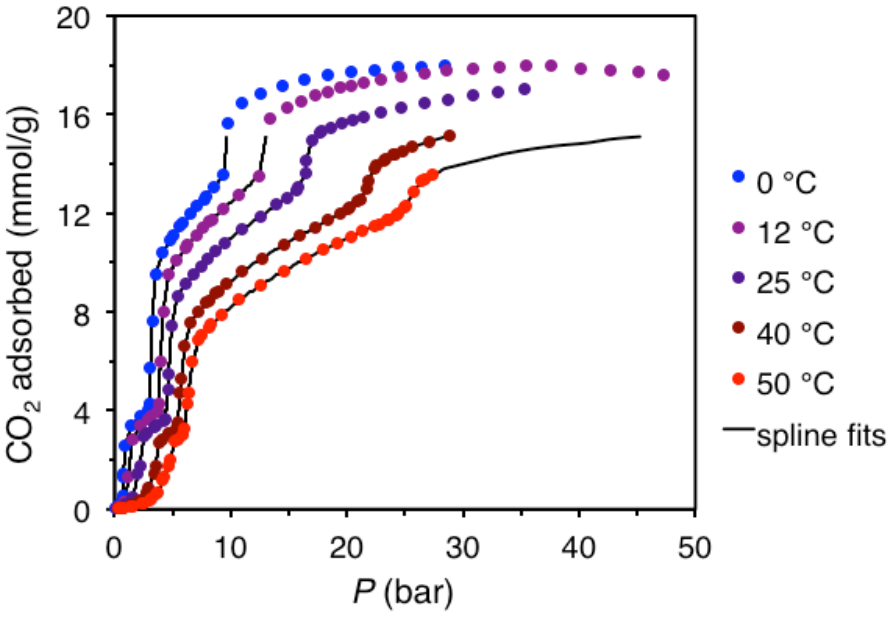

Figure 3.S18. CO_2 isotherm fits. CO_2 adsorption isotherms for Co(bdp) at 0, 12, 25, 40, and 50 °C, along with the corresponding spline fit for each isotherm.

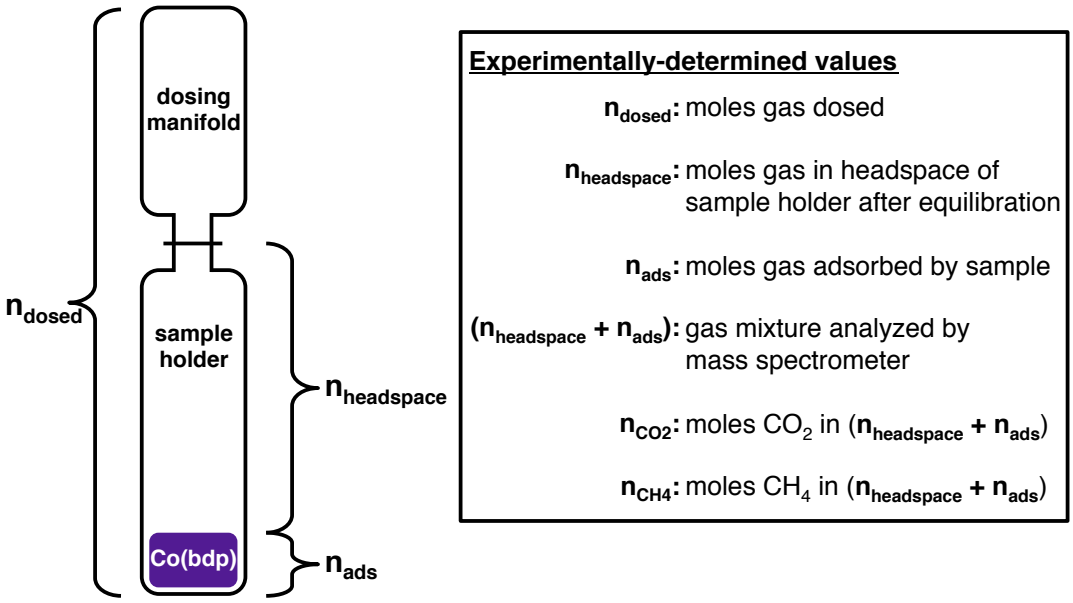

Figure 3.S19. Multicomponent adsorption system. A schematic of the dosing manifold and sample holder, with a summary of experimentally-determined values.

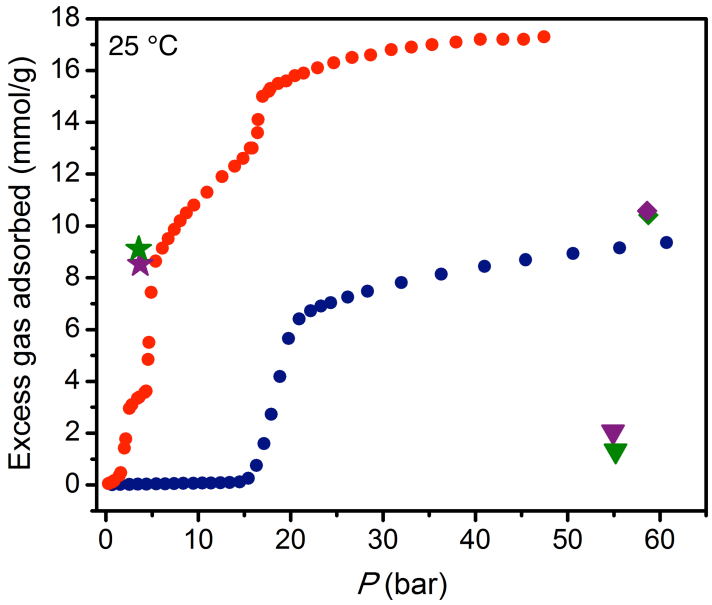

Figure 3.S20. 6:94 CO_2:CH_4 multicomponent adsorption experiments. The 6:94 CO_2:CH_4 adsorption experiment was repeated to verify reproducibility (purple and green symbols represent the first and second trials, respectively), yielding very similar results for total mixed-gas adsorption (diamonds). Stars represent CO_2 adsorption and triangles represent CH_4 adsorption.

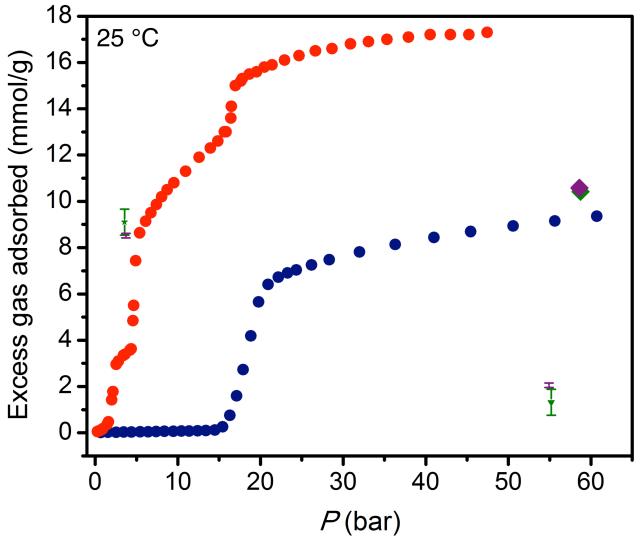

Figure 3.S21. Error in multicomponent adsorption data. Each gas mixture resulting from the two 6:94 CO_2:CH_4 adsorption experiments depicted in Figure S2 was analyzed twice by mass spectrometry, which allowed us to calculate the standard error for CO_2 and CH_4 adsorption for each experiment.

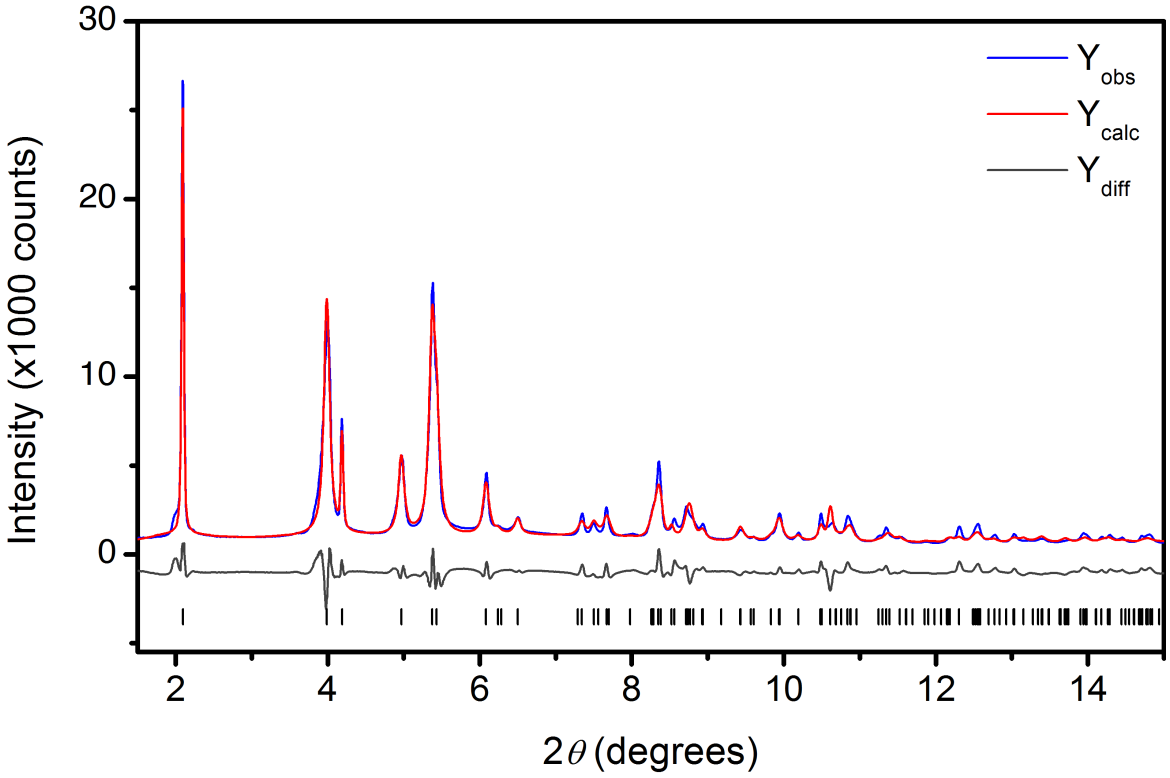

Figure 3.S22. Rietveld refinement of evacuated Co(bdp). The Rietveld refinement of a sample of Co(bdp) at 0 bar and 298 K from 1.5º to 15º using the previously published structural model for evacuated Co(bdp)[1] gives an excellent fit to the experimental data. Blue and red lines represent the observed and calculated diffraction patterns, respectively. The gray line represents the difference between observed and calculated patterns, and the black tick marks indicate calculated Bragg peak positions. Figures-of-merit (as defined by TOPAS): R_{wp} = 11.31%, R_p = 8.46%, R_{exp} = 2.61%, R_{Bragg} = 4.20%, GoF = 4.34. The wavelength was 0.45336 Å.

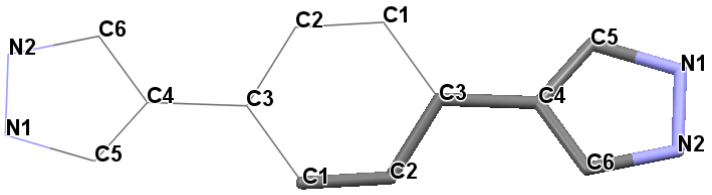

Figure 3.S23. Rigid body description of the linker molecule. The rigid body description of the bdp^{2-} ligand is drawn with bold lines, and the symmetry-generated fragment is drawn with thin lines.

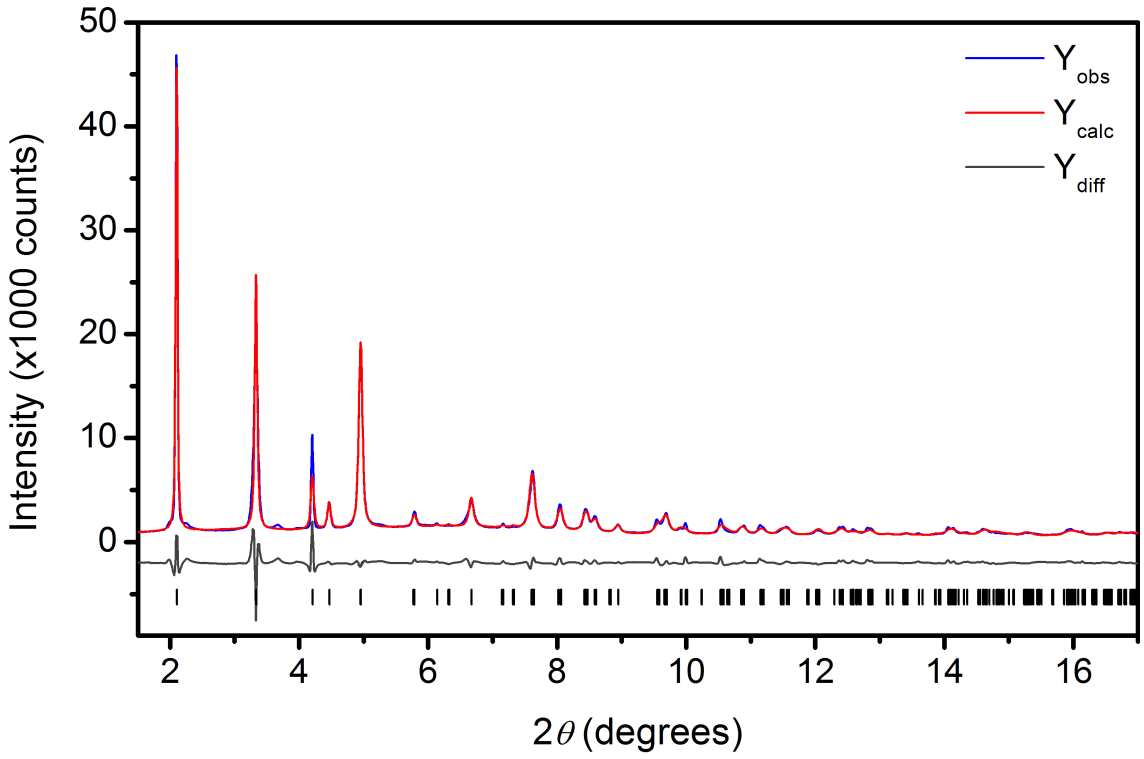

Figure 3.S24. Rietveld refinement of CO_2-dosed Co(bdp). Rietveld refinement of Co(bdp) dosed with 3.6 bar of CO_2 gas at 298 K from 1.5º to 17º. Blue and red lines represent the observed and calculated diffraction patterns, respectively. The gray line represents the difference between observed and calculated patterns, and the black tick marks indicate calculated Bragg peak positions. Figures-of-merit (as defined by TOPAS): R_{wp} = 10.82%, R_p = 7.55%, R_{exp} = 2.56%, R_{Bragg} = 2.57%, GoF = 4.23. The wavelength was 0.45336 Å.

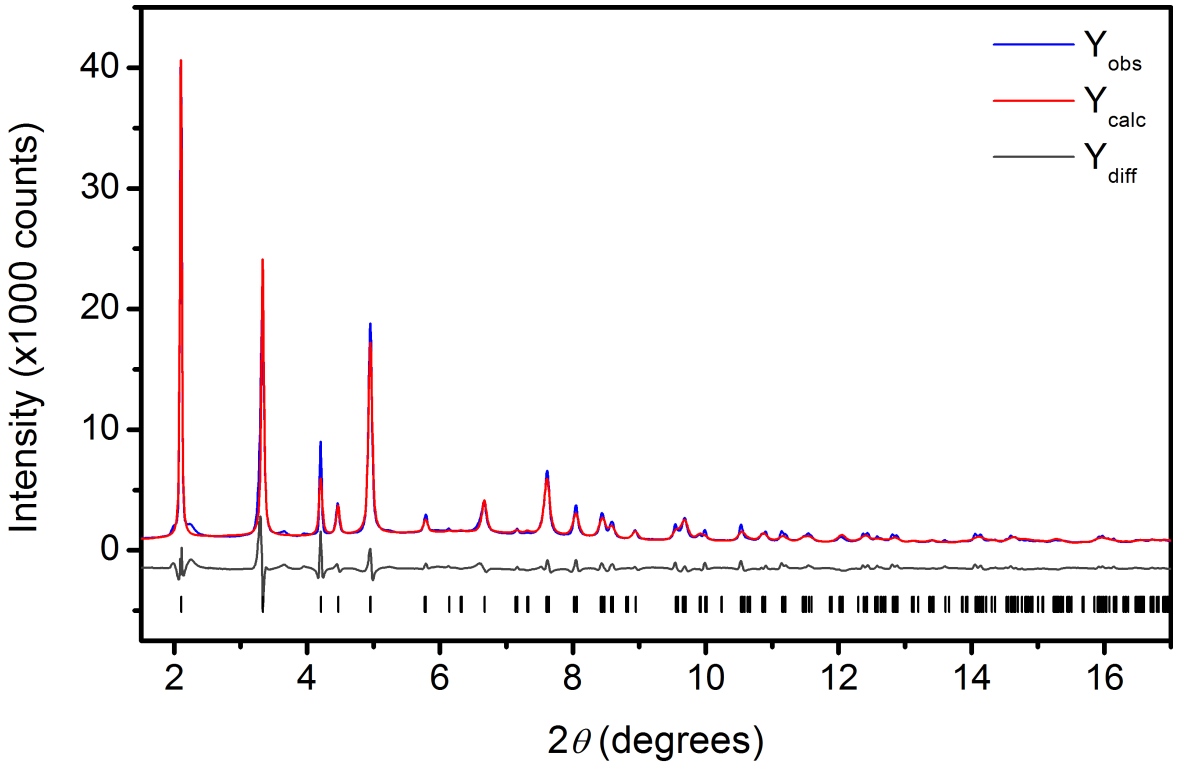

Figure 3.S25. Rietveld refinement of Co(bdp) dosed with mixed gas. Rietveld refinement of Co(bdp) dosed with 7.2 bar of 50:50 CO_2:CH_4 gas at 298 K from 1.5º to 17º. Blue and red lines represent the observed and calculated diffraction patterns, respectively. The gray line represents the difference between observed and calculated patterns, and the black tick marks indicate calculated Bragg peak positions. Figures-of-merit (as defined by TOPAS): R_{wp} = 10.00%, R_p = 6.65%, R_{exp} = 2.50%, R_{Bragg} = 2.09%, GoF = 4.01. The wavelength was 0.45336 Å.

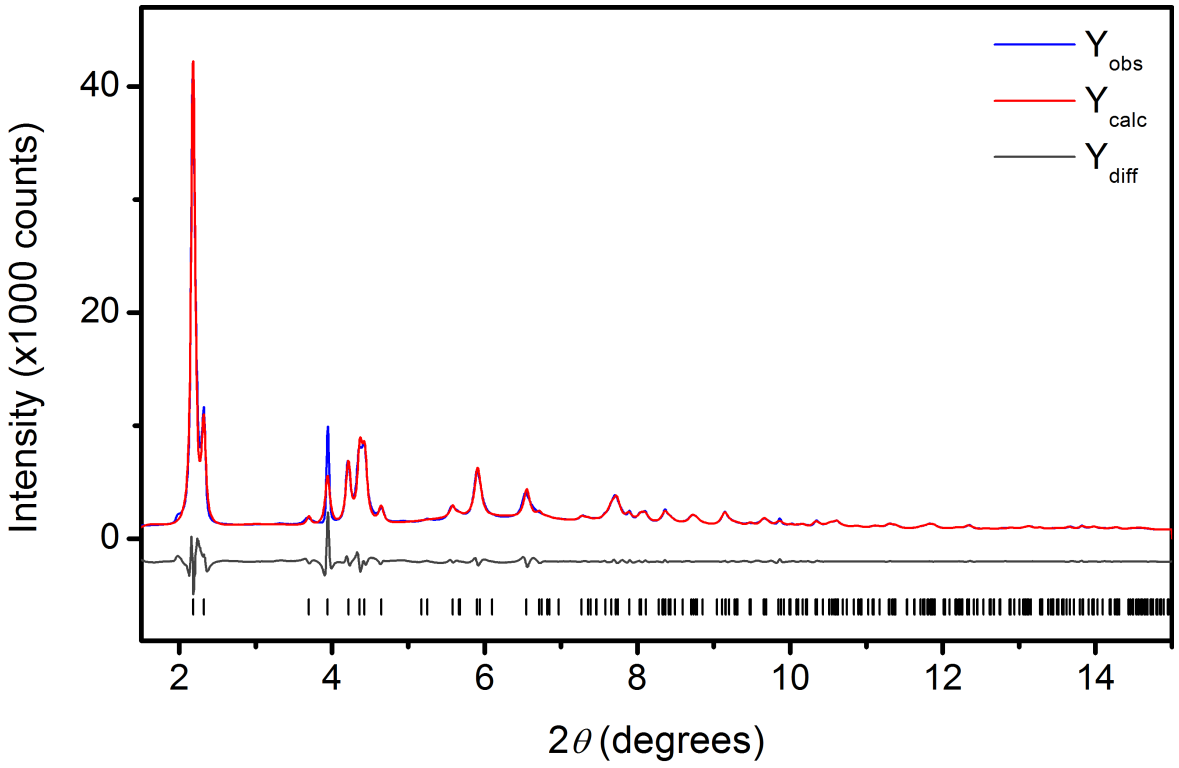

Figure 3.S26. Pawley refinement of CO_2-dosed Co(bdp). The Pawley refinement of Co(bdp) dosed with 11.7 bar of pure CO_2 gas at 298 K from 1.5º to 15º. Blue and red lines represent the observed and calculated diffraction patterns, respectively. The gray line represents the difference between observed and calculated patterns, and the black tick marks indicate calculated Bragg peak positions. Figures-of-merit (as defined by TOPAS): R_{wp} = 7.69%, R_p = 4.32%, R_{exp} = 2.02%, R_{Bragg} = 0.90%, GoF = 3.81. The wavelength was 0.45336 Å.

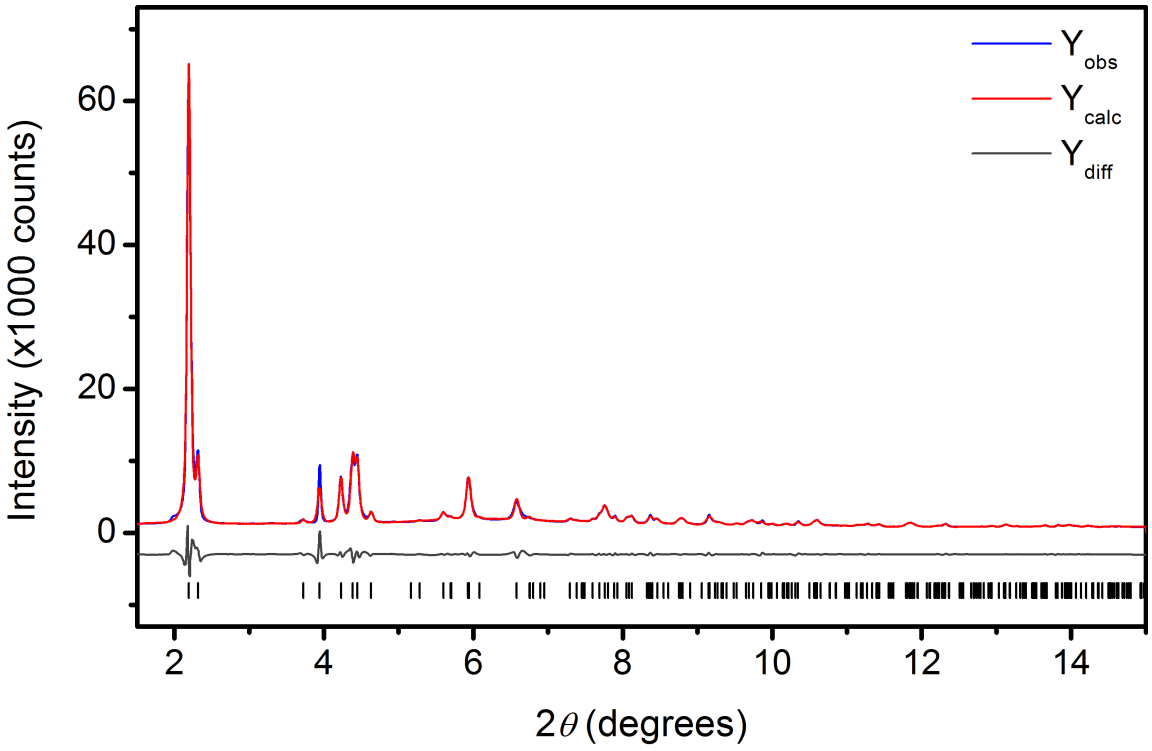

Figure 3.S27. Pawley refinement of Co(bdp) dosed with mixed gas. Pawley refinement of Co(bdp) dosed with 14.9 bar of 50:50 CO_2:CH_4 gas at 298 K from 1.5º to 15º. Blue and red lines represent the observed and calculated diffraction patterns, respectively. The gray line represents the difference between observed and calculated patterns, and the black tick marks indicate calculated Bragg peak positions. Figures-of-merit (as defined by TOPAS): R_{wp} = 7.01%, R_p = 4.30%, R_{exp} = 2.61%, R_{Bragg} = 4.20%, GoF = 3.52. The wavelength was 0.45336 Å.

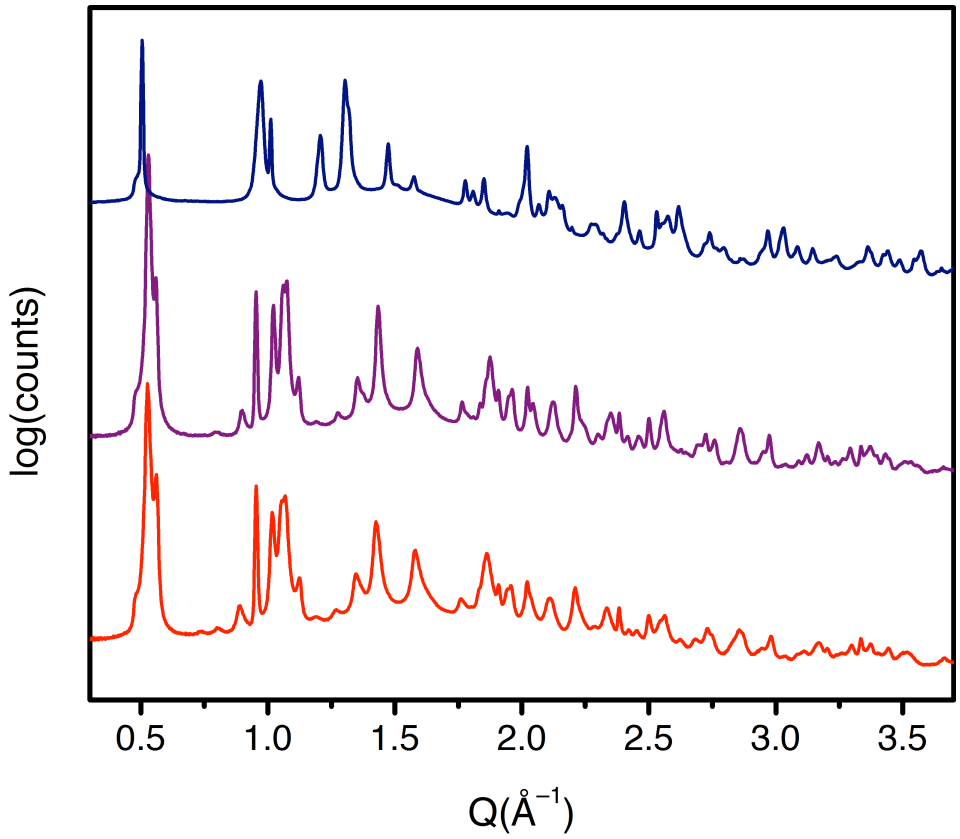

Figure 3.S28. Effect of adsorbate on powder X-ray diffraction data. A comparison of the powder X-ray diffraction data for Co(bdp) dosed with 11.7 bar CO_2 (red), 13.2 bar CH_4 (blue), and 14.9 bar of a 50:50 CO_2:CH_4 mixture (purple) shows that the mixed-gas diffraction pattern closely resembles that of pure CO_2 while the CH_4 data is clearly distinct. The pure CH_4 data was previously published[1]. The pure CH_4 data was collected at a wavelength of 0.75009 Å, the mixed-gas data was collected at 0.45336 Å, and the CO_2 data was collected at 0.45336 Å.

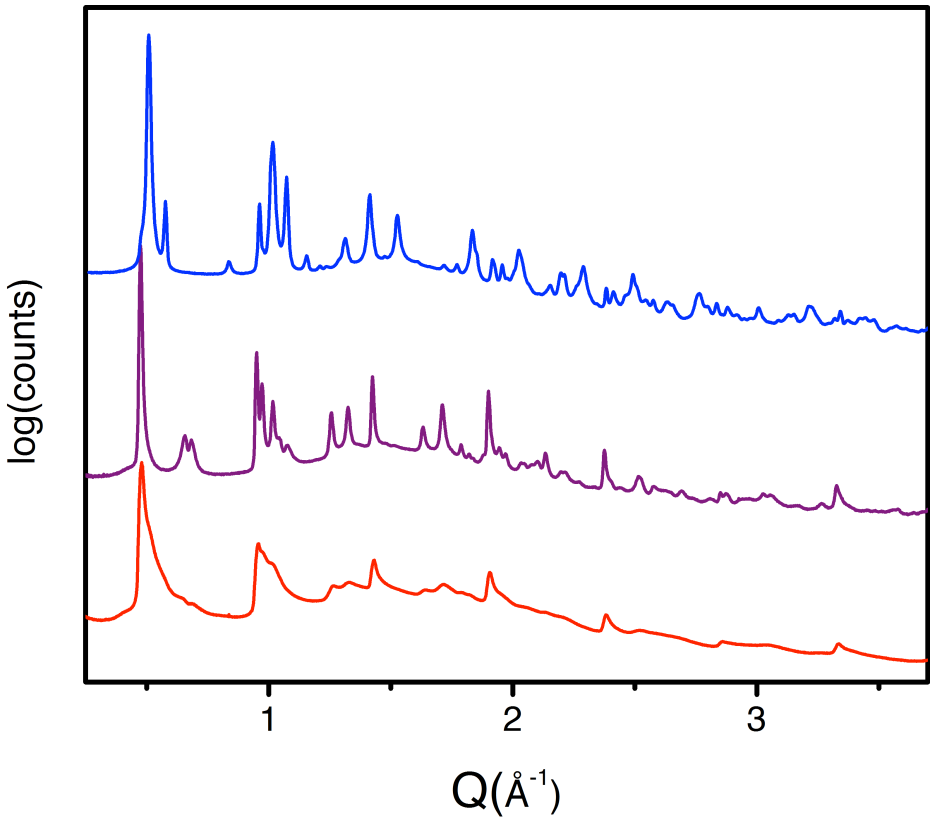

Figure 3.S29. Effect of adsorbate on powder X-ray diffraction data. Powder X-ray diffraction data for Co(bdp) dosed with 29.9 bar CO_2 (red), 23.0 bar CH_4 (blue), and 50.0 bar of a 50:50 CO_2:CH_4 mixture (purple) shows that the the mixed-gas diffraction pattern closely resembles that of pure CO_2, while the CH_4 data is clearly distinct. The pure CH_4 data was previously published[1]. The CO_2-dosed sample displays a great deal of strain at this pressure, as has been seen in other high-pressure gas-dosing experiments in this class of flexible frameworks[1]. The pure CH_4 data was collected at a wavelength of 0.75009 Å, the mixed-gas data was collected at 0.45336 Å, and the CO_2 data was collected at 0.72768 Å.

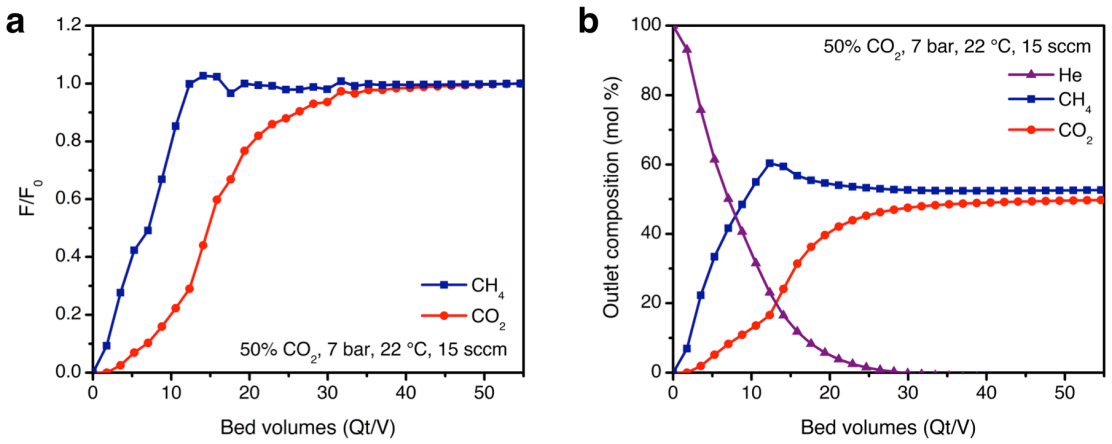

Figure 3.S30. CO_2/CH_4 breakthrough with Co(bdp). Breakthrough of CO_2 (red circles) and CH_4 (blue squares) with Co(bdp) under 15 sccm of 50:50 CO_2:CH_4 at 7 bar absolute pressure and 22 °C. A pressure drop of approximately 0.3 bar was measured across the column. Curves are plotted in terms of **a,** normalized outlet flow rate (F/F_0) and **b,** composition (mol %, right) as a function of bed volumes (Qt/V). Helium composition was calculated as the balance of the calibrated CO_2/CH_4 stream. A CO_2 breakthrough capacity of 3.0 ± 0.3 mmol/g was calculated from this experiment, and the CH_4 breakthrough capacity was within error of zero following correction from the Ar breakthrough curve collected under equivalent conditions. The unusual CO_2 breakthrough profile shown here results from the inability of Co(bdp) to capture CO_2 at partial pressures below the CO_2 phase change pressure (approximately 2 bar at 22 °C, or 29% of the total pressure), a phenomenon has been discussed previously for other flexible frameworks.[13]

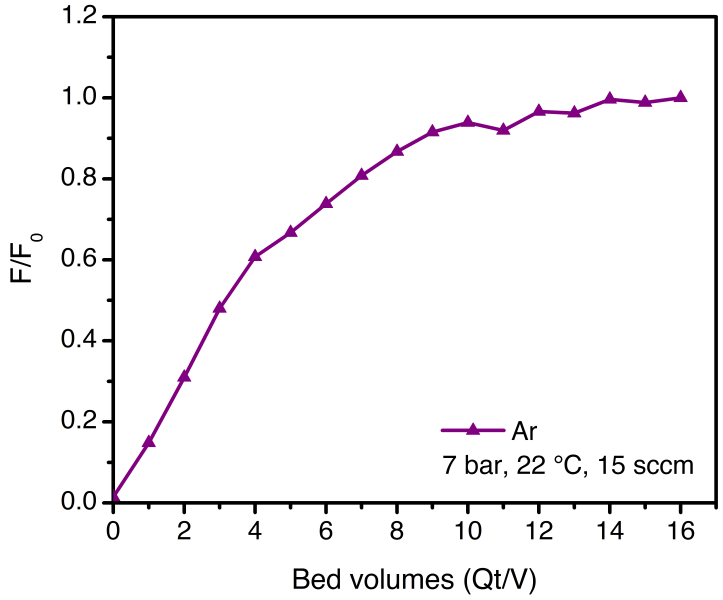

Figure 3.S31. Argon breakthrough with Co(bdp). Breakthrough of Ar (a non-adsorbing probe gas, purple triangles) with Co(bdp) under equivalent experimental conditions as in Figure S30. This curve was used to correct the capacities calculated for the 7 bar experiment reported in Figure S30.

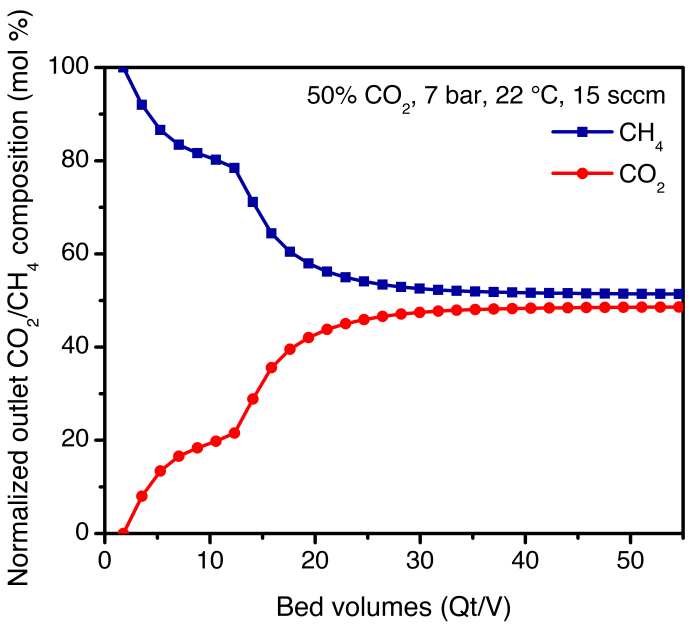

Figure 3.S32. Renormalizing the breakthrough curve in Figure S30 to account exclusively for CO_2 and CH_4 at the outlet suggests the true shape of the breakthrough profile in the absence of He accumulation in the column. Initial "slip" of CO_2 corresponding to the CO_2 step pressure is followed by full breakthrough at saturation. Renormalization was performed by taking the ratio of the calibrated outlet composition of each gas to the sum of the calibrated total CO_2 and CH_4 at the outlet.

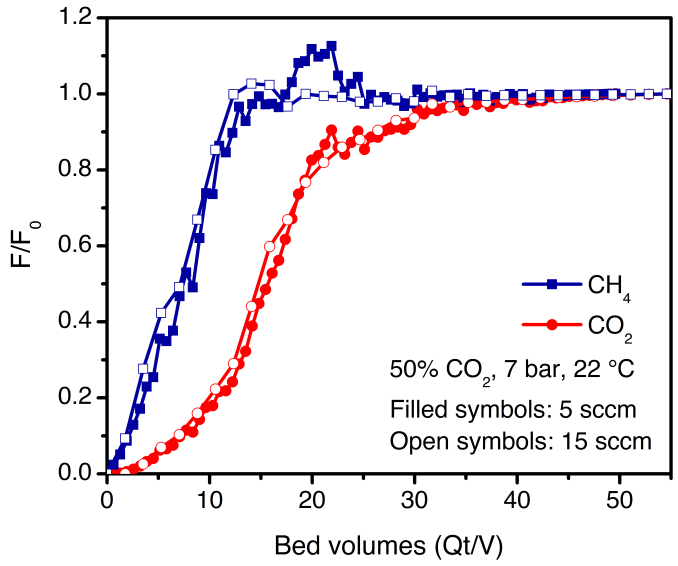

Figure 3.S33. Breakthrough at lower flow rate. Breakthrough of CO_2 (red circles) and CH_4 (blue squares) with Co(bdp) under 50:50 CO_2:CH_4 at 7 bar absolute pressure and 22 °C with a flow rate of 5 sccm (filled symbols). The curves from the equivalent experiment at 15 sccm (Figure S30) are included as open symbols.

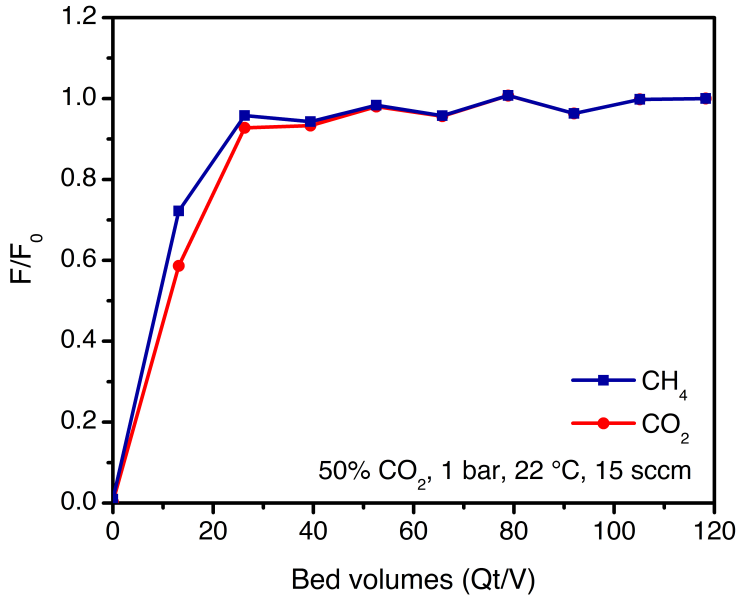

Figure 3.S34. Breakthrough with column exit at atmospheric pressure. Breakthrough of CO_2 (red circles) and CH_4 (blue squares) with Co(bdp) under 15 sccm of 50:50 CO_2:CH_4 at 22 °C with the column exit at atmospheric pressure. A pressure drop of approximately 1 bar was measured across the column. Co(bdp) remains nonporous to both adsorbates under these conditions, and neither gas is retained.

Supporting References

(1) Mason, J. A.; Oktawiec, J.; Taylor, M. K.; Hudson, M. R.; Rodriguez, J.; Bachman, J. E.; Gonzalez, M. I.; Cervellino, A.; Guagliardi, A.; Brown, C. M.; Llewellyn, P. L.; Masciocchi, N.; Long, J. R. *Nature* **2015**, *527,* 357.
(2) H_2bdp was synthesized according to a previously published procedure: Choi, H. J.; Dincă, M.; Long, J. R. *J. Am. Chem. Soc.* **2008**, *130*, 7848.
(3) Taylor, M. K.; Runčevski, T.; Oktawiec, J.; Gonzalez, M. I.; Siegelman, R. L.; Mason, J. A.; Ye, J.; Brown, C. M.; Long, J. R. *J. Am. Chem. Soc.* **2016,** *138*, 15019.
(4) Kinzel, T.; Yong, Z.; Buchwald, S. L *J. Am. Chem. Soc.* **2010**, *132*, 14073.
(5) Smith, J. M.; Van Ness, H. C.; Abbott, M. M. *Introduction to Chemical Engineering Thermodynamics,* 6th ed.; McGraw-Hill: New York, **2003**.
(6) Lemmon, E. W.; Huber, M. L.; McLinden, M. O. *NIST Standard Reference Database 23: Reference Fluid Thermodynamic and Transport Properties REFPROP Version 8.0;* National Institute of Standards and Technology: Gaithersburg, MD, **2007**.
(7) Bruker AXS, Topas, version 4.1. **2007**.
(8) Coelho, A. A. *J. Appl. Cryst.* **2003,** *36,* 86.
(9) Pawley, G. S. *J. Appl. Cryst.* **1981,** *14,* 357.
(10) Andreev, Y. G.; MacGlashan, G. S.; Bruce, P. G. *Phys. Rev. B* **1997,** *55,* 12011.
(11) Rietveld, H. M. *J. Appl. Cryst*. **1969,** *2,* 65.
(12) Mercury CSD 3.3 (Build RC5), **2013**.
(13) Hiraide, S.; Tanaka, H.; Ishikawa, N.; Miyahara, M. T. *ACS Appl. Mater. Interfaces* **2017,** *9,* 41066.

Chapter 4: Novel routes to 4,4'-bipyrazole (H_2bpz) and Co(bpz)

4.1. Introduction

The pyrazole moeity occupies a prominent place in organometallic chemistry, due to the bidentate coordinating ability of the two adjacent nitrogen atoms when deprotonated,[1,2] and this functional group attracts even greater interest in the fields of pharmaceutical and agricultural chemistry due to its pharmacological properties.[3-5] The many other applications of pyrazole-containing compounds include catalysis,[6] energetic materials,[7] and sensing/electroluminescent materials (based upon pyrazole coordination to transition metals).[8-10] In the field of metal–organic frameworks, 4,4'-bipyrazole, its substituted derivatives, and expanded bipyrazole molecules (such as 1,4-benzenedipyrazole, discussed in Chapters 1-3) have been used extensively to construct a crystalline, porous materials with promising gas adsorption properties.[11]

Traditional synthetic routes to 4,4'-bipyrazole entail laborious, multistep sequences and volatile, hazardous reagents (Scheme 4.1).[12-15] Based on the symmetry and simplicity of the molecule, the homocoupling of a monopyrazole starting material is an obvious alternative synthetic pathway. However, attempts to synthesize 4,4'-bipyrazole via the Ullmann reaction (a copper-catalyzed coupling between aryl halides) have been unsuccessful.[15,16] The Suzuki cross-coupling reaction offers a viable way to form a pyrazole–pyrazole bond, but this reaction lacks the elegance and ease of a homocoupling (as it requires both a halopyrazole and a pyrazoleboronic acid as starting materials).[17] The lack of a straightforward synthetic route to bipyrazole-based compounds prompted us to develop a catalytic, scalable protocol to access this class of molecules, with the ultimate synthetic goal of bipyrazole-based metal–organic frameworks for gas separation applications.

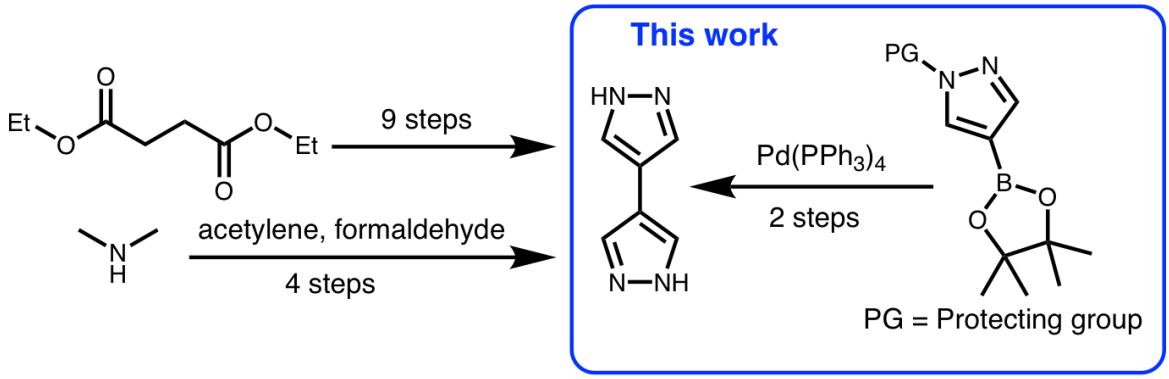

Scheme 4.1. Synthetic routes to 4,4'-bipyrazole (H_2bpz).

During the investigation of benzene-linked bipyrazoles (H_2bdp derivatives) detailed in Chapter 2, the Pd-catalzyed formation of 4,4'-bipyrazole (referred to herein as H_2bpz) was observed as the result of a Suzuki reaction using pyrazoleboronic ester starting material. Although the oxidative homocoupling of aryl boronic esters is well-documented,[18] this reactivity is relatively unexplored in heterocycles, including pyrazoles. Herein we report the first catalytic oxidative homocoupling of a

pyrazoleboronic ester to synthesize the valuable product H_2bpz, and we demonstrate the utility of this multitopic ligand via the synthesis and characterization of the metal–organic framework Co(bpz).

4.2. Experimental Section

NMR spectra were acquired on Bruker AVB-400, AVQ-400, and AV-600 instruments at the University of California, Berkeley, NMR facility. NMR spectra were obtained between 294 and 298.5 K, and all chemical shifts were referenced to residual solvent peaks. Elemental analyses were obtained from the Microanalytical Laboratory of the University of California, Berkeley, using a PerkinElmer 2400 series II combustion analyzer. Infrared spectra were collected on a PerkinElmer Avatar Spectrum 400 FTIR spectrophotometer equipped with a Pike attenuated total reflectance accessory (ATR) accessory. Powder X-ray diffraction patterns were obtained on a Bruker D8 Advance diffractometer with a Cu anode (λ = 1.5418 Å). Anhydrous *N,N*-dimethylformamide (DMF), *N,N*-diethylformamide (DEF), and anhydrous dichloromethane (CH_2Cl_2) were obtained from a JC Meyer solvent system. All other reagents were obtained from commercial vendors and used without further purification. Ultra-high purity (99.999% purity) dinitrogen, helium, carbon dioxide, and dihydrogen were used for all adsorption measurements.

Synthesis of H_2bpz. 1-(2-tetrahydropyranyl)-1H-pyrazole-4-boronic acid pinacol ester (3.00 g, 0.011 mol, 1 equiv), Cs_2CO_3 (3.5 g, 0.011 mol, 1 equiv) and $Pd(PPh_3)_4$ (0.63 g, 0.55 mmol, 0.05 equiv) were combined under an atmosphere of air and dissolved in 10.8 mL of a 1:1 H_2O:dioxane mixture. The reaction was attached to a reflux condenser and heated to 100 °C (while open to air) for 24 hours. Upon completion, the reaction mixture was diluted into ~400 mL of ethyl acetate, and the ethyl acetate layer was washed three times with ~400 mL aliquots of saturated aqueous $NaHCO_3$. The organic layer was then dried over $MgSO_4$ and concentrated under vaccum to yield a brown oil, which was carried on to the deprotection step without further purification. The crude oil was dissolved in 30 mL methanol, to which 7 mL concentrated aqueous HCl were added at room temperature. A precipitate appeared immediately following HCl addition. The solution was stirred at 50 °C for 2 hours, after which the precipitate was isolated by filtration. The precipitate was neutralized by suspending in a saturated aqueous solution of $NaHCO_3$, and the precipitate was then re-isolated by filtration and washed with H_2O to yield **H_2bpz** (0.05 g, 0.37 mmol, 3.4%) as a white solid. ^{1}H NMR (400 MHz, DMSO-d_6): δ 12.70 (s, 2H), 7.74 (s, 4H) ppm.

Synthesis of Co(bpz). H_2bpz (0.618 g, 4.6 mmol, 1.3 equiv) and $Co(SO_3CF_3)_2$ (1.24 g, 3.47 mmol, 1 equiv) were combined in 14.3 mL of anhydrous (DEF) in a 50-mL solvent bomb, under an atmosphere of air. The reaction mixture was degassed by the freeze–pump–thaw method for 5 cycles, then sealed by closing the stopcock of the solvent bomb while the frozen reaction mixture remained under vacuum. The solvent bomb was then heated at 160 °C for 3 days to afford a purple microcrystalline solid. Upon completion, the solvent bomb was opened to air, and 200 mL of anhydrous DMF was added to the solid product. The slurry was then transferred to a Pyrex jar, sealed, and heated to 110 °C

overnight. The supernatant was subsequently removed and replaced with 200 mL of fresh anhydrous DMF, and the slurry was again heated to 110 °C overnight. This solvent-exchange procedure was performed once daily for 7 days to completely remove unreacted starting material from the pores. Subsequently, the DMF was replaced with anhydrous CH_2Cl_2 following the same procedure but without heating; these CH_2Cl_2 exchanges were performed once daily for 3 days to allow activation from a lower-boiling solvent. To activate the material, the CH_2Cl_2 was decanted until 25 mL of solution remained. The resultant slurry was transferred to a 100-mL Schlenk flask, and the CH_2Cl_2 was evaporated by flowing Ar at room temperature for 1 h. The resultant solid was dried by flowing Ar at 160 °C for 6 h, then placed under dynamic vacuum at 160 °C overnight to yield **Co(bpz)** (0.204 g, 1.07 mmol, 31%). The activated solid was immediately transferred to a glovebox and handled under a dinitrogen atmosphere for all further experiments.

Dinitrogen, carbon dioxide, and dihydrogen adsorption isotherms for pressures in the range of 0-1.1 bar were measured using a Micromeritics ASAP 2420 gas adsorption analyzer. An activated sample was transferred under a N_2 atmosphere to preweighed analysis tubes, which were capped with a Transeal. The sample was evacuated on the instrument until the outgas rate was less than 3 μbar/min. The evacuated analysis tube containing degassed sample was then carefully transferred to an electronic balance and weighed to determine the mass of sample (typically 30-50 mg). The tube was then fitted with an isothermal jacket and transferred back to the analysis port of the instrument. The outgas rate was again confirmed to be less than 3 μbar/min. Dinitrogen and dihydrogen adsorption isotherms were measured at 77 K using a liquid N_2 bath, and carbon dioxide adsorption isotherms were measured at 195 K using a solid CO_2/isopropanol bath.

4.3. Results and Discussion

The homocoupling of a pyrazoleboronic ester was first observed when attempting to couple this boronic ester with an aryl bromide in a Suzuki cross-coupling reaction (Scheme 4.2). This reaction was undertaken as part of the effort to synthesize functionalized derivatives of benzenedipyrazole (H_2bdp), as described in Chapter 2. The

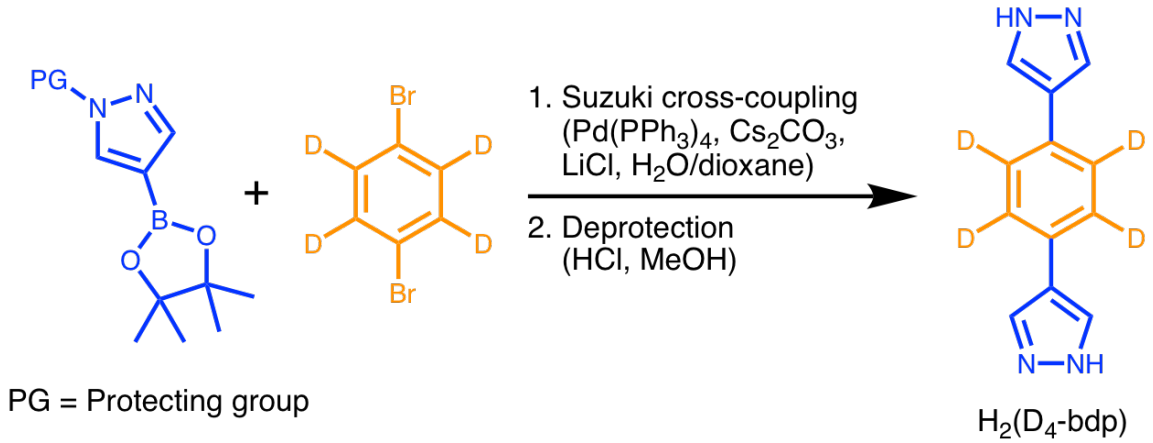

Scheme 4.2. Suzuki cross-coupling reaction with $H_2(D_4$-bdp) as desired product.

product of the reaction shown in Scheme 4.2 gave ^{1}H NMR shifts that were apparently consistent with the desired product, tetradeuterobenzenedipyrazole ($H_2(D_4$-bdp)), and this product was carried on to reaction with a cobalt(II) source in an attempt to form the metal–organic framework Co(D_4-bdp).

The metal–organic framework synthesis reaction did indeed yield a crystalline, purple precipitate, as expected. However, the powder X-ray diffraction (PXRD) spectrum of this precipitate revealed the material to be structurally distinct from Co(bdp) (Figure 4.1), a surprising and unlikely result for a derivative material whose only chemical difference from the parent material was partial deuteration of the ligand. Furthermore, the Langmuir surface area of the deuterated material proved to be approximately one-third that of Co(bdp), indicating pronounced structural differences.

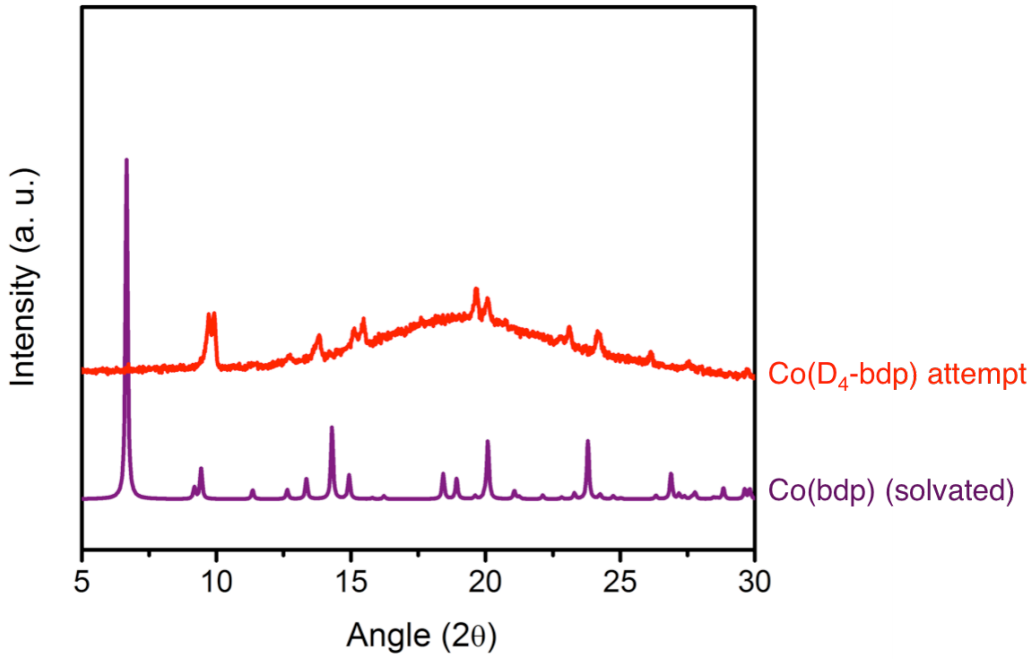

Figure 4.1. Powder X-ray diffraction patterns of DEF-solvated Co(bdp) (purple) and the product of a Co(D_4-bdp) synthesis attempt (red). The product of the Co(D_4-bdp) synthesis attempt was ultimately identified as Co(bpz). The Co(bdp) powder X-ray diffraction pattern shown here is simulated from the published single crystal X-ray diffraction structure.[23]

A literature search of pyrazolate-based metal–organic frameworks led to the hypothesis that the true identity of the crystalline product described above was Co(bpz) (bpz^{2-} = 4,4'-bipyrazolate)[19] and therefore that the major product of the synthesis depicted in Scheme 4.2 was 4,4'-bipyrazole (H_2bpz; Scheme 4.3). The replacement of ^{1}H atoms with NMR-silent deuterium atoms on the aryl bromide had allowed the initial misidentification of H_2bpz as $H_2(D_4$-bdp), but the identity of the major product of the reaction shown in Schemes 4.2-4.3 was confirmed to be H_2bpz via liquid chromatography-mass spectrometry (LCMS).

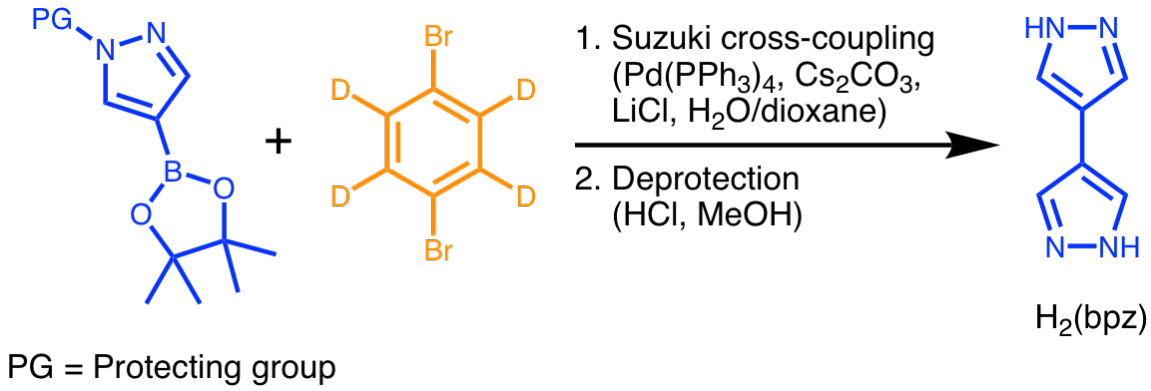

Scheme 4.3. The product of the above Suzuki cross-coupling reaction was identified as H_2(bpz), leading to the discovery of the Pd-catalzyed homocoupling of pyrazoleboronic esters.

This palladium-catalyzed homocoupling of pyrazoleboronic ester in the presence of an aryl bromide (usually the preferred coupling partner in such a reaction mixture) represented unexpected and heretofore unpublished reactivity. To further investigate this reactivity, a survey of reaction conditions was undertaken to look for the formation of H_2bpz from a starting pyrazoleboronic ester. Test-scale reactions were monitored by LCMS to identify H_2bpz formation, and ultimately conditions were identified that led to complete conversion as shown by LCMS (see H_2bpz Synthesis, Section 4.2). Due to the fact that the work-up and deprotection steps of this synthesis were completely unoptimized, the final yield was only 3.4%. However, these results demonstrate our ability to synthesize pure H_2bpz via a simple palladium-catalyzed homocoupling of pyrazoleboronic ester, rather than through the laborious traditional procedures.[12-15] Promising efforts are ongoing with our collaborator Prof. Jiwoong Lee at the University of Copenhagen to improve the yield of this homocoupling and optimize it further.

A pure sample of H_2bpz was used to resynthesize the metal–organic framework Co(bpz), as our initial Co(bpz) synthesis had used an H_2bpz sample containing 1,4-dibromobenzene-d_4 and other impurities from the failed Suzuki cross-coupling. The Co(bpz) synthesis using pure H_2bpz linker yielded a somewhat different PXRD spectrum from the initial the original Co(bpz) synthesis, which had likely incorporated various pyrazolate impurities into the framework (Figure 4.2). Although the synthesis of Co(bpz) has been reported previously, the authors of that report could not obtain a PXRD spectrum due to fluorescence contamination and therefore could not determine the structure of Co(bpz), although the authors speculated that Co(bpz) was likely to be isostructural to Zn(bpz).[19] The PXRD spectrum of Co(bpz) (reported herein for the first time) upholds this hypothesis, as the Co(bpz) diffraction pattern is indeed isostructural to that of Zn(bpz) (Figure 4.3). Notably, the PXRD spectrum of Co(bpz) did not change during the course of one month, during which time the sample was stored on the benchtop under an atmosphere of air (Figure 4.4). The fact that Co(bpz) does not lose crystallinity during prolonged exposure to air represents an exciting improvement over many flexible metal–organic frameworks, including Co(bdp), and this property makes Co(bpz) a potentially promising adsorbent for industrial gas sorption applications.

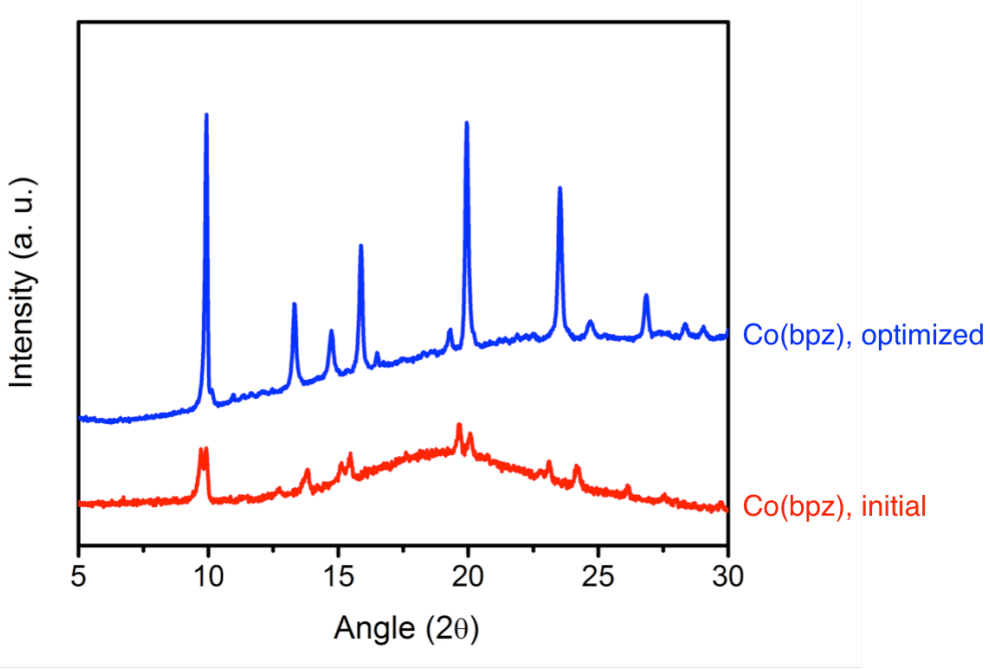

Figure 4.2. Powder X-ray diffraction patterns of the products of the initial synthesis of Co(bpz) (red) and the optimized synthesis of Co(bpz) (blue).

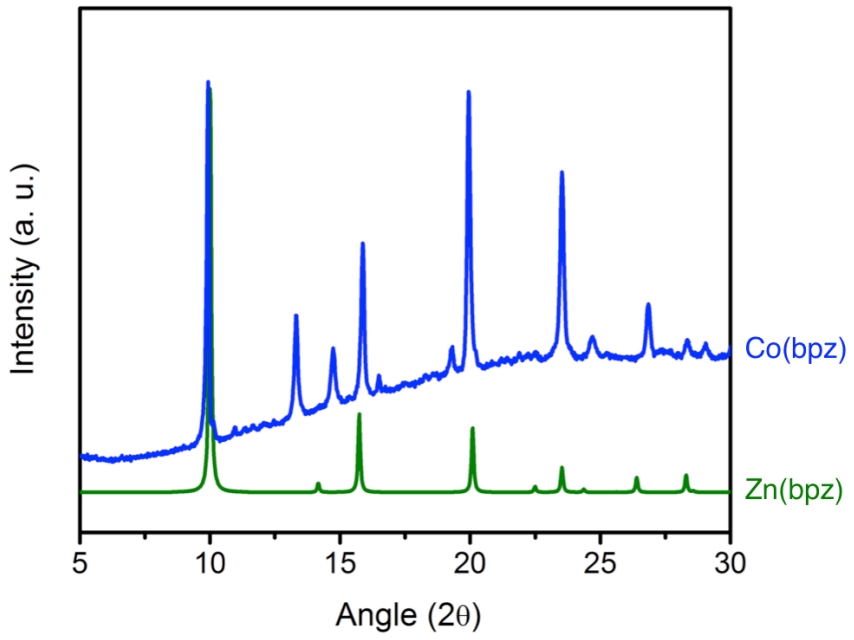

Figure 4.3. Powder X-ray diffraction patterns of Co(bpz) (blue) and Zn(bpz) (green). The diffraction pattern for Co(bpz) is reported herein for the first time, and the diffraction pattern for Zn(bpz) is simulated from the Zn(bpz) single crystal X-ray diffraction structure reported in Ref. 19.

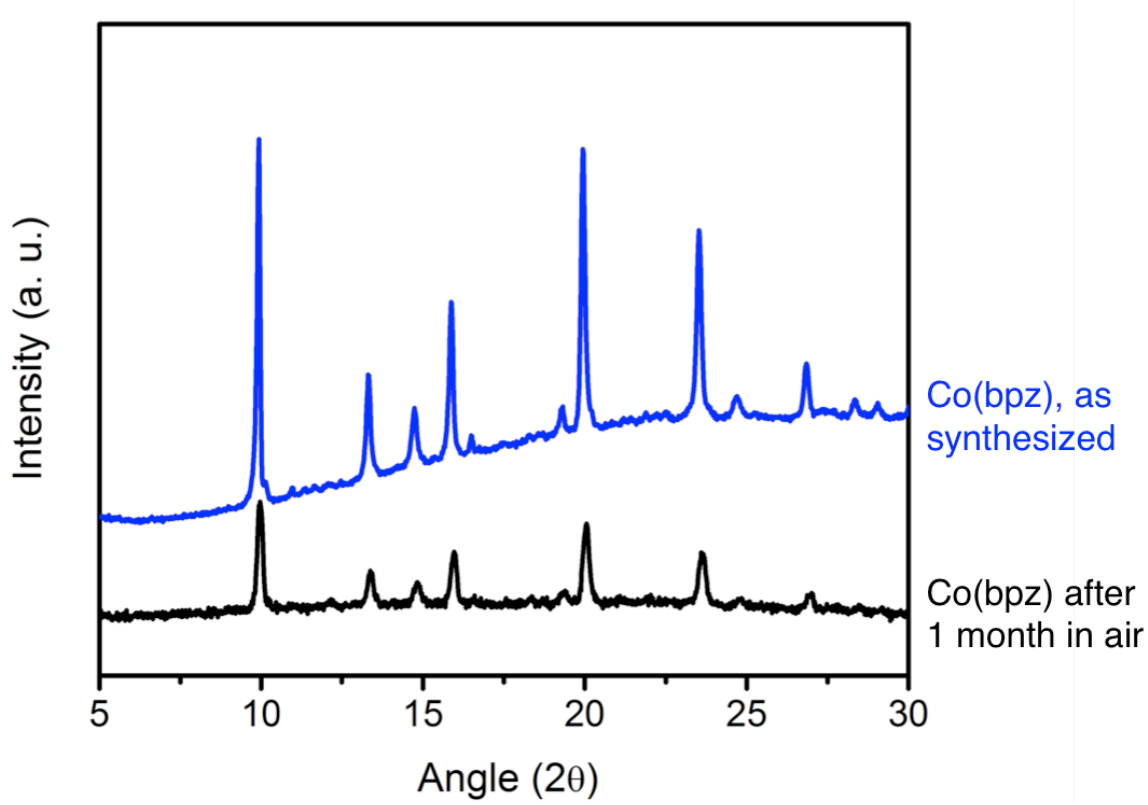

Figure 4.4. Powder X-ray diffraction patterns of Co(bpz) immediately after synthesis (blue) and after storage for 1 month in air (black).

To further confirm the structure of Co(bpz), attempts were made to grow Co(bpz) crystals large enough for single-crystal X-ray diffraction (SCXRD). However, Co(bpz) synthesis reactions under vacuum, under air, in silanized and unsilanized glassware, and at various scales, concentrations, and pH ranges all failed to yield crystallites suitable for SCXRD.

A 77 K N_2 adsorption isotherm (Figure 4.5) yields a Langmuir surface area of 1064 m^2/g for Co(bpz), nearly identical to the previously reported value of 1057 m^2/g.[19] However, the shape of the 77 K N_2 isotherm constitutes a major discrepancy between the published report and the current work: While Pettinari et al. state that "No steps could be detected in the low-pressure region of [Co(bpz)], at variance with what was reported for the homologous species [Co(bdp)]",[19] our data does indeed show a distinct step at very low pressures (Figures 4.6-4.7). Specifically, at pressures below ~10^{-5} bar, the N_2 isotherm rises steeply to a capacity of ~ 5mmol/g and reaches a plateau. Then, at ~10^{-5} bar, the isotherm undergoes a second steep rise to a saturation capacity of ~10 mmol/g.

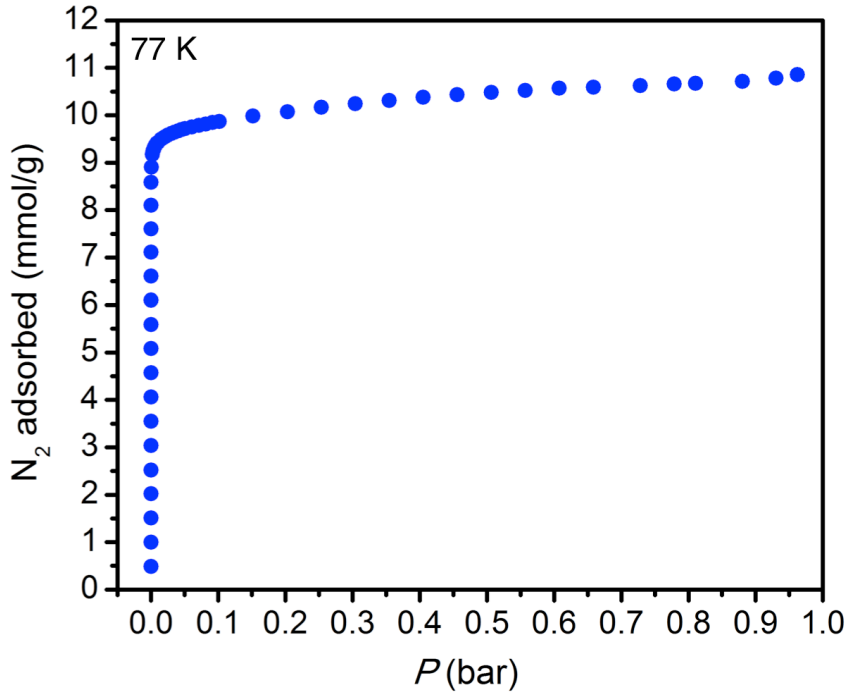

Figure 4.5. N_2 adsorption isotherm at 77 K for Co(bpz).

Steps in the adsorption isotherms of metal–organic frameworks can result from several unrelated phenomena, including a change in adsorption mechanism,[20] a change in spin state of the metal,[21] or a change in overall framework structure.[22] In this case, the step-shaped isotherm of Co(bpz) is likely to indicate structural flexibility of the framework, as does that of the structurally-related framework Co(bdp). Indeed, because Co(bdp) shows such extensive structural flexibility,[23] Pettinari et al. found it worth explicit mention in their paper that Co(bpz) did not.[19] Although they do not provide the raw data for their isotherms, I hypothesize that Pettinari et al. did not collect many data points at pressures below 10^{-5} bar (which is indeed an uncommonly low pressure to measure in a surface area measurement) and therefore did not observe the step in the isotherm of Co(bpz).

The steps observed in the 77 K N_2 isotherm are reproduced in the 195 K CO_2 isotherm for Co(bpz), as shown in Figures 4.8-4.10. In fact, the similarities between the N_2 and CO_2 isotherms are striking, as the first plateau occurs at approximately 5 mmol/g and the second at approximately 10 mmol/g for both gases. (The N_2 and CO_2 isotherms were performed at 77 K and 195 K, respectively, because these are the condensation temperatures for each adsorbate at atmospheric pressure.) These results indicate that Co(bpz) may begin as the same phase in both cases, a partially-collapsed structure capable of accommodating ~5 mmol adsorbate per gram, and that Co(bpz) subsequently expands to a fully-open phase capable of adsorbing ~10 mmol/g. It will be critical to perform *in situ* powder X-ray diffraction experiments over varying gas pressures to identify the structural phase change responsible for shape of the N_2 and CO_2 isotherms, and such experiments will be carried out soon at the Advanced Photon Source at Argonne National Laboratory.

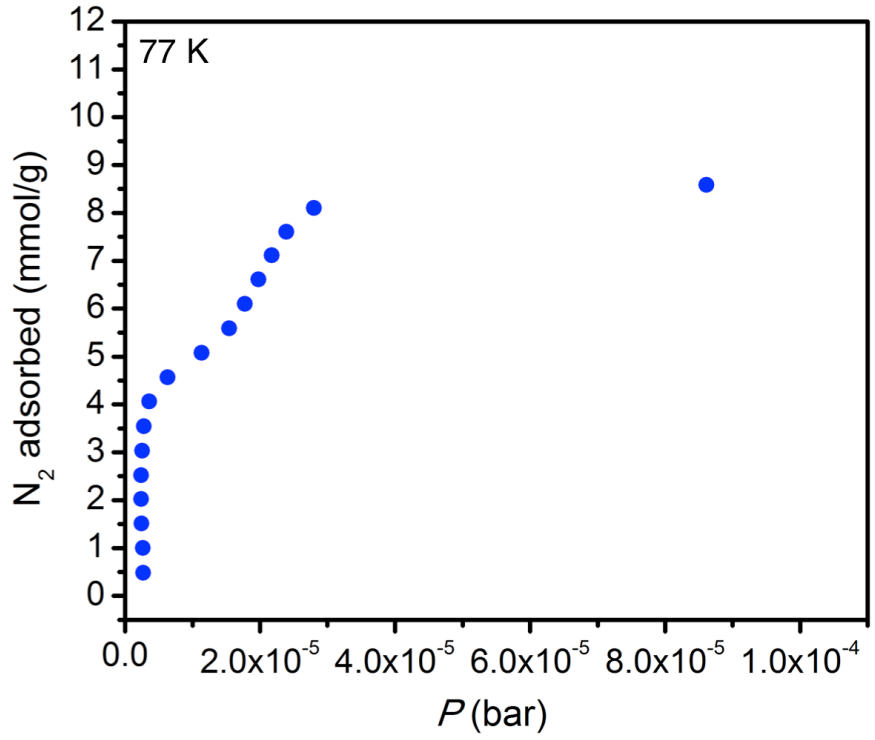

Figure 4.6. N_2 adsorption isotherm at 77 K for Co(bpz), at pressures below 10^{-4} bar.

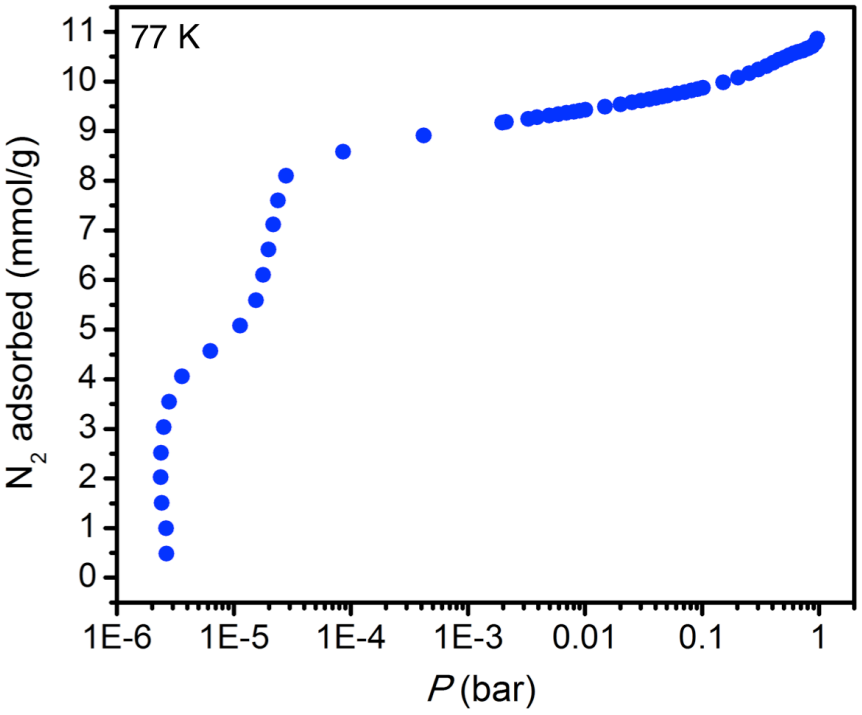

Figure 4.7. N_2 adsorption isotherm at 77 K for Co(bpz), with the *x*-axis plotted logarithmically.

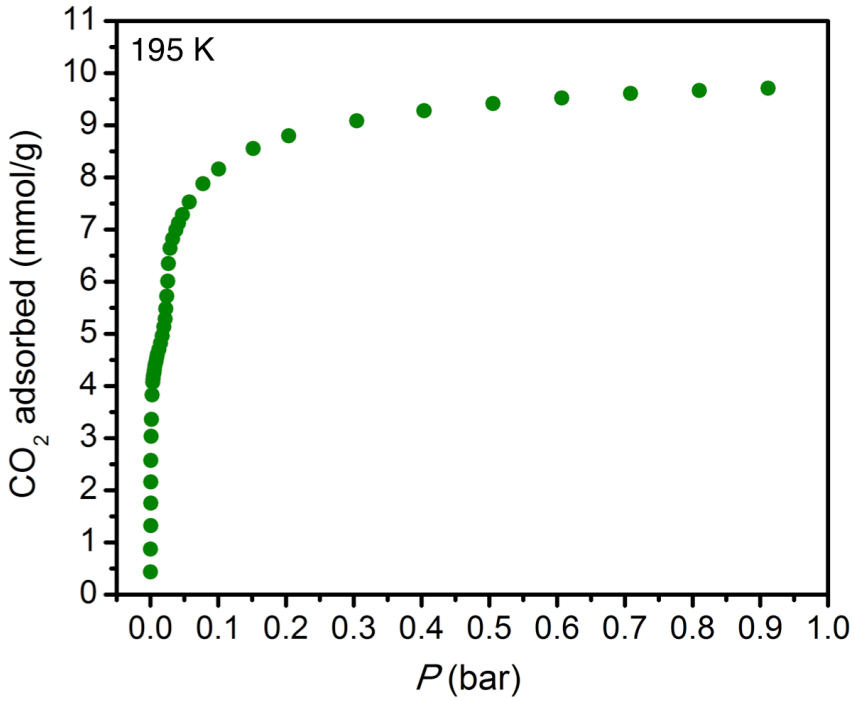

Figure 4.8. CO_2 adsorption isotherm at 195 K for Co(bpz).

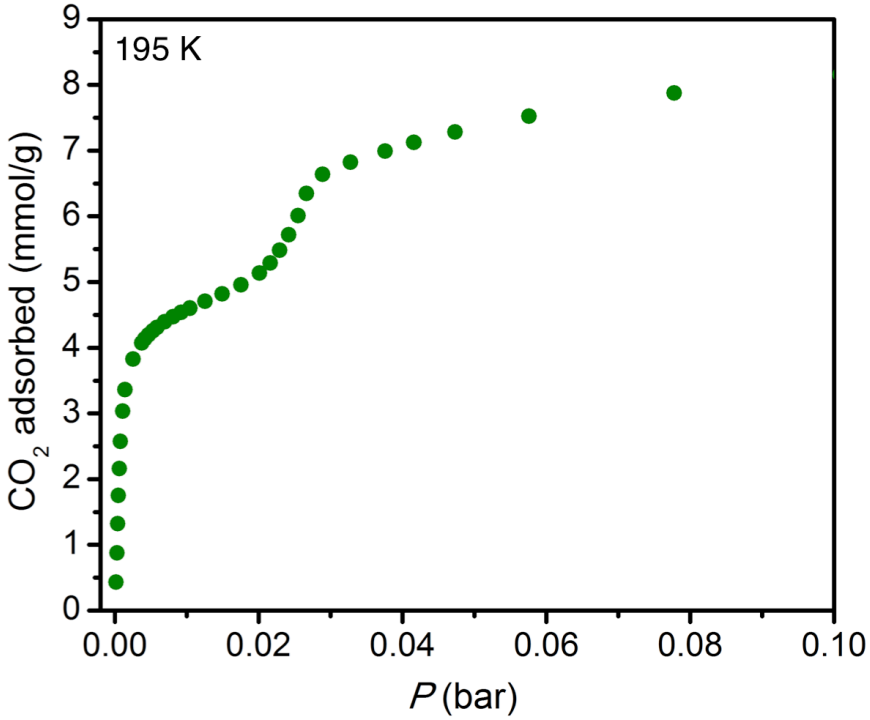

Figure 4.9. CO_2 adsorption isotherm at 195 K for Co(bpz), at pressures below 0.1 bar.

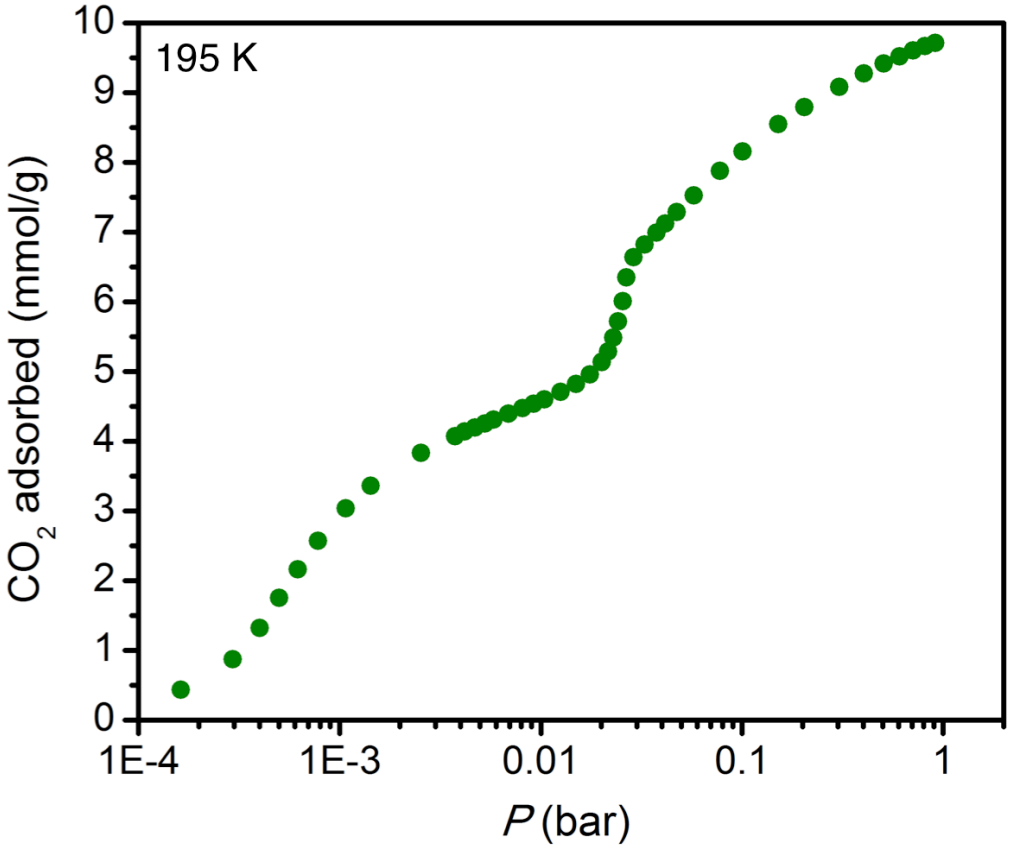

Figure 4.10. CO_2 adsorption isotherm at 195 K for Co(bpz), with the *x*-axis plotted logarithmically.

Unlike the results for N_2 and CO_2 adsorption, the 77 K H_2 isotherm for Co(bpz) shows no evidence of any steps, instead adopting a Type I isotherm shape (Figures 4.11-4.12). This unexpected result indicates that under conditions of H_2 adsorption, Co(bpz) bypasses the partially-collapsed intermediate seen at ~5 mmol/g in the N_2 and CO_2 isotherms and instead transitions directly to the fully-expanded phase. This behavior can be rationalized by the weaker binding strength of H_2 as an adsorbate[24] in comparison to N_2 and CO_2: If the fully-expanded phase of Co(bpz) is less strained and more energetically favorable than the partially-collapsed phase, the interaction between H_2 molecules and the walls of Co(bpz) may not be strong enough to stabilize the partially-collapsed phase. Again, *in situ* powder X-ray diffraction experiments will shed light on the phase-change behavior of Co(bpz) and its variation from one gas to another.

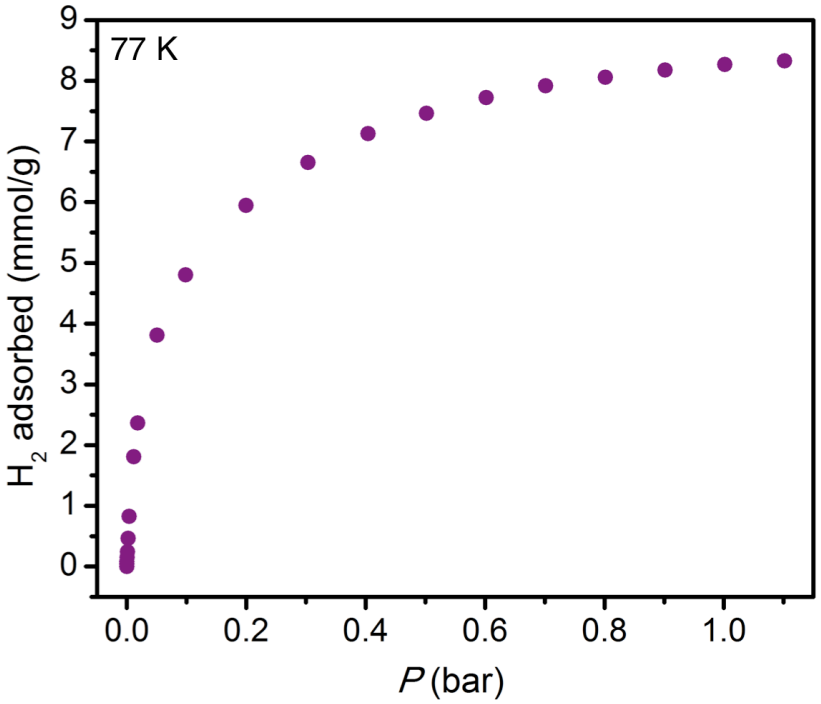

Figure 4.11. H_2 adsorption isotherm at 77 K for Co(bpz).

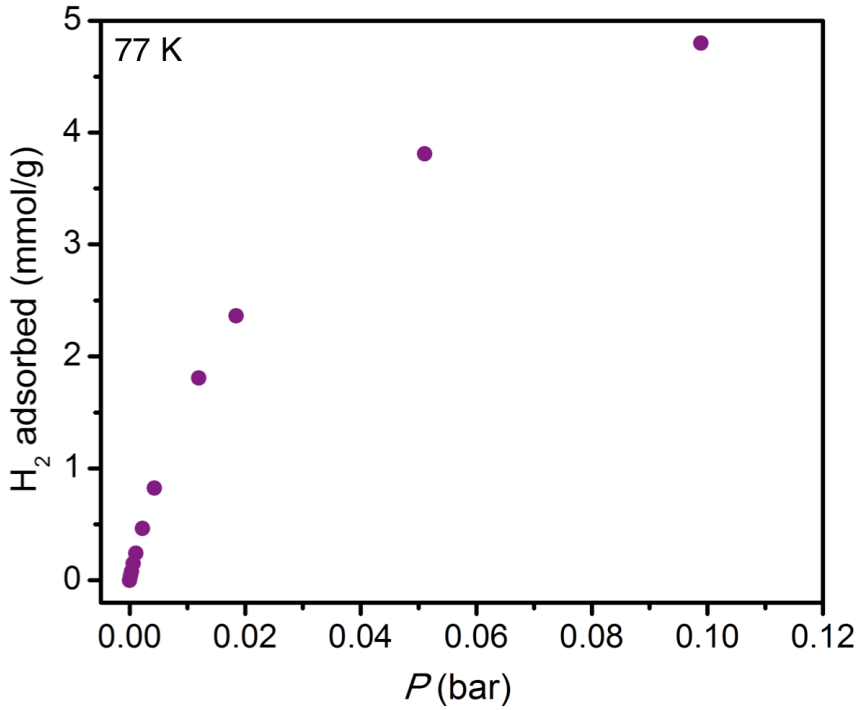

Figure 4.12. H_2 adsorption isotherm at 77 K for Co(bpz), at pressures below 0.12 bar.

Experiments are underway to probe the high-pressure, room temperature adsorption of N_2, CO_2, and H_2 in Co(bpz), to determine whether the step-wise behavior is reproduced at 25 °C, as such conditions are more typical of industrial gas storage and separation applications. As was described in detail in Chapters 2 and 3, adsorption-induced phase changes confer notable advantages on metal–organic frameworks in terms of their gas storage and separation properties. In the case of Co(bpz), one such application might be the purification of H_2, as the partially-collapsed phase is accessible to CO_2 but not H_2. The fact that Co(bpz) is porous to gases even in the partially-collapsed phase may improve its real-world performance in an industrial gas separation, which would likely be effected in a dynamic breakthrough set-up. In contrast to Co(bdp), which is nonporous to CO_2 below 2 bar at room temperature (as described in Chapter 3), Co(bpz) would not allow a low-pressure CO_2 slip due to the shape of its isotherm. Furthermore, because Co(bpz) shows long-term stability in air, it could comprise a significant improvement over air-sensitive flexible metal–organic frameworks such as Co(bdp). Finally, the narrow pores of Co(bpz) may prove to be highly effective at separating mixtures of hydrocarbons, as in the the case of $Fe_2(bdp)_3$,[25] and therefore the adsorption of other gases beyond N_2, CO_2, and H_2 in Co(bpz) is a promising topic of investigation.

4.4. Conclusions

The palladium-catalyzed homocoupling of pyrazoleboronic esters to form a pyrazole-pyrazole bond is reported here for the first time, and this novel reactivity is optimized to give conditions for the straightforward synthesis of 4,4'-bipyrazole (H_2bpz). Among other uses, this molecule is employed as a linker for many metal–organic frameworks, although its synthesis until now required several laborious steps and could not be accomplished by a metal-catalyzed cross-coupling.[12-16] We demonstrate the importance of H_2bpz as a metal–organic framework linker by using it to synthesize and characterize Co(bpz), a flexible, air-stable framework. Gas adsorption studies indicate that Co(bpz) undergoes adsorption-induced phase changes, and this newfound flexibility merits further study by *in situ* powder X-ray diffraction. The narrow one-dimensional channels of this framework, combined with its stability and flexibility, make it a promising adsorbent for numerous gas separations, and the facile H_2bpz synthesis reported herein makes Co(bpz) a readily accessible material.

4.5. Acknowledgements—I gratefully acknowledge the National Science Foundation Graduate Research Fellowship Program for providing funding support. I thank Ever Velazquez and Mike Ziebel for experimental assistance, and I am grateful to Prof. Jiwoong Lee for invaluable scientific discussions, collaboration, and mentorship on this project.

4.6. References

(1) Trofimenko, S. *Chem. Rev.* **1972**, *72*, 497.
(2) Mukherjee, R. *Coord. Chem. Rev.* **2000**, *203*, 151.
(3) Fustero, S.; Sánchez-Roselló, M.; Barrio, P.; Simón-Fuentes, A. *Chem. Rev.* **2011**, *111*, 6984.

(4) Khan, M. F.; Alam, M. M.; Verma, G.; Akhtar, W.; Akhter, M.; Shaquiquzzaman, M. *Eur. J. Med. Chem.* **2016**, *120*, 170.
(5) Ansari, A.; Ali, A.; Asif, M.; Shamsuzzaman. *New J. Chem.* **2017**, *41*, 16.
(6) Burckhardt, U.; Hintermann, L.; Schnyder, A.; Togni, A. *Organometallics* **1995**, *14*, 5415.
(7) Ye, C.; Gard, G. L.; Winter, R. W.; Syvret, R. G.; Twamley, B.; Shreeve, J. n. M. *Org. Lett.* **2007**, *9*, 3841.
(8) Dedeian, K.; Shi, J.; Shepherd, N.; Forsythe, E.; Morton, D. C. *Inorg. Chem.* **2005**, *44*, 4445.
(9) Cavero, E.; Uriel, S.; Romero, P.; Serrano, J. L.; Giménez, R. *J. Am. Chem. Soc.* **2007**, *129*, 11608.
(10) Taydakov, I. V.; Akkuzina, A. A.; Avetisov, R. I.; Khomyakov, A. V.; Saifutyarov, R. R.; Avetissov, I. C. *J. Lumin.* **2016**, *177*, 31.
(11) Pettinari, C.; Tăbăcaru, A.; Galli, S. *Coord. Chem. Rev.* **2016**, *307*, 1.
(12) Kornfeld, E. C.; Jones, R. G. *J. Org. Chem.* **1954**, *19*, 1671.
(13) Arnold, Z. *Collect. Czech. Chem. Commun.* **1962**, *27*, 2993.
(14) Trofimenko, S. *J. Org. Chem.* **1964**, *29*, 3046.
(15) Boldog, I.; Sieler, J.; Chernega, A. N.; Domasevitch, K. V. *Inorg. Chim. Acta* **2002**, *338*, 69.
(16) Coburn, M. D. *J. Heterocyclic Chem.* **1971**, *8*, 153.
(17) Jedinák, L.; Zátopková, R.; Zemánková, H.; Šustková, A.; Cankař, P. *J. Org. Chem.* **2017**, *82*, 157.
(18) Adamo, C.; Amatore, C.; Ciofini, I.; Jutand, A.; Lakmini, H. *J. Am. Chem. Soc.* **2006**, *128*, 6829.
(19) Pettinari, C.; Tăbăcaru, A.; Boldog, I.; Domasevitch, K. V.; Galli, S.; Masciocchi, N. *Inorg. Chem.* **2012**, *51*, 5235.
(20) McDonald, T. M.; Mason, J. A.; Kong, X.; Bloch, E. D.; Gygi, D.; Dani, A.; Crocella, V.; Giordanino, F.; Odoh, S. O.; Drisdell, W.; Vlaisavljevich, B.; Dzubak, A. L.; Poloni, R.; Schnell, S. K.; Planas, N.; Lee, K.; Pascal, T.; Wan, L. F.; Prendergast, D.; Neaton, J. B.; Smit, B.; Kortright, J. B.; Gagliardi, L.; Bordiga, S.; Reimer, J. A.; Long, J. R. *Nature*, **2015**, *519,* 303.
(21) Reed, D. A.; Keitz, B. K.; Oktawiec, J.; Mason, J. A.; Runčevski, T.; Xiao, D. J.; Darago, L. E.; Crocellà, V.; Bordiga, S.; Long, J. R. *Nature* **2017**, *550*, 96.
(22) Mason, J. A.; Oktawiec, J.; Taylor, M. K.; Hudson, M. R.; Rodriguez, J.; Bachman, J. E.; Gonzalez, M. I.; Cervellino, A.; Guagliardi, A.; Brown, C. M.; Llewellyn, P. L.; Masciocchi, N.; Long, J. R. *Nature* **2015**, *527,* 357.
(23) Choi, H. J.; Dincă, M.; Long, J. R. *J. Am. Chem. Soc.* **2008,** *130,* 7848.
(24) Suh, M. P.; Park, H. J.; Prasad, T. K.; Lim D.-W. *Chem. Rev.* **2012**, *112*, 782.
(25) Herm, Z. R.; Wiers, B. M.; Mason, J. A.; van Baten, J. M.; Hudson, M. R.; Zajdel, P.; Brown, C. M.; Masciocchi, N.; Krishna, R.; Long, J. R. *Science* **2013**, *340*, 960.